



SURFACE ACOUSTIC WAVE DEVICES
AS CHEMICAL VAPOR SENSORS

THESIS

Daniel Gallagher, GS-11, DAF

AFIT/GE/ENG/09-16

DEPARTMENT OF THE AIR FORCE
AIR UNIVERSITY

AIR FORCE INSTITUTE OF TECHNOLOGY

Wright-Patterson Air Force Base, Ohio

APPROVED FOR PUBLIC RELEASE; DISTRIBUTION UNLIMITED.

The views expressed in this thesis are those of the author and do not reflect the official policy or position of the United States Air Force, Department of Defense, or the United States Government.

SURFACE ACOUSTIC WAVE DEVICES
AS CHEMICAL VAPOR SENSORS

THESIS

Presented to the Faculty
Department of Electrical and Computer Engineering
Graduate School of Engineering and Management
Air Force Institute of Technology
Air University
Air Education and Training Command
In Partial Fulfillment of the Requirements for the
Degree of Master of Science in Electrical Engineering

Daniel Gallagher, BSEE
GS-11, DAF

March 2009

APPROVED FOR PUBLIC RELEASE; DISTRIBUTION UNLIMITED.

SURFACE ACOUSTIC WAVE DEVICES
AS CHEMICAL VAPOR SENSORS

Daniel Gallagher, BSEE
GS-11, DAF

Approved:

/signed/

9 March 2009

Lt Col Ronald A. Coutu, Jr., PhD, PE
(Chairman)

Date

/signed/

9 March 2009

Maj LaVern A. Starman, PhD (Member)

Date

/signed/

9 March 2009

Dr. Lawrence L. Brott, PhD (Member)

Date

Abstract

In order to effectively neutralize non-traditional threats to US forces and population such as improvised explosive devices (IED) and chemical, biological, radiological, nuclear, and explosive (CBNRE) weapons, a flexible vapor sensor platform is proposed. This work involves the design, fabrication, and testing of coated surface acoustic wave devices for vapor sensing ability. Devices were fabricated in-house using MEMS fabrication techniques, then coated with a thin layer of a Nafion polymer. The frequency response of coated devices displayed 2 MHz frequency shifts around the resonance frequency upon introduction of ethanol vapors into the nitrogen vapor stream. This indicates strong sensing ability based upon the viscoelastic changes in the polymer film. Further work should include new coating layers such as biological molecule self-assembled monolayers, circuitry to allow portability, and a preconcentrator to increase sensitivity.

Acknowledgements

First and foremost, I acknowledge my God, Jesus Christ, who gives me peace and hope. I see science as an investigation into the mysteries of creation.

To my friends and family, thank you for supporting me during my time here. Your understanding, love, and encouragement were invaluable to me. Thank you to those who were willing to pitch in and lighten my load, especially Brent, Doneda, and Pam.

I would like to express my appreciation to those who provided leadership and guidance to me while I was here. Thank you to Lt Col James Fellows for pointing me in the right direction and pushing me to excel both in the classroom and during this thesis. Thank you to Lt Col Ronald Coutu for working with me from your very first days here at AFIT, even as hard as it was for you to come in partially through the thesis. Thank you to Maj Lavern Starman for constant availability to answer questions and for the encouraging presence even during late nights in the lab. Thank you to Dr. Larry Brott for your thoughts, guidance, and willingness to help out on short notice. Thank you to Capt Mark Allard for providing the leadership and oversight of this project from the sponsor's side. Thank you to Dr. Rajesh Naik for getting me involved in the crazy world where biology, chemistry, and engineering meet, and for providing the vision for biosensor technology.

Several people are worthy of recognition for providing technical assistance. Rich Johnston performed numerous e-beam metallization runs. Larry Callahan diced several wafers for me. Mark Allard and Laura Sowards designed the original devices at AFRL. Thank you all.

Finally, thank you to the rest of the MEMS crew: Luke, Adam, Nick, James, Mo, Todd, and Mimi. Going through these difficulties together helped us accomplish more than we could have alone. I appreciate each of you and the support you have given me.

Daniel Gallagher

Table of Contents

	Page
Abstract	iv
Acknowledgements	v
Table of Contents	vi
List of Figures	ix
List of Tables	xii
List of Symbols	xiv
List of Abbreviations	xv
I. Introduction	1
1.1 Motivation	1
1.2 Performance Goals	2
1.3 Objective and Approach	3
II. Literature Review	5
2.1 Theory of SAW Devices as Vapor Sensors	5
2.1.1 Piezoelectric Effect	5
2.1.2 Excitation of Acoustic Waves Using Interdigital Transducer	6
2.1.3 Substrate Acoustic Wave Propagation	9
2.1.4 Thin Films as Vapor Sensing Mechanism	10
2.2 Design of SAW Devices for Sensing Applications	14
2.2.1 Effects of SAW Geometry	14
2.2.2 Material Considerations	18
2.2.3 Enhancement Techniques	20
2.3 MEMS Fabrication Techniques	24
2.3.1 Bulk Micromachining	27
2.3.2 Surface Micromachining	30
2.3.3 Microtemplating	32
2.4 Fabrication of SAW	35
2.4.1 Substrate Preparation	35
2.4.2 IDT Fabrication	35
2.4.3 Sensing Film Fabrication	35
2.5 Characterization Techniques for SAW Sensors	37
2.5.1 Transmission Parameter Analysis	37
2.5.2 Integrated Oscillator Analysis	37
2.6 Chapter Summary	38

	Page
III. Research Methodology	40
3.1 Plan of Attack Overview	40
3.2 SAW Device Design	41
3.2.1 Mask Design	41
3.2.2 Material Choices	43
3.3 Device Fabrication Using AFRL Mask	44
3.4 Testing AFRL-Designed SAW Devices	46
3.5 Fabrication of AFIT-Designed SAW Devices	49
3.6 Wire Bonding	49
3.7 Testing of AFIT-designed Devices	50
3.8 Sensing Layer Fabrication	51
3.9 Testing of Coated SAW Devices	52
3.10 Chapter Summary	54
IV. Results	56
4.1 Results of Device Fabrication using AFRL Mask	56
4.2 Testing AFRL-Designed SAW Devices	60
4.3 Device Fabrication using AFIT Mask	62
4.3.1 Wire Bonding	63
4.4 Testing AFIT-Designed Devices	64
4.5 Testing of Coated SAW Sensors	64
4.5.1 Electrical Characterization	64
4.5.2 Vapor Sensing	65
4.6 Chapter Summary	69
V. Conclusions	71
5.1 Results Analysis	71
5.1.1 Fabrication	71
5.1.2 SAW Activity	71
5.1.3 Testing of Coated Chips	73
5.2 Future Project Recommendations	75
5.2.1 Fabrication	75
5.2.2 Investigation of Intermetallics	75
5.2.3 Sensor Testing	75
5.2.4 Oscillator Design	76
5.2.5 Preconcentrator Design	76
5.2.6 Packaging	77
5.3 Conclusions	77

	Page
Appendix A. Fabrication Details	78
A.1 Fabrication of AFRL-Designed Devices	78
A.2 Fabrication of AFIT-Designed SAW Devices	85
A.3 Wire Bonding	96
Appendix B. Additional Results	99
B.1 Fabrication	99
B.1.1 Wafer Dicing	99
B.1.2 Series 1-3 Fabrication	99
B.2 Testing at AFIT with Micromanipulator Probe Station	102
B.3 Series 3 Testing at AFRL	106
B.3.1 COTS SAW testing	106
B.4 Second Generation Device Fabrication	109
B.4.1 Series 4 Fabrication	109
B.4.2 Series 5 Fabrication	114
B.4.3 Series 6 Fabrication	118
B.4.4 Series 7 Fabrication	122
B.4.5 Series 8 Fabrication	124
B.4.6 Series 9 Fabrication	126
B.4.7 Series 10 Fabrication	131
B.5 Testing Newly Designed Devices	131
B.5.1 Calibration with MMR Probe Station	131
B.6 Additional Vapor Testing	133
Appendix C. Lessons Learned	136
C.1 Equipment	136
C.2 Processing	136
C.3 Design	138
C.4 Planning	138
Bibliography	140

List of Figures

Figure		Page
2.1	Piezoelectric Effect in Non-Centrosymmetric Crystals	6
2.2	IDT	7
2.3	Surface Acoustic Wave Propagation Modes	10
2.4	Standard Frequency Response	16
2.5	Resonator Vs. Delay Line Design	17
2.6	Apodization	22
2.7	Sin^2 Apodization	23
2.8	Apodization Simulation	23
2.9	IDT Generation of Bulk and Surface Waves	24
2.10	Chirped IDT	25
2.11	Photolithographic Patterning	26
2.12	Etch Stop	28
2.13	Anisotropic Wet Etch	28
2.14	Step Coverage	30
2.15	Electroplating and Sacrificial Layers	32
2.16	Metal Lift-Off	33
2.17	Casting	34
2.18	SAW Oscillator Configuration	39
3.1	RF Splitter	48
3.2	Vapor Test Setup	49
3.3	Nafion Chemical Structure	51
3.4	Ethanol Vapor Bubbler	54
4.1	Series 1B Lithography	56
4.2	Series 1B Metal Lift-off	58
4.3	Series 2 Devices	59
4.4	Series 3 SEM	60

Figure		Page
4.5	Custom Signal Splitter Testing	61
4.6	Sample 3.6 145 MHz Testing	61
4.7	Sample 4.4 Metallization	62
4.8	Series 6 SEM	63
4.9	Series 6 SEM	64
4.10	Testing of Device 6.3.3	65
4.11	Nafion Conductivity Tests	66
4.12	10 Micron Nafion Coated Device Testing	67
4.13	6 Micron Nafion Coated Device Testing	68
4.14	3 Micron Nafion Coated Device Testing	70
B.1	Sample 1a.1 Lithography	100
B.2	Sample 1a.8 Lithography	100
B.3	Series 3 Lift-off	101
B.4	Sample 3.2 Photoresist	102
B.5	Sample 3.2 Development	103
B.6	Sample 3.1 Development B	103
B.7	Sample 3.6 Development	104
B.8	Sample 3.1 Metallization	104
B.9	Sample 3.1 Testing	105
B.10	S_{21} Testing of Sample 3.6	107
B.11	Adaptor and Cable S_{21} Testing	108
B.12	Sample 3.6 87 MHz Testing	108
B.13	Sample 3.6 290 MHz Testing	109
B.14	Sample 4.2 Lithography	110
B.15	Series 4 Lithography	111
B.16	Sample 4.2 Metallization	111
B.17	Sample 4.3 Metallization	112
B.18	Sample 4.5 Metallization	112

Figure		Page
B.19	Device 4.3.2 Burnout	113
B.20	Sample 4.1 2nd Lithography	114
B.21	Sample 4.5 Bond pads	115
B.22	Sample 4.2 Wire bonding	115
B.23	Sample 4.1 Wire bonding	116
B.24	Sample 5.1 Lithography	117
B.25	Sample 5.5 Lithography	117
B.26	Sample 5.4 Lithography	118
B.27	Series 5 Metal Lift-off	119
B.28	Series 6 double LOR3A Lithography	120
B.29	Series 6 Single LOR3A Lithography	121
B.30	Series 6 Unacceptable Metal Lift-off	121
B.31	Sample 6.2 Bond pad Lithography	122
B.32	Sample 6.3 Bond pads	123
B.33	Series 5 and 6 Successful Bondpad Deposition	123
B.34	Series 7 Quartz Lithography	124
B.35	Series 7 Quartz Lithography with HDMS	125
B.36	Series 7 Metal Lift-off	125
B.37	Sample 8.4 lithography	126
B.38	9.1 and 9.2 Lithography	127
B.39	9.4 - 9.6 Lithography	128
B.40	Series 9 Metal Lift-off	130
B.41	Series 10 Lithography	132
B.42	Calibrated Testing of Device 6.4.1	133
B.43	3 Micron Nafion Coated Device Repeat 1	134
B.44	3 Micron Nafion Coated Device Repeat 2	135

List of Tables

Table		Page
2.1	Properties of Several Common SAW Substrate Materials.	19
3.1	Design Parameters of Basic SAW Device	42
3.2	Novel Layered SAW Electrodes	43
3.3	Series 3 Lithography Process	46
3.4	Fabrication Series Overview	50
4.1	Nafion Coated Resonance	65
5.1	Recommended Fabrication Process	72
A.1	Series 1a Lithography Process	78
A.2	Series 1a Lithography Details	79
A.3	Series 1b Lithography Process	80
A.4	Series 1b Lithography Details	81
A.5	Series 2 Lithography Process	83
A.6	Series 3 Lithography Process	84
A.7	Series 4 Development Times	85
A.8	Series 5 Fabrication	86
A.9	Series 6 Fabrication	87
A.10	Series 6 Lithography Details	88
A.11	Series 6 Lithography Details.	88
A.12	Series 7 Fabrication	90
A.13	Series 7 Lithography Details	90
A.14	Series 8 Fabrication	91
A.15	Series 9 Fabrication	93
A.16	Series 10 Fabrication	94
A.17	Series 10 Fabrication Details	95
A.18	Wire Bonding Test Set A	96
A.19	Wire Bonding Test Set B and C	96

Table		Page
A.20	Wire Bonding Test Set D - 18 Micron Wire	97
A.21	Wire Bonding Test Set D - 25 Micron Wire	98

List of Symbols

Symbol	Page
d_{ij}	6
\mathbf{d}	7
f	8
v	8
λ	8
N	8
f_o	8
$L(f)$	9
U	11
$\Delta\rho$	11
c_m	11
P	11
c_e	12
G'	12
f_o^2	15
N	15
ϕ_E	18
K^2	19
C_s	19
c_m	19

List of Abbreviations

Abbreviation		Page
GSA	Global Situational Awareness	1
FLTC	Focused Long Term Challenge	1
IED	Improvised Explosive Devices	1
CBRNE	Chemical, Biological, Radiological, Nuclear, and Explosive . .	1
UAV	Unmanned Aerial Vehicle	1
SAW	Surface Acoustic Wave	3
OBP	Odorant Binding Protein	3
MEMS	Microelectromechanical Systems	5
SAW	Surface Acoustic Wave	5
IDT	Interdigital Transducer	7
TCD	Temperature Coefficient of Delay	20
PMMA	Poly(methyl methacrylate)	21
RIE	Reactive Ion Etching	29
DRIE	Deep Reactive Ion Etching	29
LACE	Laser-Assisted Chemical Etching	29
FIB	Focused Ion Beam	29
CVD	Chemical Vapor Deposition	31
LOR	Lift-Off Resist	32
CVD	Chemical Vapor Deposition	35
PECVD	Plasma Enhanced Chemical Vapor Deposition	36
OBP	Odorant Binding Protein	36
TPA	Transmission Parameter Analysis	37
IOA	Integrated Oscillator Analysis	37
SOLT	Surface, Open, Load, Through	41
VNA	Vector Network Analyzer	46
SEM	Scanning Electron Microscope	57

SURFACE ACOUSTIC WAVE DEVICES AS CHEMICAL VAPOR SENSORS

I. Introduction

1.1 *Motivation*

Chemical and biological-based surface acoustic wave sensors will be an important part of fulfilling the Air Force goal of global situational awareness (GSA). Additionally, developing a flexible sensor platform that can be biologically tailored to sense particular molecular targets will advance other goals of national interest, such as landmine removal, border security, and future biotechnology research.

A part of GSA, the Air Force Research Laboratories Focused Long Term Challenge (FLTC) # 3's stated goal is to have the ability to "detect, identify, tag, track, and target adversaries, improvised explosive devices (IED), and Chemical, Biological, Radiological, Nuclear, and Explosive (CBRNE) weapons in congested or concealed environments" [1]. In order to accomplish this goal, a flexible sensor platform is proposed which is able to signal the presence of a CBRNE target based solely on the molecular vapors it emits [2–4]. This sensor would be able to perform dual roles of active seeking and passive detection. If the sensor is mounted on a mobile platform, such as a micro unmanned aerial vehicle (UAV), it would be able to seek out and identify weapon caches and IEDs in an urban environment, providing vital information to allow the warfighter to engage these devices. A vapor sensor of this type could also be distributed in a passive UAV, building, or troop mounted sensor network, providing critical early warning in the case of a chemical or biological attack on our troops or citizens. This would allow the implementation of defensive measures to significantly reduce casualties [4]. Since chemical and biological weapons are becoming an increasingly important part of asymmetric warfare from both rogue states and terrorist organizations, the implementation of a passive sensor network is becoming increasingly critical [5].

With an estimated 127 million buried around the world, traditional landmines remain a dangerous threat to U.S. troops and global civilians [6]. Additionally, current technology is not sufficient to safely find and remove landmines, thus prompting further research, of which vapor sensors are a significant part [6, 7].

In order to prevent a terrorist attack on the American population, the security of our borders is paramount. To this end, one of the technologies that the U.S. Department of Homeland Security is soliciting in a recent Broad Agency Announcement is an explosive vapor sensor [2]. These could be installed in critical locations such as airports and seaports.

Finally, as biotechnology becomes an important part of our armed forces, an increase in biotechnology research is required [8]. By developing a sensor platform whose sensing agent contains a variable biological molecule, biotechnology researchers would be given an additional tool to be able to probe critical binding interactions [9]. Since much of this information currently comes from difficult to quantize fluorescent molecular labelling, an independent method to verify binding events would aid research.

1.2 Performance Goals

In order to successfully fulfill the above missions, a vapor sensor must provide high sensitivity, specificity, and speed, while at the same time being low cost and lightweight [4, 7, 8].

First, the sensor must be sensitive enough to detect the target of interest at sufficiently low concentrations for it to be operationally effective. In the case of chemical or biological substances, this level must be well before the lethal limits of the substance. This sensing requirement is different for specific substances, but is usually in the range of 1-500 ppm [4]. Due to the lower vapor pressure of explosives, devices made to detect them must be sensitive to concentrations below 1 ppb [7]. The device should provide a 99% chance of detection at or above these concentrations [4].

Second, the sensor must have high specificity, leading to low false-positives. It must be able to differentiate a particular vapor in the midst of a wide range of battlefield interferences and environmental conditions. The Army expects 97% detection specificity [4].

Third, the sensor must have a quick response time. In the case of a mobile probing sensor, a quick response time allows better localization of the vapor source. In a distributed network, the quick response allows personnel to take action sooner to mitigate the effects of an attack. The response time expected for sensing different vapors ranges from 10 seconds to 2 minutes [4].

Finally, the sensor must be designed to be low-cost and lightweight. These properties would allow effective deployment in the field [8].

1.3 Objective and Approach

Vapor sensors are generally made with a sensing element to interact with the molecules in the air and a transducer to convert the sensing signal into a form where it can be read out, such as an electrical frequency or voltage. Currently, highly sensitive and quickly responding vapor sensors are being made with a polymer layer as the sensing element and a surface acoustic wave (SAW) device as the transducing element [7, 10–14]. As vapors sorb into the polymer layer, the increased mass loading on the surface of the device changes the acoustic velocity of the surface wave, which can be read out with supporting circuitry. However, these devices are lacking in specificity, since most polymers will absorb a range of vapors out of the air [14–16].

In order to address the problem of specificity in SAW vapor sensors, the goal of this thesis is to explore the possibility of using biological molecules as an alternative to the polymer sensing element. The molecules, such as aptamers, DNA, or odorant binding proteins (OBP), have the properties of binding only to very specific molecular arrangements, leading to high specificity in addition to the already desirable sensitivity and response times of SAW sensors.

In order to accomplish this goal, several tasks must be accomplished. First, this project will include developing a process for reliably depositing metal down to 2 μm line widths at AFIT with the new mask aligner. Second, a variety of SAW designs will be designed using L-Edit, since SAW sensors are not mature enough to have an exact design laid out as the optimal sensor. Third, these devices will be fabricated in the AFIT cleanroom. After this, the devices will be characterized using a network analyzer and a wafer probe station. The SAW devices will be coated with a polymer sensing layer and subjected to initial vapor sensing tests. Fresh devices will then be functionalized with biomolecules and vapor sensing tests repeated.

II. Literature Review

The scientific community's understanding of molecular interactions has progressed rapidly over the last several decades. Scientists are now able to engineer polymer or biomolecule-based coatings to selectively adsorb analytes of interest. Meanwhile, the microelectromechanical systems (MEMS) community has been progressively shrinking the size of mechanical transducers down to the micron range and beyond. As the scale decreases, surface effects become more prominent in the mechanical response of a device. This allows the possibility of a sensor where the mechanical changes in a chemical sensing layer can be transduced using a MEMS device into a usable electronic signal. Surface acoustic wave (SAW) devices are one MEMS possibility with great potential for use as small, inexpensive, sensitive, and selective vapor sensors. This paper will discuss the background theory, device design, fabrication, characterization, and published uses of SAW sensor technology.

2.1 *Theory of SAW Devices as Vapor Sensors*

2.1.1 Piezoelectric Effect. SAW sensors rely heavily on the piezoelectric properties of certain crystalline materials in order to both generate and receive acoustic waves using electrical signals. Thus, in order to understand SAW devices, one must first gain a qualitative understanding of piezoelectricity, the phenomenon which couples the electric signal to the mechanical waves.

Some materials are crystalline; their atoms are arranged in groups of unit cells which are repeated periodically in the three dimensions of the crystal lattice. A crystal has a center of inversion symmetry if any vector r from the center to a point on the lattice can be matched with a vector $-r$ that points to an equivalent point. For those crystals that do not have a center of inversion symmetry, a mechanical deformation of the crystal lattice will change the distribution of charge in the unit cell, as shown in Figure 2.1.

The effects of numerous unit cells lead to a detectable charge on the crystal surface [18]. This relation between mechanical and electric properties is called the

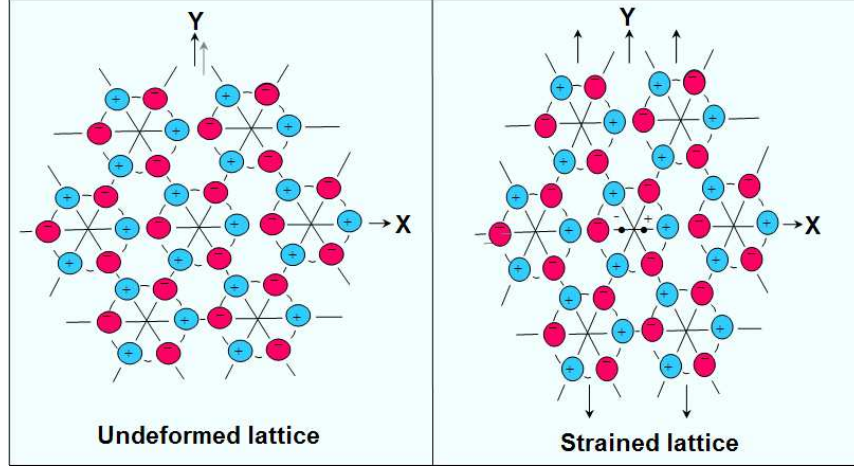


Figure 2.1: Strain can cause crystals without central inversion symmetry to form electric dipoles. In this case, as strain in one direction causes charge separation in a perpendicular direction. This inter-axial dependency requires tensor notation to fully characterize [17].

direct piezoelectric effect, which can be quantified using the material and direction dependent piezoelectric coefficients d_{ij} in the equation [19]

$$V_i = \frac{d_{ij} \Delta F_j x}{\epsilon A}, \quad (2.1)$$

where V is the voltage detected across the crystal, F is the force applied, x is the distance across which the voltage is measured, ϵ is the electrical permittivity of the crystal, and A is the area of the charged surface. The subscripts i and j are variables indicating direction. Note that due to the mechanical relationships between force, stress, and strain and the electrical relationships between charge, voltage, and electric field, there are several different ways to write the same effect [18, 20]. The converse of direct piezoelectric effect is also true: a voltage applied across a crystal will cause strain in the crystal [19]. SAW devices make use of both the converse and direct piezoelectric effect for generating and receiving acoustic waves, respectively.

2.1.2 Excitation of Acoustic Waves Using Interdigital Transducer. The harnessing of the piezoelectric effect in a SAW device is accomplished through the use

of interdigital transducers (IDT). Each IDT is composed of a pair of multi-finger electrodes patterned onto the piezoelectric substrate such that their fingers are interleaved as shown in Figure 2.2. A DC voltage applied between the pair of electrodes will form an electric field in the substrate, leading to semi-sinusoidal piezoelectric deformation of the crystal. Removing this voltage will then cause the crystal to relax back into its natural state, generating travelling acoustic waves along the surface of the substrate in both directions. The wavelength of these waves is constrained to exactly the periodicity of one side of the IDT fingers. For the most common IDTs with 50% metallization (i.e. the finger width is the same as the finger separation), the wavelength of the acoustic wave is four times the width of each electrode finger, d.

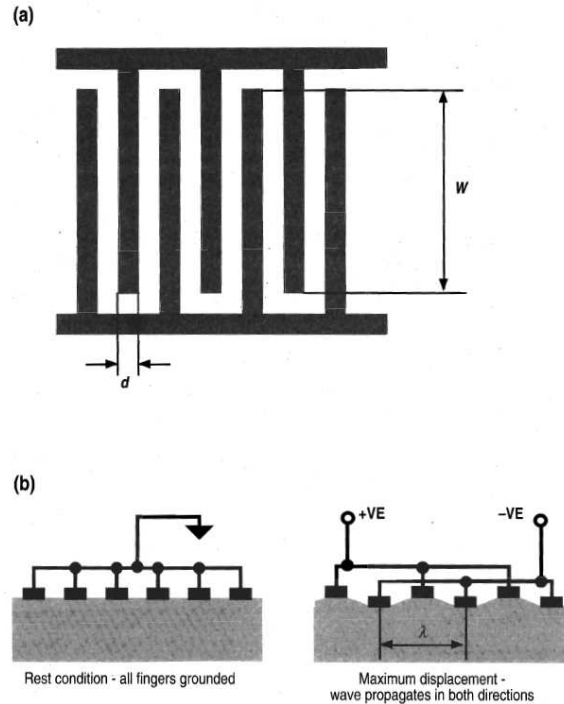


Figure 2.2: (a) A typical SAW interdigital transducer with finger width d and acoustic aperture W . This design also shows 50% metallization, meaning that the spacing between fingers is also d . (b) The design of the IDT allows the application of a voltage differential across linear regions of a piezoelectric substrate. This in turn causes wave-like deformation which will propagate in both directions under an AC voltage [20].

If an AC voltage is applied to the IDTs, the waves generated on successive cycles will interfere with each other. For the wave fronts to have total constructive interference, the frequency of the AC signal must satisfy the equation

$$f = \frac{v}{\lambda}, \quad (2.2)$$

where f is the frequency of the AC signal, v is the material and direction-dependent acoustic wave velocity, and λ is the acoustic wavelength. This ensures that the time taken for the acoustic wave to travel one wavelength equals the period of the wave generating signal, causing the newly generated wave to be exactly in phase with the existing wave. Any deviation from this center frequency will result in less than optimal wave interference leading to a decreased signal amplitude. Due to additive phase error, as the number of IDT fingers increases so does the interference at these off-center frequencies, leading to steeper frequency responses.

The time taken for a signal to propagate between transducers is directly related to the geometry by the acoustic velocity of the substrate, as inferred in Equation (2.2). Thus, one can look at the IDT as a spatially sampled version of the SAW device impulse response. This allows one to relate the IDT geometry to its frequency response using a scaled Fourier Transform either to predict IDT frequency response from a given geometry, or design the geometry to match a desired frequency response [21]. For the standard IDT configuration discussed so far, we see that the IDT fingers are spatially sampled versions of the $\text{rect}(t)$ function (ie. one pulse of a square wave) and can predict the frequency response

$$H_{total}(f) = \frac{N}{f_o} e^{-jN\pi(f-f_o)/f_o} \text{sinc}(N\pi(f-f_o)/f_o), \quad (2.3)$$

where N is the number of finger pairs in the IDT and f_o is the fundamental frequency due to spatial sampling which corresponds to the center frequency above resulting in complete constructive interference [20]. Equation (2.3) refers to the impulse response of a single IDT only. The full frequency response will include terms from both input

and output IDTs, as well as a term from the propagation path between them. This is written as

$$H(f) = H_{in}(f)H_{out}(f)e^{jL(f)2\pi f/v}, \quad (2.4)$$

where $H_{in}(f)$ and $H_{out}(f)$ are the frequency responses of the input and output IDTs, $e^{jL(f)2\pi f/v}$ is the phase delay due to the propagation path neglecting attenuation and $L(f)$ is the distance between the portions of the input and output IDTs sensitive to a certain frequency [21]. Only in the case of chirped IDTs is L a function of frequency, as discussed in Section 2.2.3. For constant finger separation, L is the constant length between the center fingers of the input and output transducers.

2.1.3 Substrate Acoustic Wave Propagation. After its excitation, the acoustic wave travels along the surface of the substrate in both directions perpendicular to the fingers of the input transducer. If the overlap of the input fingers, called the acoustic aperture, is greater than 30λ , then the SAW can be considered to have parallel wavefronts [18]. Particle motion can be transverse, having displacements normal to the surface, or compressional, having displacements along the axis of propagation, as shown in Figure 2.3. Generally, SAWs will be composed of both displacements, leading to elliptical particle motion. The proportions of the transverse and compressional displacements are both material, cut, and direction dependent. Because the most common SAW cuts and propagation directions involve significant transverse components, operation in a liquid environment is highly difficult due to the greatly increased attenuation from energy lost into the liquid [20]. The magnitude of particle displacement r in the wave decreases with depth into the substrate y according to the formula [18]

$$|r| \propto e^{-2\pi y/\lambda}. \quad (2.5)$$

We see that most of the displacement, and thus wave energy, is confined within one wavelength of the surface. This leads to devices that are highly sensitive to changes in the surface and environment.

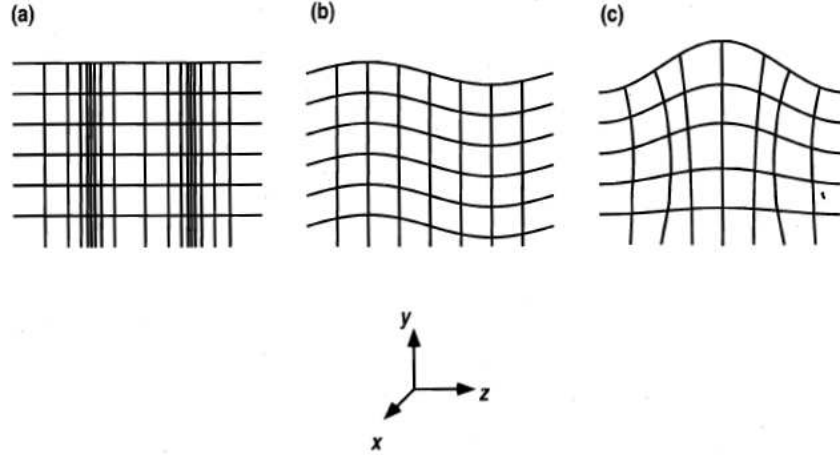


Figure 2.3: Surface Acoustic Waves can propagate in 2 different ways. (a) The displacement of particles is along the same axis z as the wave is travelling in compressional waves. (b) The displacement of particles is perpendicular to the axis of wave motion in transverse waves. This can occur either perpendicular or parallel to the surface. (c) Most surface acoustic waves are composed of the superposition of both compressional and surface-normal transverse waves [20].

2.1.4 Thin Films as Vapor Sensing Mechanism. In the simplest case of a surface acoustic wave travelling on a bare piezoelectric substrate, the wave velocity is usually specified as a constant for a certain material-direction combination [18, 20, 21]. Often a thin polymer film is deposited on the substrate surface between the input and output IDTs. In this case, the velocity of the surface wave will depend not only on the material parameters of the substrate as detailed in Section 2.2.2, but also on the more variable properties of the thin film. Both the wave's velocity and attenuation may become dependent upon the mass of the film, the operating temperature, environmental air pressure, stiffness of the film, the dielectric constant of the film, and the surface conductivity [18]. If molecules in the environment adsorb into the film, the material parameters of that film may change, leading to a change in wave velocity and attenuation. As the polymer films are designed to specifically adsorb only certain types of molecules, changes in the film due to adsorption can be related to the type and concentration of target molecules in the gas flow. The three primary sensing mechanisms that alter wave velocity in a SAW polymer sensor are

the mass-loading, acoustoelectric, and viscoelastic effects [22]. Note that much of the following theory on polymer sensing films on SAW devices is also applicable if the thin film is biologically based [23–25].

The mass-loading effect comes from the increased kinetic energy density required to move the larger sheet mass density resulting from the adsorbed molecules. Thus, an increase in mass per unit area will increase the energy density, which decreases the acoustic wave velocity linearly according to the relation

$$\frac{\Delta v}{v_o} = \frac{\Delta U}{U_o}, \quad (2.6)$$

where U represents energy density [18]. Combining this with the expected energy density shift from each of the directions of particle velocity yields

$$\frac{\Delta v}{v_o} = -c_m f_o \Delta \rho, \quad (2.7)$$

where $\Delta \rho$ is the change in ratio of mass/area of the film to to adsorbed molecules, and c_m is the mass sensitivity factor

$$c_m = \frac{\pi v_o}{2} \left(\frac{v_{xo}^2}{\omega P} + \frac{v_{yo}^2}{\omega P} + \frac{v_{zo}^2}{\omega P} \right). \quad (2.8)$$

The $v_{io}^2/\omega P$ terms are substrate material constants that relate particle velocity to energy density at a certain frequency [18]. P refers to the acoustic power input to a differential volume of particles. One could also think of the mass-loading effect as an increased inertia in the film corresponding to the inductor in a distributed transmission line. This is the effect most relied upon in many vapor sensing devices, which can measure the change in velocity by looking at a phase or frequency shift, as detailed later [10, 11, 15, 24, 26, 27].

The acoustoelectric effect deals with the wave of surface charge that accompanies the acoustic wave due to the piezoelectric effect. Energy will be stored in the associated electric fields. Changes in the conductivity or permittivity of the film will

also have an effect on the energy, and thus the interdependent wave velocity [18]. Note that most polymer sensing films will have very low constant conductivities, thus this term can be neglected in these cases. Only when adding metallic thin films or expecting a change in film conductivity does this term need to be accounted for. However, if one is expecting vapor adsorption to cause a conductivity change but does not want to have the velocity affected, using a thin metal film to short out the electric field should remove the acoustoelectric effect [22].

The viscoelastic effects occur due to the deformation of the thin film by the acoustic wave. The thin film will have a characteristic shear modulus, G , which will be mostly real if the film is elastic [18]. As vapors adsorb into the thin film, the film may swell increasing its thickness and changing the characteristic shear modulus. The resulting change in wave velocity is given by

$$\frac{\Delta v}{v_o} = 4c_e \frac{f_o}{v_o^2} \Delta(hG'), \quad (2.9)$$

where c_e is the coefficient of substrate elasticity, h is the film thickness, and G' is the real portion of the shear modulus [22]. Thus, most adsorption will lead to a velocity increase. This is not always the case, as at higher gas concentrations, the vapor may begin to soften the polymer layer through solvent plasticization, leading to a lower hG' product and a velocity decrease [20]. This causes the vapor concentration-acoustic velocity curve to no longer be a one to one function, leading to difficulties in extracting an unknown gas concentration from measurements. Note that using the imaginary portion of the shear modulus in the same equation yields $\Delta\alpha/k$, the change in the SAW attenuation rate [22], where the wave number $k = 2\pi/\lambda$.

The acoustic wave velocity changes due to the mass-loading and viscoelastic effects are generally in opposite directions, leading to reduced overall sensitivity. In order to maximize sensor response, it is desirable to design the sensor such that one effect will dominate. Thompson, *et al.* defines this primarily on the rigidity of thin sensing film as a function of temperature. Every thin film has two glass transition

temperatures T_a and T_g where significant changes in specific heat and thermal expansion occur. If the sensor is operated in a region significantly below these temperatures, the film is highly rigid, and mass-loading effects dominate. As the operating temperature approaches T_g , the film becomes more and more rubbery and the viscoelastic effects eventually equal or slightly overcome the mass-loading effects [20].

One can look at this from a different perspective by defining two types of thin films: acoustically thin vs. acoustically thick. The molecules at different depths of an acoustically thin film will have displacements in phase with each other, leading to rigid responses. Conversely, the surface molecules of acoustically thick will have displacements that lag in phase compared to those beneath it. In other words, they will act more rubbery, leading to the possibility of film resonance and higher attenuation. Determining whether a film acts acoustically thick or thin depends on the ratio

$$R = \frac{A f_o v_o \rho h}{|G|}, \quad (2.10)$$

where A is a substrate-dependant constant which has a value of 1.9 for ST-cut quartz [18, 20], ρ is film density, h is the film thickness, and G is the shear modulus. If $R \ll 1$, then the substrate can be considered acoustically thin. This is beneficial, since analytical expressions for the viscoelastic effect are most accurate here, and anomalous readings from film resonance can be avoided [20].

Acoustic velocity changes in the pathway of the acoustic wave result in a change in the phase shift of the device frequency response according to Equation (2.4). Additionally, anything that increases the attenuation constant will cause the magnitude of the output to drop as well. This is often referred to in the SAW community as an increased insertion loss and is measured in dB. Either the phase shift or the increased insertion loss due to changes in the sensing layer can be used to determine whether or not the target molecules are present. Further details on the electronic setups of these sensing schemes will be shown later in this paper.

2.2 *Design of SAW Devices for Sensing Applications*

While SAW devices have found wide uses as filters in RF and microwave systems, the optimization of SAW sensors is not nearly as mature. This section will address current knowledge about sensor design based upon theory of SAW operation. In some cases, exact analytical optimizations are not known or easily solvable, and SAWs are experimentally found to work best under certain design specifications.

2.2.1 Effects of SAW Geometry. The deposition thickness of the metal fingers can affect both the electrical and mechanical aspects of the SAW system, and thus must be designed with both in mind. From an electrical point of view, thick finger electrodes lead to lower resistance, providing a good electrical contact. If the fingers are too thin, their electrical resistance becomes a significant factor that leads to higher circuit loading and insertion loss [21]. Conversely, having thicker or heavier fingers leads to an increased impedance to the transmission of the acoustic wave [18]. The first effect of increased impedance is to lower the average acoustic velocity underneath the fingers, reducing the center frequency according to Equation (2.2). Secondly, the periodically changing acoustic impedance leads to complicated partial reflections of the wave which can alter the ideal frequency response. Campbell suggests a layer of 500-2000 Å aluminum (Al) as a good compromise between the electrical and mechanical considerations. Ballantine agrees with a suggestion of 1000 Å Al, but points out that 1000 Å of gold with a chromium adhesion layer may also be a good choice to prevent electrode deterioration due to oxidation.

If the SAW sensor is configured within an electrical circuit as the frequency selective component of an oscillator, any change in the velocity of the acoustic wave will correspond directly to a change in the frequency of oscillation of the entire system. Specifically,

$$\frac{\Delta v}{v_o} = \frac{\Delta f}{f_o}. \quad (2.11)$$

This is due to the linearity of the IDT's phase response in the region near the center frequency. The change in velocity will cause a shift in the phase of the frequency

response, thus the phase response corresponding to the condition of oscillation will be correspondingly moved in frequency. More detail will be covered in the section on oscillators. Using Equations (2.11) and (2.7), one can find [18] the relation

$$\frac{df}{d\rho} = -f_o^2 c_m. \quad (2.12)$$

Thus, the change in frequency due to an adsorbed mass (the mass sensitivity) is proportional to the square of the center frequency. This upwards trend has been verified experimentally, although the data does not support the complete f_o^2 factor [10, 11]. Thus, to make highly sensitive devices, one would like to increase the center frequency of the device. According to Equation (2.2), there are two ways to accomplish this. One can either increase the natural acoustic velocity by choice of substrate or decrease the acoustic wavelength λ . Since the acoustic wavelength is determined by the IDT finger periodicity, this periodicity should be minimized. One is limited in increasing the center frequency ad infinitum by two factors. First, technology and cost contribute restrictions to minimum manufacturable line sizes. This can be abated fairly easily by operating the SAW at a higher harmonic [7, 18]. The second factor refers back to Equation (2.3), where one sees that higher frequencies decrease the amplitude of the frequency response, leading to more difficult oscillations. As a consequence, most SAW sensors operate in the range of 0.1 - 1 GHz.

Another point that can be gleaned from Equation (2.3) deals with the design parameter N , the number of finger pairs in the IDT. We see that the amplitude of the frequency response increases with N . This intuitively makes sense, since we expect that constructively adding acoustic energy from more fingers would increase the total acoustic energy transmitted. This is a benefit to the system, since additional frequency response amplitude aids circuit oscillation. Perhaps more significantly, increasing N causes the periodicity of the sinc term to decrease, as shown in Figure 2.4. This causes the main lobe to sharpen, leading to increased frequency stability, a key design goal in SAW sensors [18]. At the same time, there is higher attenuation

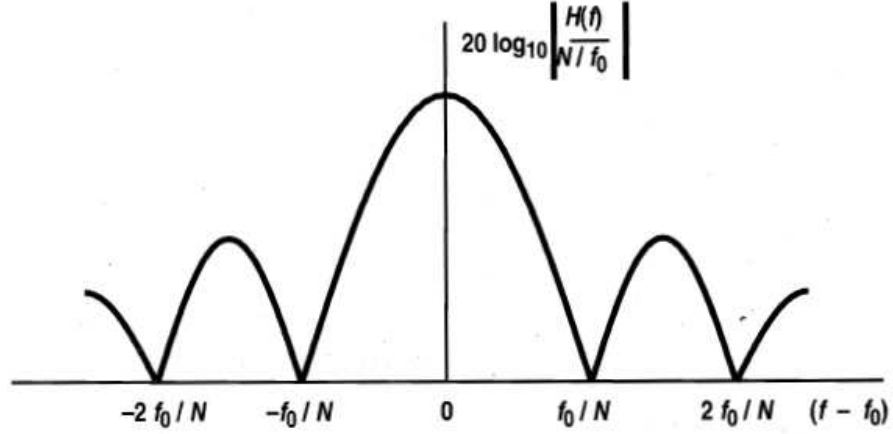


Figure 2.4: The periodicity of the frequency response is determined by f_0 and N . As N increases, the primary lobe narrows and the side lobes move in closer [20].

of unwanted frequencies [20]. N is also directly related to the phase term in Equation (2.3). Increasing N increases the phase vs. frequency slope. While this will lower mass sensitivity in the electrode region, it also reduces frequency noise due to phase fluctuations in the electronic circuitry. While increasing N begins by giving positive benefits, this is only to a point. As N increases, the mass-loading of additional finger pairs begins to overcome the added benefits. At the same time, the added benefits of high N begin to decrease due to increased reflectivity [18] Only a small portion of the signal generated by a finger pair on the outermost end will make it through the IDT, which acts like a Bragg reflector to the acoustic waves. For these reasons, most groups have found that SAW sensors work well when the number of finger pairs is in the range of 50-160 [18, 24, 28].

As mentioned earlier, the acoustic aperture should be at least 30λ to ensure parallel wavefronts. If this is not the case, the waves must be considered partially curved. This is undesirable since the different portions of the curved wavefronts will intersect the output transducers out of phase with each other, resulting in reduced gain. There seems to be no significant tradeoff driving lower acoustic apertures other than overall device size on chip, thus many researchers design for an acoustic aperture in the range of $70 - 200 \lambda$ [11, 13, 24, 28].

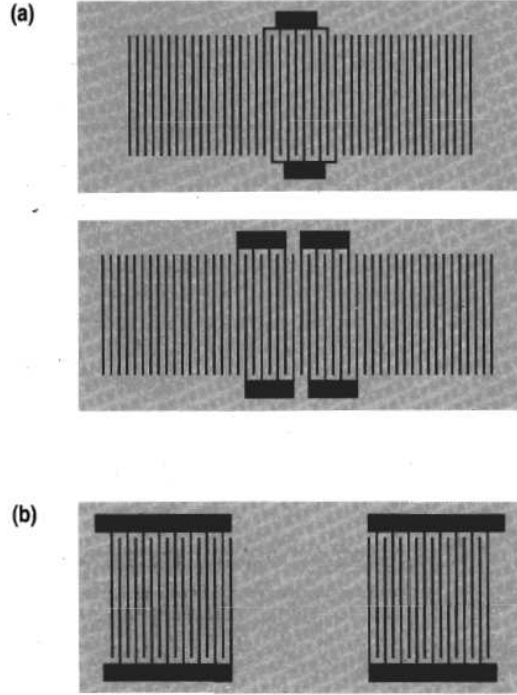


Figure 2.5: A SAW device can be designed to act in one of two modes. In (a), the device is in a resonator mode. The SAW is generated by one transducer, then is reflected back and forth between the IDTs and reflection gratings, setting up a standing wave that is sampled by the output. This can be a one or two-port device. In (b), the SAW is in a delay line configuration. The SAW travels directly from input to output, with a large enough path to accumulate phase and attenuation changes due to the sensing mechanism [20].

There are two different modes a SAW device's geometry can be designed towards. In Figure 2.5a, the SAW is generated by one transducer, then is reflected back and forth between the IDTs and reflection gratings, setting up a standing wave that is sampled by the output. This is referred to as resonator mode, and can be made as either a one or two port device. The space between the IDTs is kept small in order to reduce attenuation and more easily set up the standing wave. In Figure 2.5b, the SAW is in a delay line configuration. The SAW travels directly from input to output, with a large enough path to accumulate phase and attenuation changes due to the sensing mechanism. This is the configuration more often used in sensor designs.

When using a delay-line SAW device in an oscillator system, stable oscillation requires a multiple of 2π phase shift in the closed loop, as will be detailed later. We can write this as

$$\frac{\omega L}{v} + \phi_E = 2\pi n, \quad (2.13)$$

where ω is the phase shift due to the SAW delay-line, L is the distance from the center of the input IDT to the center of the output, and ϕ_E is the phase shift due to the external circuit [20]. Since phase noise in the external circuit is a major factor in frequency stability, one can rearrange Equation 2.13 and take partial derivatives with respect to frequency and external phase shift, resulting in the equation

$$\frac{\delta f}{f} = -\frac{\delta \phi_E \lambda}{2\pi L}, \quad (2.14)$$

which relates the phase noise in the external circuit to its contribution to oscillator frequency noise [20]. One can see that as L is increased, the contribution of phase noise to overall frequency noise is decreased. Thus, one should increase L , though keeping in mind that doing so also increases the attenuation of the SAW wave. Ballantine suggests values in the range of $200 - 400\lambda$ [18]. Note that this analysis also applies to resonator SAW devices, but their L is a more complicated function of geometry and reflectivity.

2.2.2 Material Considerations. In designing a SAW device, one should give proper attention to the substrate material, as its selection decides several key properties. A few of these properties for common substrates are given in Table 2.1, while others can be found in Slobodnik's handbook [29]. Note that many of these properties are also cut- and direction-specific, thus several values may be found for the same material, although this is not apparent from the data in Table 2.1. Most SAW substrates are made of bulk piezoelectric material. However, some materials such as ZnO or AlN can be grown as a crystallographically-aligned epilayer if necessary [18,20].

Table 2.1: Properties of Several Common SAW Substrate Materials [18, 20, 21]

Substrate Cut/ Propagation Direction	Propagation Velocity ($\times 10^5 \text{ cm/s}$)	$v_{xo}^2/\omega P$	$v_{xy}^2/\omega P$ ($\times 10^{-6} \text{ cm}^{1/2} \text{ g}^{1/2}$)	$v_{xz}^2/\omega P$	K^2	C_s (pF/cm)	TCD (ppm/ $^\circ\text{C}$)
Quartz ST X	3.158	0.13	1.34	0.88	0.0011	0.5	~ 0
Lithium Niobate -Y X	3.488	0	0.83	0.56	0.048	4.6	94
Gallium Arsenide Z X + 22.5°	2.763	0.16	1.22	0.91	0.0007	1.2	35

One important material property is a material's natural acoustic velocity. This is set by the mechanical properties of the material, such as its shear modulus, density, and, in the case of piezoelectrics, conductivity. Earlier it was shown that high frequency operation is key to mass sensitivity. From Equation (2.2), it can be seen that a higher substrate acoustic velocity will result in a proportionally higher frequency, raising the sensors mass sensitivity according to Equation (2.12).

The other term in Equation (2.12), c_m , is also material-dependent according to Equation (2.8). It deals with the ratio of magnitude of the instantaneous particle velocities to power density. If one calculates the right hand side of Equation (2.12) for each of the materials in Table 1, it is found that quartz has the highest overall mass sensitivity, followed by lithium niobate and gallium arsenide in ratios of 7.4:5.9:4.8, respectively. Thus, even though lithium niobate has the superior acoustic wave velocity, it is unexpectedly overcome by quartz's higher particle velocities.

Another material consideration is the electromechanical coupling factor K^2 , which represents the magnitude of the piezoelectric coupling. A higher K^2 means that the substrate is deformed more in an electric field. This increases the magnitude of the frequency response at both the input and output transducers, lowering the insertion loss of the sensor and reducing the number of finger pairs necessary [18]. Since low

insertion loss is a key factor in oscillator stability, a high K^2 value is considered beneficial [28].

The presence of long parallel conductors in the IDTs leads to a highly capacitive electrical input impedance. Since the fingers are not in a parallel plate configuration, one must use a much more complex method to estimate the capacitance [20]. The electric field lines pass through the substrate, the capacitance is dependent upon the material's permittivity. If one is planning to impedance match the SAW device into an electrical system, this becomes a factor to consider.

All material substrates expand and contract due to thermal expansion. Coupled with these motions are often changes in other material properties, such as shear modulus and density. These temperature effects are all combined into another important material property, the temperature coefficient of delay (TCD), which quantifies the expected change in velocity vs temperature. Since one does not generally want to sense temperature changes, this property should be minimized. The ST cut of quartz has nearly zero TCD around room temperature. SAW devices based on a piezoelectric epilayer can be built on a composite stack of other materials in order to minimize this coefficient. Additionally, a reference sensor could be used to attempt to subtract away changes due to temperature effects, though this does not work perfectly.

Apparently, quartz is the material of choice for SAW sensor designs. Although LiNiO_3 has a higher piezoelectric coefficient, quartz's overall mass sensitivity, low capacitive coupling, and TCD challenge this. Additionally, the quartz industry is fairly mature, reducing cost and increasing reliability.

2.2.3 Enhancement Techniques. There are several proposed alterations to the basic SAW sensor that may be able to improve its performance. The first is the introduction of non-planar surface morphologies to the sensing region. Thompson states that non-planar surfaces generally reduce the acoustic velocity and increase attenuation due to scattered energy into the bulk [20]. However, several articles recently disagree with this. In one, the authors perform COMSOL simulations of nanopillars

in the delay-line of a SAW device and claim its insertion loss is more sensitive to simulated poly(methyl methacrylate) (PMMA) depositions, though the graphs provided only show minor differences [30]. Penza, *et al.* gives a more convincing argument by showing experimental data that the frequency sensitivity of SAW sensors increasing by a factor of two with the addition of carbon nanotubes to their polymers [10]. In 2004, a student working under Bill Hunt at Georgia Institute of Technology performed research with photonic crystals in the delay line [31]. The results were inconclusive, though there does not seem to be any related papers from the group since then. None of the authors gave reasons why non-planar surfaces would enhance the sensitivity, though it might be inferred that the main reason is to increase surface area, adsorbing more molecules. Another option is since some carbon nanotubes are conductors, there is the possibility that these devices would have complementary mass-loading and acoustoelectric effects, increasing sensitivity over mass-loading only devices.

Due to the Fourier relation between transducer geometry and frequency response, a particular frequency response can be obtained by weighting the amplitude of the input signal at different locations. Since all of the fingers are connected electrically, the weighted amplitude comes from differing the overlap distance between the fingers of opposite electrodes in a process called apodization [21]. An example of this is shown in Figure 2.6. This is commonly used in the filter community to shape bandpass filters by apodizing the fingers according to a $\text{sinc}(x)$ function to yield a rectangular frequency response. Some are attempting to apply these ideas to sensors in order to reduce side band energy and increase overall frequency stability, leading to higher sensitivity. For instance, Ying, *et al.* use a \sin^2 apodization in their mass sensor which nearly eliminates the characteristic side lobes of the standard IDT $\text{sinc}(f)$ frequency response [32]. However, this apodization widens the main lobe and increases the insertion loss of the SAW device as well, as has been shown using MATLAB in Figure 2.7. Ying, *et al.* do not give comparative data or come to any conclusions regarding the appropriateness of apodization to SAW sensing. Figure 2.8 shows a va-

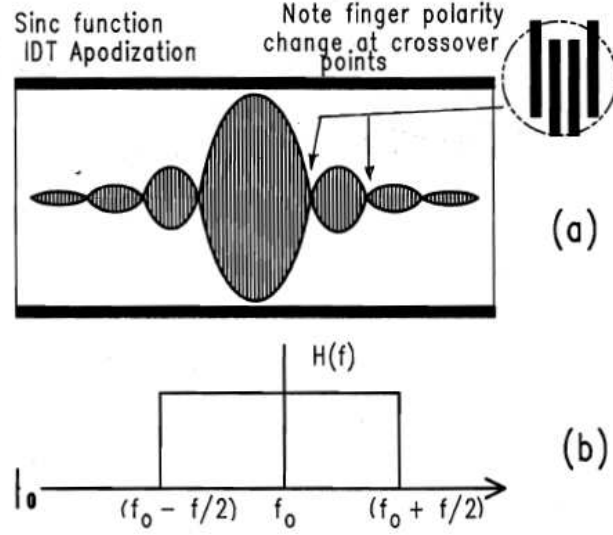


Figure 2.6: (a) Some SAW devices are designed with varying overlap between their fingers using a design method called apodization. This is an example of $\text{sinc}(cx)$ apodization. Note the doubled finger due to polarity change. (b) The expected frequency response is the Fourier pair of the IDT geometry. For a sinc geometry, a rectangular response is expected [21].

riety of other apodization schemes, none of which match the unapodized/rectangular IDT in performance.

When using an IDT to generate Rayleigh surface acoustic waves in the delay-line, other unwanted acoustic waves can be generated as well. First, the standard transducer generates SAWs in both directions, thus only half of its power is propagated in the forward direction. Additionally, the IDT will generate bulk waves as in Figure 2.9, which are a different mode entirely. Not only do these unwanted surface and bulk waves reduce the amount of energy coupled into the desired acoustic wave, but they may reflect into the path of the output transducer, generating significant amounts of noise. To reduce the effects of the unwanted surface waves, one could deposit a strip of acoustically absorbing material such as a thick polymer onto the surface of the device, cut the substrate at an angle to the wave propagation to reflect the waves away from the device, or create a unidirectional transducer through non-uniform finger geometry [20, 28]. To reduce the effects of bulk wave interference, one

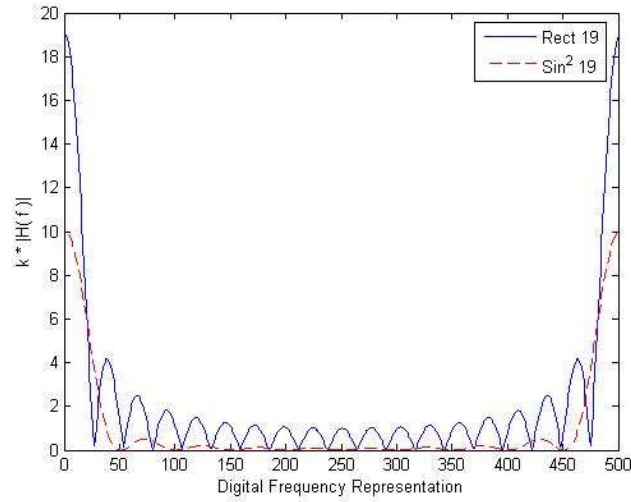


Figure 2.7: When using a \sin^2 apodization geometry, the side bands are nearly eliminated at a cost of reduced gain and wider bandwidth. (19 refers to the number of finger pairs.)

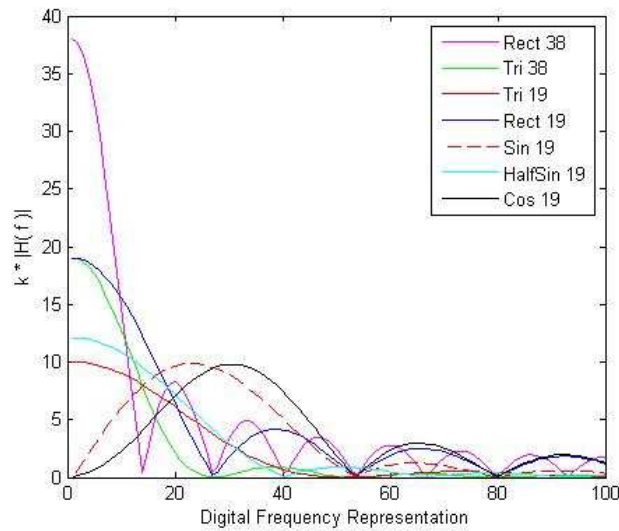


Figure 2.8: A variety of other IDT finger apodizations are proposed. A simple rectangular apodization (unapodized) is preferable with high gain and narrow bandwidth. (19 or 38 refers to the number of finger pairs.)

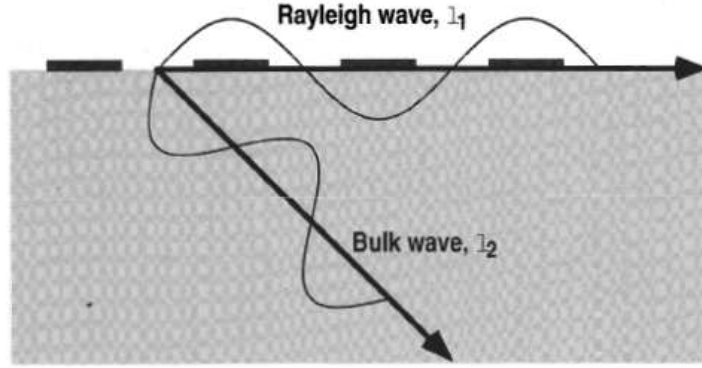


Figure 2.9: The IDT will launch acoustic waves that travel through the bulk rather than on the surface. These will have a different wavelength and preferential angle of radiation [20].

can leave the back surface roughened to scatter the waves, coat the back side with an absorbent material, or pattern an IDT-like grating structure on it [20].

Another enhancement technique is to use Chirped IDTs, a process where the finger width and spacing is not constant over the length of the IDT, as shown in Figure 2.10. In this manner, changes in frequency also change the effective distance of the delay-line. Some results have claimed a factor of 35 sensitivity increase using this technique, although Yadava disagrees with mathematical reasoning in his paper [27]. He does conclude that a different chirp method would theoretically give infinite sensitivity, but this has not yet been accomplished [27].

2.3 MEMS Fabrication Techniques

As the size of a structure decreases, traditional macroscale fabrication techniques become more difficult to implement. As a result, in order to fabricate MEMS device transducers, sensors, and optical structures having features on the micron scale, an entirely new set of fabrication techniques is required. Generally, these techniques fall into three broad categories: bulk micromachining, surface micromachining, and micromolding.

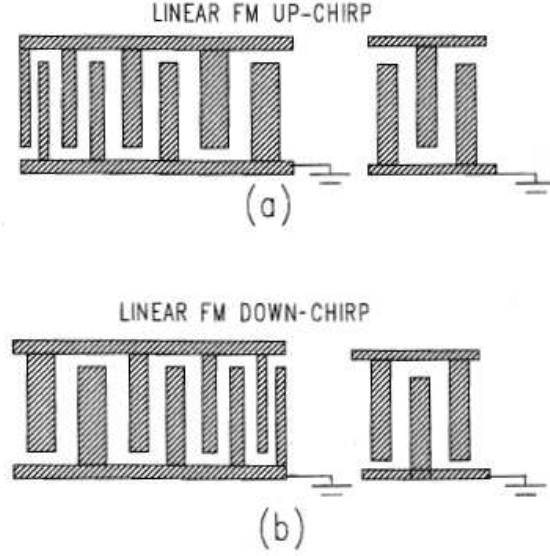


Figure 2.10: The finger width and spacing is not constant for a chirped IDT. (a) is a Linear Up-Chirp IDT, where the frequency increases linearly with increasing L . (b) is a Linear Down-Chirp IDT [21].

Almost all of the techniques that are used to fabricate MEMS devices require a method of patterning. Following in the footsteps of the microelectronics industry, much of this patterning is done using photolithographic methods. In a photolithography process, the substrate is coated with a light-sensitive polymer film called photoresist. When exposed to light, the polymers in the resist become either more or less cross-linked, leading to a change in solubility. These are called negative and positive photoresists, respectively. By shining light on the resist through a mask, only certain areas of the polymer layer are exposed. These areas can then selectively be removed with a developer solution, leaving a patterned thin film on the substrate. This film can then be used in a variety of ways, such as a protective layer during an oxide etch as in Figure 2.11.

Photolithography is generally classified by the wavelength of light used to expose the resist. The most common of these is ultraviolet (UV) lithography, using wavelengths such as the 365 nm I-line. Since the wavelength of light is directly related to the minimum feature size possible, the industry also uses deep UV sources such as the 248 nm or 193 nm excimer lasers to produce line widths as low as 22 nm [34].

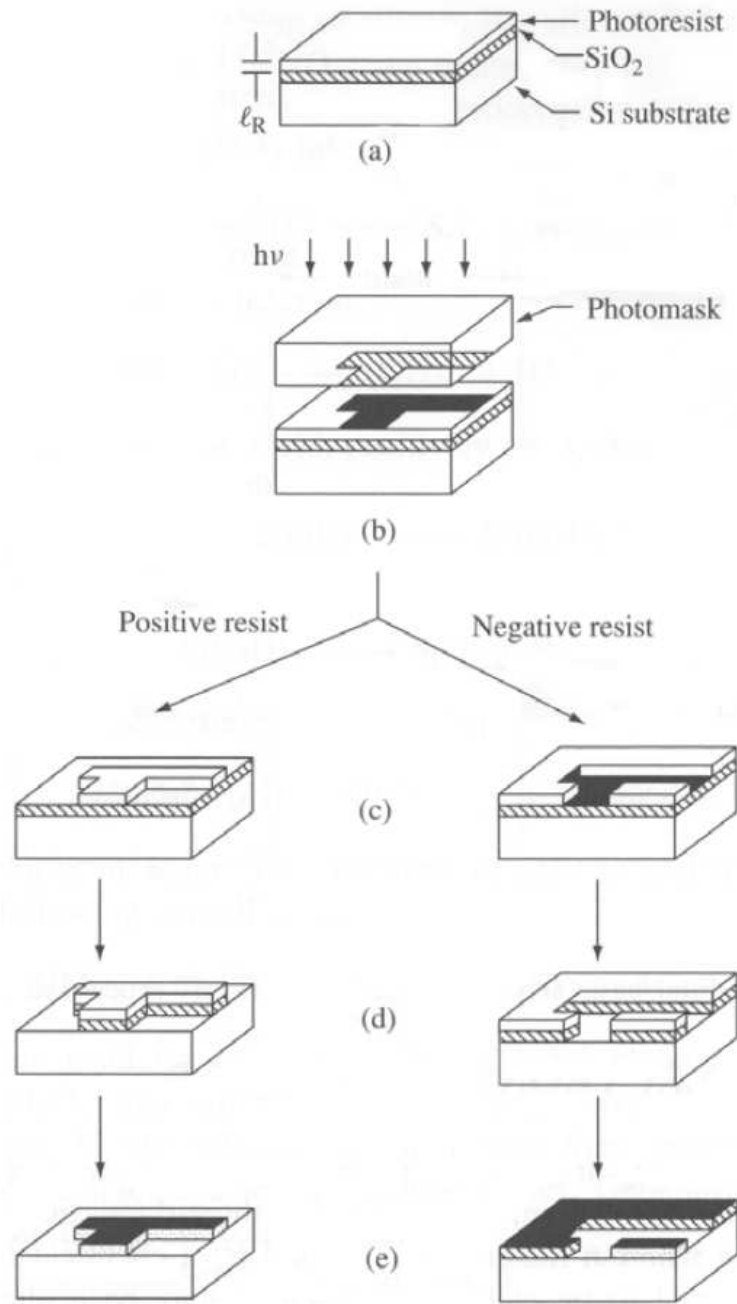


Figure 2.11: Photolithographic patterning of an oxide (a) Oxidized substrate is coated with photoresist. (b) Resist is selectively exposed through a photomask. (c) Developing creates a pattern. (d) Photoresist acts as protective layer during etch. (e) The resist is removed with an organic solvent [33].

As wavelengths decrease, photon-matter interactions change drastically, leading to increasing difficult and expensive lithography tools. Lithographic systems using extreme ultraviolet (EUV) or X-ray wavelengths are currently being researched. Alternatively, electrons, which have a significantly smaller effective wavelength, can be used in place of photons. This method, known as electron-beam lithography, provides increased resolution past 10 nm at the cost of lower device throughput [33,35,36].

2.3.1 Bulk Micromachining. Bulk micromachining deals with subtractive processes in which the substrate itself is selectively etched through a variety of processes into the desired structure. These processes include both wet and dry chemical etches, plasma or reactive ion etches, and laser etching [19]. These can be anywhere on a scale from completely isotropic, etching the material equally in all directions, to completely anisotropic, which can create high aspect ratio structures.

Many wet chemical etches can be used in MEMS fabrication, the selection of which depends on a wide variety of factors such as substrate material, available etch stop layers, etch rates, compatibility with other materials, and mask selectivity [19]. The substrate is generally masked using photolithography and the sample immersed into an etchant for a set period of time. If the photoresist is not sufficient to mask the wafer in a particular etchant, a secondary layer such as an oxide may be patterned by the resist to act as a hard mask. Often some form of agitation is used in order to increase the etch rate by speeding the delivery of fresh etchant to and removal of byproducts from the etching locations. By inserting a layer resistant to a certain etchant into the substrate through methods such as ion implantation, the depth of the etch can be controlled as shown in Figure 2.12. Wet chemical etching can also take advantage of the differences in etch rates for different crystallographic directions in many substrates to produce highly-predictable anisotropic etches. An example of this is shown in Figure 2.13.

Dry chemical etches can also be used to etch substrate materials. These processes use reactive chemicals in vapor phase to produce highly controllable etches in

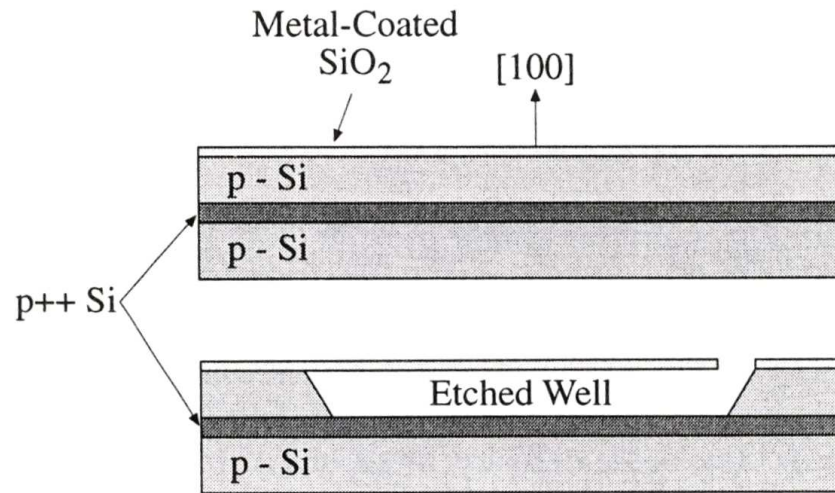


Figure 2.12: Doping Layers can act as an etch stop layer in silicon in making the well underneath this cantilever [19].

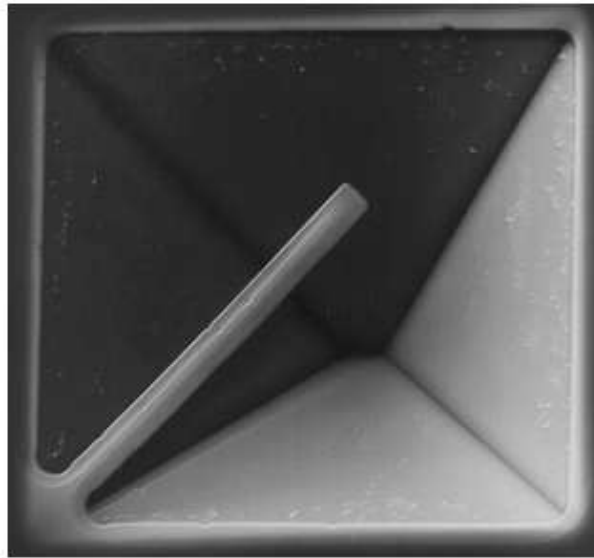


Figure 2.13: The anisotropic wet etch of $\langle 100 \rangle$ silicon in KOH produces an inverse pyramidal pit with faces in the $\langle 111 \rangle$ direction. The cantilever is formed from silicon dioxide and aluminum, and thus is not etched [37].

materials. These are almost entirely isotropic etches, and tend to have high selectivity towards masking layers. Common dry etchants include xenon difluoride, interhalogens, and hydrofluoric acid (HF) [19].

Plasma etching similarly uses chemical reactions out of the vapor phase in order to etch the substrate. The main difference is that radio frequency (RF) energy is coupled into the plasma to provide the energy for reaction rather than elevated temperatures. A variety of plasma etch types are available from isotropic to highly anisotropic. Depending on the positioning of the ground electrode, this process may also be called reactive ion etching (RIE) [19].

By changing the RIE process to periodically switch between etching and protective layer deposition, very high aspect ratio etches can be achieved. This is called a deep reactive ion etch (DRIE). The sidewalls can be very nearly vertical in this process, with wells reaching as deep as 1 mm [19].

Lasers can also be used to micromachine most substrates by directed ablation. Since this must be done serially, laser ablation is a slow process. Lower energy lasers can also be used to speed the etch rate of the substrate in the presence of certain gases, but care must be taken with the chemistry of different substrate-gas mixtures. This is called laser-assisted chemical etching (LACE) [19].

A focused ion beam (FIB) can also be used to etch a wide range of materials. Ions are accelerated and focused electrostatically before bombarding the substrate. Upon impact kinetic energy is transferred from the ions to atoms on the surface of the substrate, some of which are ejected. The resolution of a FIB system can be as low as 4 nm [38].

Bulk micromachining also commonly uses wafer bonding to assemble final devices. Multiple wafers that have already been etched appropriately are physically bonded together using some combination of adhesives, temperature, pressure, and electrical fields. Methods have also been developed that directly bond surface combi-

nations such as metal and oxide, silicon and silicon, or oxide and oxide without the use of an adhesive.

2.3.2 Surface Micromachining. Surface micromachining includes processes where thin films are added, patterned, and etched on top of a substrate in order to produce structures with features on the micron scale. A variety of films can be added, such as metals, dielectrics, and polymers. With a wider variety of materials and processes, more intricate devices can be made with surface micromachining as compared to bulk micromachining.

An important property in depositing thin films is the type of step coverage, which denotes how consistent the angle of incoming molecules is upon hitting the surface. This affects the consistency of film thickness when the height of the underlying layer changes. For instance, a process with vertically directional step coverage will result in almost no deposition on the side walls of the underlying layer, but a non-directional process will have conformal side walls on approximately the same order of thickness as the rest of the device. This is illustrated in Figure 2.14.

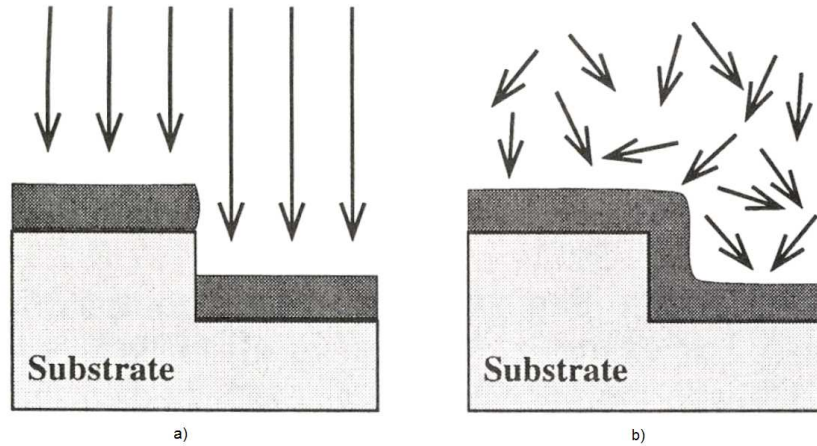


Figure 2.14: Step coverage a) Vertically directional processes do not coat side walls b) Non-directional processes produce conformal coverage [19].

One method of thin-film deposition is called evaporation, where a sample of the desired film is heated until it vaporizes. Since this is generally done under a

vacuum, the evaporated molecules then travel directly outward from the heating area until they arrive at the surface of the sample, where they adhere. By placing the substrate a distance away from the heating element, highly directional coverage can be obtained. Two methods of evaporating the sample are commonly used: a resistive heating element and a scanned electron beam [19].

Sputtering is another common method of thin film deposition. Chemically inert ions are accelerated towards a target using a high voltage. Upon impact, these ions eject material from the target which can then land on the substrate. Sputtering tends to yield both higher quality thin films and better substrate adhesion than evaporation, but also creates conformal films, which are not always desirable [19].

Direct deposition of a material from a reactive vapor to the substrate is also possible in a process known as chemical vapor deposition (CVD). Advantages can include high film uniformity and conformal step coverage [35]. This usually requires high temperatures unless assisted by an energetic plasma (PECVD) [35]. Other variants of CVD include low-pressure CVD (LPCVD) and metalorganic CVD (MOCVD) [33].

Electroplating is a common technique for depositing metals, especially when thicker layers are required. The areas to be electroplated are held at a negative voltage compared to an electrode and both are immersed in a solution containing reducible metal ions [19]. The electrons provided by the voltage allow the ions to be reduced at the wafer, thus depositing onto the surface. Commonly a metallic seed is deposited over the entire wafer to provide electrical contact. This layer can be selectively protected by photoresist, only allowing electroplating in the exposed regions. After growing the metal layer, the seed layer can be etched away to remove electrical conductivity between structures, as shown in Figure 2.15 [35].

Sacrificial layers are commonly used in MEMS fabrication, as also shown in Figure 2.15. A layer of material such as an oxide or photoresist is patterned onto the surface as a structural template or spacing layer. After further layers are deposited above it, the sacrificial layer can be selectively etched away, leaving a void. One

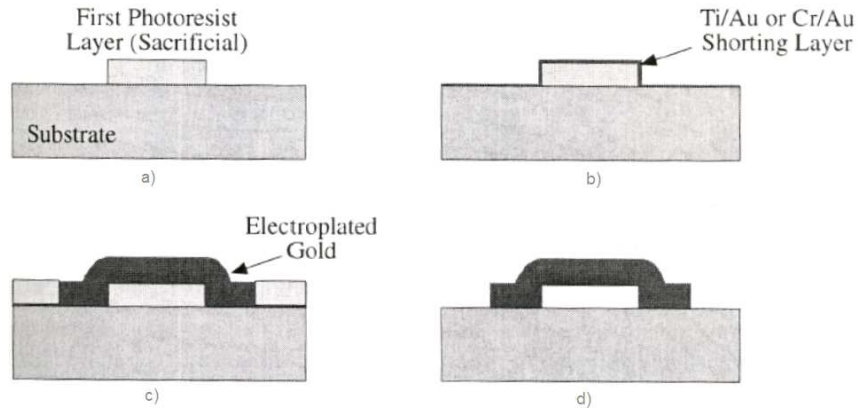


Figure 2.15: Electroplating process over a sacrificial layer: a) Pattern sacrificial photoresist using standard lithography. b) Deposit shorting layer. c) Perform masking lithography and electroplating. d) Remove photoresist and etch shorting layer [19].

common difficulty during the removal of the sacrificial layer is stiction, where surface tension from the liquid solvent or etchant can produce large attractive forces between nearby surfaces and cause them to pull together. This can be avoided through the use of super-critical drying [19].

A common metal patterning technique that involves the use of a sacrificial layer is called metal liftoff. Generally, two photoresist layers are deposited onto the substrate: a lower lift-off resist (LOR) and an upper imaging resist [39], although in some cases only the imaging resist is required [19]. The LOR has a higher etch rate than the imaging resist, leading to an undercut photoresist ledge. When a metal is deposited onto the device, the undercut prevents it from forming a continuous sheet across the side walls. Thus, only the metal deposited directly on the substrate is attached, and removal of the photoresist layers with an organic solvent will similarly remove the remainder of the metal. This process is described visually in Figure 2.16.

2.3.3 Microtemplating. Microtemplating offers another category of making devices in the micron range. This involves the transfer of features from a master to copies. This allows the initial fabrication cost of the master to be spread out

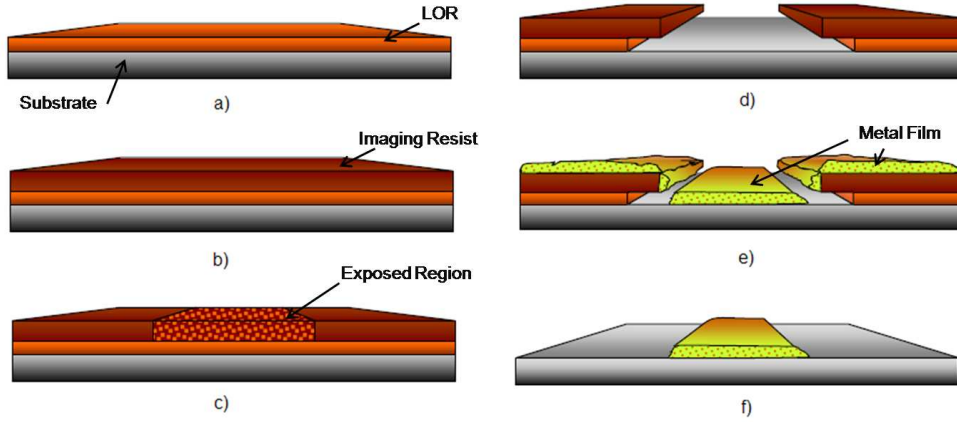


Figure 2.16: Metal lift-off process a) Coat and soft-bake LOR. b) Coat and soft-bake imaging resist. c) Expose imaging resist. d) Develop imaging resist and LOR. e) Deposit film. f) Lift-off resists and unwanted metal [39].

over multiple device fabrication runs while still obtaining good resolution. The most commonly used microtemplating techniques include casting and micromolding.

Casting is a method where a liquid material is enclosed in a mold and allowed to solidify. This can be extended to the microscale using materials such as poly(dimethylsiloxane) (PDMS) with a curing agent as the cast material. A variety of materials can be used for the master, such as silicon, oxide, or SU-8 photoresist [40]. Once the PDMS is pouring onto the master, it is enclosed using another planar surface. After curing, the PDMS can be peeled off the master. A process from Jo, *et al.* is shown in Figure 2.17.

Micromolding is very similar to casting, except the PDMS is not enclosed for curing. Some molding processes involve embossing at 50-100 °C. This allows molding of both surfaces and cure times within 10 minutes [40].

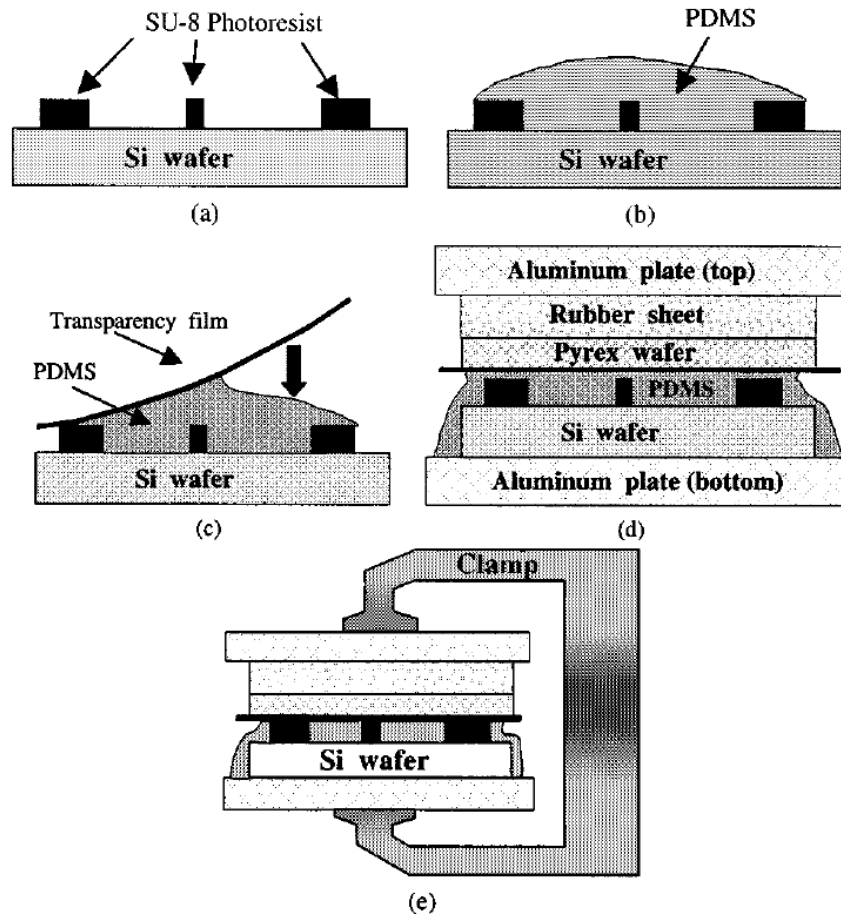


Figure 2.17: Example Casting Process a) Master is formed using standard SU-8 photolithography on silicon b) PDMS prepolymer poured c) Transparency placed over mixture d) Compression mold formed e) Layers clamped during cure, after which the transparency can be peeled off with intact PDMS structures [41].

2.4 *Fabrication of SAW*

Much of the complexity of a SAW sensor goes into the design work. Once the design process is complete, a comparatively simple fabrication process is the next step. We will explore piezoelectric substrate preparation, IDT deposition, and sensing film fabrication in this section.

2.4.1 Substrate Preparation. Once a piezoelectric material has been chosen, one must begin the fabrication process by obtaining the correct substrate. If this is quartz, lithium niobate, or any of several commercially grown bulk crystals, one may simply purchase a wafer precut and polished. One may request one side be left unpolished to reduce interference from bulk wave reflections off the back side of the substrate. However, if one chooses to deposit an epilayer, a process must be developed to correctly align the crystal molecules on the chosen substrate, generally using a form of chemical vapor deposition (CVD) [20].

2.4.2 IDT Fabrication. Once the piezoelectric substrate is ready, standard IC lithography techniques can be used to deposit and pattern the metal device geometry. The metal can be deposited by sputtering or evaporation. Patterning steps generally use UV lithography and metal lift-off for most devices, but could be extended to e-beam lithography if smaller feature sizes are necessary. Except for the bond pads, the SAW metal is generally of uniform thickness and only requires a single mask. Sometimes a 50 nm coating of silicon dioxide is applied as a protective coating over the IDTs [20].

2.4.3 Sensing Film Fabrication. Due to the wide array of sensing films, there is a correspondingly wide array of film fabrication techniques. Most polymer film depositions require a patterning step with photoresist to place the film selectively between the IDTs. This is especially important if there is a possibility that the film could short out the IDT's. After this point, there is a wide variety of deposition options. The polymer could be spun-coat on the surface, although this can result

in overly thick films with poor uniformity. Alternatively, polymer films could be deposited with CVD or plasma enhanced chemical vapor deposition (PECVD).

In addition to vapor sensitive polymer films, there is the possibility of coating the SAW device with biologically active films [23–25]. Antibodies, odorant binding proteins (OBP), and aptamers are three categories of organic molecules with the potential to be used in biosensors. Antibodies are complex proteins used by the immune system to identify and tag foreign targets inside the body, such as bacteria and viruses. Antibodies specific to a certain target molecule can be obtained by injecting a mammal with the target, then capturing the new antibodies produced by the animal to target it. They are currently the most well understood and used sensing molecule. Odorant binding proteins are naturally produced proteins used to bind to molecules in the air. They are mostly found in the nasal passages or antennae of an animal. OBPs are perhaps the least understood of the three possible sensing molecules, but since they are the molecules used in nature to sense airborne targets, they are the subject of much research interest. Finally, aptamers are short chains of synthetic amino acids that are selected from a large number of random sequences based on their ability to bind to a specific target molecule [42]. The aptamers that display high affinity to the target also tend to be selective against other molecules, leading to engineered selective binding [43]. Any of these molecules have the potential to be used in future biosensors.

There are a variety of techniques available to pattern biomolecules, such as dip-pen lithography, e-beam lithography, inkjet printing, and preferential binding [44]. Another possibility is the use of a self-assembled monolayer of patterned linker molecules which can tether the biomolecules chemically to the surface without suppressing their sensing ability. To do this, a monomer solution is applied to the substrate. Each monomer atomically bonds at one end to the substrate (often silicon or gold), resulting in a single molecular layer film. The other end of the monomer is designed to be a succinimide molecular group, which can permanently bind to an amine group in the structural region of the sensing molecule [45]. The result of this

binding is a ‘forest’ of sensing molecules bound on the surface of the device, each of which retains its specific binding capabilities. Since biological molecules require an aqueous environment in order to function properly, one possibility is to coat the wafer with a thin hydrogel either before or after biomolecule deposition [23–25].

2.5 Characterization Techniques for SAW Sensors

Once a SAW sensor has been designed and fabricated, there is a need to test and characterize the sensor. There are two primary methods with which to do this, involving different figures of merit. These methods are transmission parameter analysis (TPA) and integrated oscillator analysis (IOA).

2.5.1 Transmission Parameter Analysis. Transmission parameter analysis is the quicker of the two methods but requires more expensive equipment. In TPA, a precision input frequency is applied to the input IDT while either or both the amplitude and phase are measured at the output IDT. In this mode, changes to the sensing layer are captured through changes in the amount of insertion loss or the phase. These can be quantified with units of dB/ppm or degrees/ppm concentration of the vapor to be sensed. Sometimes the input frequency is swept across a range to allow a more complete picture, although this is less adaptable to field automation. The minimum equipment necessary is a precision signal generator and spectrum analyzer or a network analyzer. Matching the load presented by the SAW device is recommended [18]. Due to the expensive precision equipment setup, it is possible to obtain good results using this method. However, the equipment is neither portable nor cost-effective enough for widespread application outside of the laboratory.

2.5.2 Integrated Oscillator Analysis. Integrated oscillator analysis requires extra design time, but allows more application outside of the laboratories due to its producibility and portability. In this method, the SAW sensor is configured as the frequency selective feedback element of an RF oscillator, as shown in Figure 2.18a.

Random noise in the system is amplified by the loop until stable oscillation occurs. The SAW device determines the exact frequency at which the system will resonate according to the Barkhausen criteria as follows. The closed loop gain must be greater than one for oscillations to build, and the phase delay around the loop must be a multiple of 2π . Velocity changes due to vapor sensing result in a linear phase shift in $H(f)$. If one assumes that the phase of the external loop is comparatively constant, then a new frequency of operation now provides the correct loop phase delay for oscillation, and the frequency of the entire system shifts to a slightly new value. This frequency can be sensed easily with a frequency counter. By adding a reference SAW oscillator and mixing the two frequencies, one now only must measure the difference of the two frequencies. By doing this, not only can this method increase producibility by allowing measurement at a much easier low frequency, but it also automatically subtracts out systematic noise such as temperature or humidity effects.

2.6 Chapter Summary

In summary, the use of surface acoustic wave devices as sensors is a fairly recent field. While the generation and reception of acoustic waves using IDTs is fairly well understood, the optimization of SAW devices for sensing is not. Important variables to creating good surface acoustic wave sensors include substrate materials, electrode composition, geometry, and the type of sensing film used. Different groups have suggestions for these variables based on experience, but hardly any concrete proof is available. MEMS fabrication techniques appear to be the most applicable to building this device, and several device characterization techniques are available.

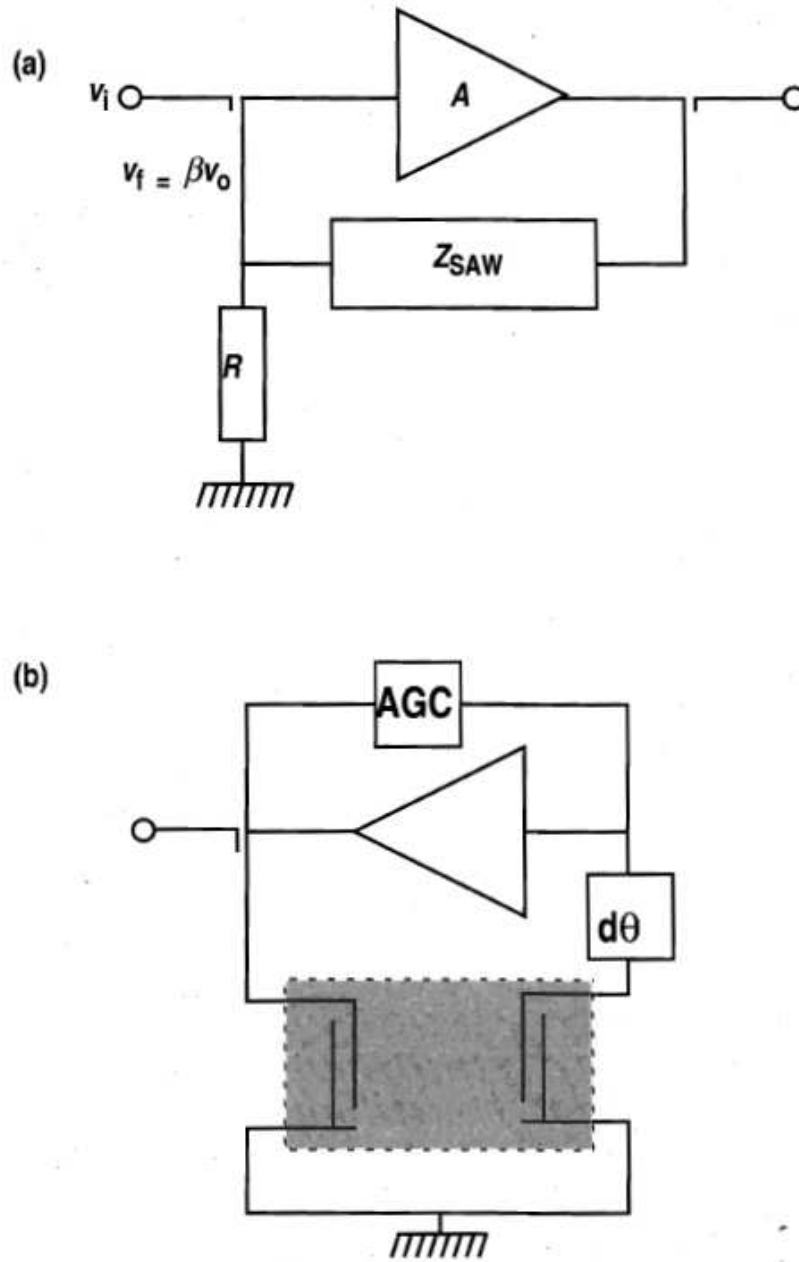


Figure 2.18: (a) The basic SAW Oscillator acts as the frequency selective portion in a feedback oscillator loop. (b) Improvements to the SAW oscillator include an adjustable phase block to position the SAW in the optimum location of its frequency response and an automatic gain control block to provide the proper signal levels to the input IDT [20].

III. Research Methodology

This chapter will explain the research procedures used in this thesis to investigate SAW devices as sensors. This includes a project overview, the design of the sensors, the processes used to create the sensors, the equipment setup used to test the sensors, and the details of the tests performed.

3.1 *Plan of Attack Overview*

The SAW device was created using standard photolithography processes. A quartz or lithium niobate wafer was diced into 1 cm² squares using a diamond-tip saw to provide the substrates for each sample. A soda-lime/chrome mask was fabricated commercially by Photosciences, Inc. This mask was used to pattern a double layer of lift-off resist and imaging resist on the samples using an ultraviolet mask aligner. The exposed resist was developed, opening features in the resist layer down to the substrate. Care needed to be taken to align the exposure with the correct crystallographic axis in order to take advantage of the maximum piezoelectric constants in the cut of the wafer selected. This allowed subsequent metal deposition directly onto the substrate using an e-beam evaporation system. Metal-liftoff was performed, removing the unwanted metal and photoresist and resulting in complete devices. These were either probed directly at the bond pads or wire-bonded to a chip carrier for increased durability.

After the SAW device was fabricated, the next step is to deposit a sensing layer. Several deposition methods were proposed to deposit the Nafion, including draw-down bar coating, inkjet deposition, and spin-coating. The objectives were to create a thin (approximately 1 micron) uniform coating. The draw-down bar and spin-coating were suitable for coating the entire device, while ink-jet printing confers the ability to place drops of material at specific locations on the device.

A photolithography mask including basic SAW device designs was available from the sponsor, AFRL/RXB. Initial device fabrication was performed using this mask, which allowed fabrication process refinements early on in the project and led

to early fabricated devices. The devices made using this mask were used to establish the testing equipment and procedures for generating and detecting surface acoustic waves. Once evidence of surface acoustic waves was found, this verified both our basic approach to surface acoustic wave generation and the test equipment used was satisfactory.

The original mask did not include several design norms from the literature review, including additional fingers, a larger acoustic aperture, and increased spacing between the electrodes. Without these improvements, it was uncertain whether or not the initial devices would produce measurable surface acoustic wave activity. Additionally, it was desired to test different SAW design parameters not available on the mask from AFRL. Finally, several additional devices were desired for purposes such as surface, open, load, through (SOLT) calibration and bond pad deposition. As a result, a second mask was designed concurrently with initial fabrication using the AFRL mask.

Once the second mask was received, fabrication began using the new devices. These devices were then tested for SAW activity using the network analyzer. Once this was confirmed, the devices were coated with a Nafion polymer layer, which is sensitive to ethanol vapors [46]. Dry nitrogen was alternated with with nitrogen saturated with ethanol vapors to investigate the sensing ability of the completed sensor. Both the amplitude and phase of the transmitted signal (S_{21}) were recorded in order to better understand the sensing mechanisms present.

3.2 SAW Device Design

3.2.1 Mask Design. Based on the lithographic limits of available equipment and the cost of mask fabrication, the finger width was set at two microns to maximize device sensitivity according to Equations 2.2 and 2.12. A variety of guidelines found in the literature review were used to scale the structure to this finger width, creating the design of the standard device shown in Table 3.1. A variety of similar devices

Table 3.1: Design Parameters of Basic SAW Device

Finger Width (μm)	2
Number of Finger Pairs	120
Acoustic Aperture (μm)	800
Center to Center Spacing (μm)	2000
Electrode Thickness (\AA)	1000
Substrate Material	ST Quartz

were included on the same mask to test the effects of various geometries on device sensitivity, especially finger width and IDT spacing. Additionally, devices including options such as resonators, arrays to reflect unwanted acoustic energy away from the devices, and different pad schemes were designed.

The ability to design SAW devices with an increased number of finger pairs (N) was one of the main incentives to design a new mask. Doing this comes with a number of benefits as detailed in Section 2.2.1. However, at some point, the benefits to increasing N begin to decrease and even hinder device operation due to increased attenuation and reflection due to impedance mismatches. A mathematical description to optimize this design parameter is not available, but most SAW devices found in literature contain from 50-160 finger pairs in each IDT [18,24,28]. Since the original mask had only 5 finger pairs, it was decided to raise N to 100. Ballantine suggests that this is the turning point beyond which further benefit is not obtained [18]. Later it was learned that another hinderance from having a larger N was an increased likelihood of contamination causing terminal faults during fabrication. Alternate designs using 75 finger pairs were also designed on the mask.

The acoustic aperture is the length of overlap of the IDT fingers. The only requirement found in the literature review was that this must be at least 30λ in order for the wavefronts to be considered parallel. Since none of the devices on the mask from AFRL satisfied this condition, it was unclear in advance whether they would even work properly. A wide range of acoustic apertures from 50 to 200λ are reported to work in literature [11,13,18,24,28]. A value of 100λ was chosen in order to

Table 3.2: Novel Layered SAW Electrodes

Material	Thickness (Å)
Titanium	100
Aluminum	750
Nickel	100
Gold	150

fall well within this range while avoiding the increasing IDT capacitance from making it too large. Several devices with a 50λ acoustic aperture were also designed.

The center to center spacing L between the input and output transducers affects the degree to which the phase changes given a change in acoustic velocity from a binding event (see Equation 2.13). For this reason, it is beneficial to increase L . However, this increases attenuation, since the wave must travel further. Ballantine suggests values in the range of $200 - 400\lambda$. Since the attenuation constant of the SAW devices coated with biomolecules was unknown, a value of 250λ near the bottom of this range was selected for the primary device, increasing the likelihood of obtaining devices with measurable signal throughput. Devices with spacings of 125 and 400λ were also designed on the same mask.

3.2.2 Material Choices. In order to obtain the benefits of both the low density aluminum and corrosion resistant gold for the deposition metal, a novel layered electrode scheme was designed. A titanium adhesion layer was required in order to obtain good surface attachment. An aluminum layer was used to provide low electrical resistance while minimizing acoustic reflections as compared to a denser material. A gold surface layer was used to provide a corrosion-resistant surface and good electrical contact. Finally, a nickel barrier layer was required between the gold and aluminum to prevent intermetallics from forming. This electrode scheme is given in Table 3.2. Additionally, the bond pads underwent an additional lithography step in which 5000-7500 Å of gold was added to increase the thickness to allow easier probing and wire bonding.

As stated earlier, increasing the natural frequency of the SAW device increases its sensitivity. According to Equation (2.12), another way to increase the natural frequency of the device is to increase the velocity of the acoustic wave. This is a variable based on the material and crystal orientation of the substrate as well as the propagation direction of the surface acoustic wave. Many of these velocities have been experimentally determined, the most commonly used being a lithium niobate cut at 128° from the Y-axis for propagation along the X-axis. This cut results in both high piezoelectric coupling and high acoustic velocity. As a result, 128° RY-X lithium niobate was ordered as a primary substrate, with Y-Z lithium niobate providing a comparison. After further research, it was found that quartz may result in higher surface sensitivity despite its lower acoustic velocity (see Section 2.2.2). To test this theory, ST-cut quartz was also ordered, since it has the best acoustic velocity and piezoelectric coefficient of the temperature-compensated quartz cuts.

3.3 Device Fabrication Using AFRL Mask

It was decided that due to the higher cost of the piezoelectric wafers, fabrication would be done on individual chips rather than the full wafers, minimizing the waste from poor runs. To obtain these chips from the full wafers, two different approaches were used. A diamond saw at AFRL/RY was used to dice the wafers into 1 cm squares. The initial wafer set diced including one of each lithium niobate cut. This set did not have a photoresist layer as a protective top coating, leading to cleanliness issues observed during later processing. Subsequent dicing sets included a layer of photoresist (1818) spun on to collect the debris caused by dicing.

On all substrates ordered, the proper propagation direction coincided with the flat of the wafer. Since orientation is critical to success, upon removal from the dicing pad each chip was marked on the back side with a diamond tipped pen in order to keep track of the proper orientation during subsequent processing steps.

The basic process began with cleaning the wafer. The photoresist is then applied evenly by spinning the samples at a constant speed. This is done in two layers using a lift-off resist (LOR3A) underneath an 1805 imaging resist. The samples are exposed using contact lithography on an EVG620 mask aligner. The exposed regions of the imaging resist are developed away, exposing the LOR underneath. This is removed isotropically during the same developing step, creating an undercut of the imaging resist. The device metal is then evaporated using a Torr-EB-4P-6KW e-beam evaporation system in a non-conformal process. Due to the undercut of the LOR, the metal deposited on the substrate is unconnected to the metal on the photoresist. This allows the unwanted metal to be lifted off in an ultrasonic bath when the photoresist is dissolved in acetone, leaving device metal as desired. These general processes were utilized and refined over a number of lithography runs.

Each run generally consisted of 6-10 chips with similar, but not identical, processing steps. These chips were each fabricated with at least four devices. A naming scheme was followed using the series number, sample number, and device number. Thus, the third device from the top on sample one of the second run is referred to as Device 2.1.3, but the chip itself is Sample 2.1.

Series 1 and 2 chips were used to refine the lithography process in order to produce the best devices. Variables tested included various photoresist layers, UV exposure times, development times, and the inclusion of a plasma ashing step. Plasma ashing is a process where a low-pressure oxygen plasma is used to remove photoresist from a wafer. It was attempted here in order to ensure all of the photoresist was removed in the developed areas while still leaving sufficient photoresist remaining where desired for metal lift-off. Series 3 fabrication was performed using these refined processes in order to produce working devices for testing. This process is given in Table 3.3, and further details from process refinement are available in Appendix A.

Table 3.3: Series 3 Lithography Process

Clean Chips Acetone spray for 20 seconds at 500 rpm Methanol rinse for 20 seconds at 500 rpm Nitrogen dry for 15 seconds at 500 rpm Bake on hotplate at 110 °C for 2 minutes
Photoresist Application (Spread/Spin) LOR3A at 500/3000 rpm for 5/30 seconds Bake on hotplate at 170 °C for 2 minutes 1805 at 500/3000 rpm for 5/30 seconds Bake on hotplate at 110 °C for 90 seconds
Exposure and Development Expose in EVG620 for 2 seconds Develop with LDD26W on spinner for 30 seconds (35 seconds for 3.3) Dry with nitrogen for 15 seconds
Premetallization Spin 1818 at 500 rpm on 3" wafer Arrange samples on wafer Bake at 110 °C for 3 minutes
Metal Deposition 100 ÅTi 750 ÅAl 250 ÅAu
Metal Liftoff Soak wafer in acetone for 5 minutes Remove chip from wafer Immerse chip in acetone filled dish (3.2 and 3.4 attempted alternate tape liftoff) Sonicate in phases until metal removal complete Immerse in 1165 at 110 °C for 10 min

3.4 Testing AFRL-Designed SAW Devices

An Agilent E5070B vector network analyzer (VNA) formed the basis of the test equipment. It is a two-port device equipped with N-type connectors. This device allowed the measurement of both the magnitude and phase of the transmission (S_{21}) parameters over a range of frequencies from 300 kHz to 3 GHz, which easily covers the range of operation of the manufactured SAW devices. Since the phase changes are critical to the follow-on development of an oscillating SAW sensor system, it was important to both choose a network analyzer capable of phase measurements and to

include these measurements in the characterization of the SAW sensor in addition to any changes in the magnitude of the frequency response.

There were two difficulties to be overcome to use the network analyzer with a typical 4-probe system necessary to activate the SAW devices. First, the network analyzer output signals using N-type RF connectors, while the probe station connected with BNC. Second, the signal and ground on each of the two ports of the network analyzer would need to be connected to a separate probe without losing signal integrity. To solve the first problem, several N-type to BNC adaptors were obtained. However, the problem of splitting two ports into four remained.

Several high-frequency probe tips were ordered from the Micromanipulator Company in order to obtain necessary high-frequency performance. At the same time a calibration substrate was ordered to allow systematic errors in the adaptors and cabling such as signal attenuation, reflection, and distortion to be mathematically accounted for, thus reducing error.

In order to improve the issue of routing a 2-port network analyzer to a 4-port probe system, two custom splitter boxes were built with assistance from AFRL/RX, as shown in Figure 3.1. These boxes split an N-type connector into two BNC connectors, one for the signal and one for ground. The shielding of both BNC cables is connected to the ground of the N-connector to maintain signal integrity at high frequencies. The boxes were tested by hooking them to the network analyzer and running BNC cables between them, generating a direct through line between the two ports.

The network analyzer was brought to AFRL/RX, where an MMR Variable Temperature Micro Probe Station was set up. Frequency response data for this station indicated good performance up to 1 GHz. This station was also completely sealed, allowing vapors to be passed through the chamber to a vacuum outlet on the other end during electrical testing. Several adaptors were required to convert from BNC to the triax inputs of this probe station, but this was judged to be an acceptable imperfection, since calibration could account for the minor losses associated with

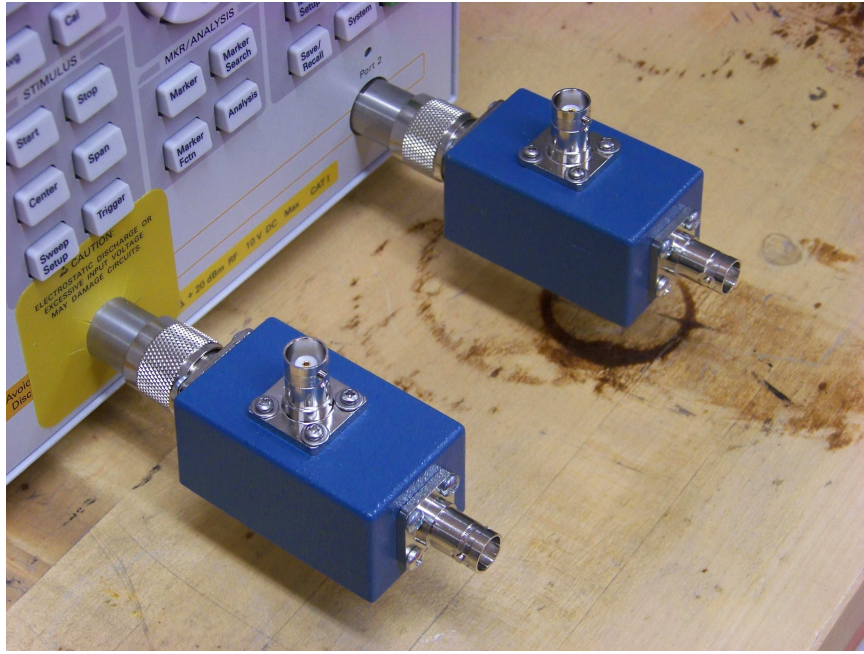


Figure 3.1: The custom made RF Splitter connects the ground and signal lines of an N-type connector to two BNC connectors using BNC cabling.

additional adaptors once the calibration substrates arrived. The system including the MMR probe station is shown in Figure 3.2.

Using the custom boxes, MMR probe station, and network analyzer, data was collected for several of the devices from the original AFRL mask. As detailed in Section 4.2, even minor table vibration would affect the probe connections and thus the frequency response. To gather sensor data that could reliably be attributed to changes in the gas flow and not probe connection movements, it became necessary to improve the quality of the electrical connections prior to the testing of sensing ability. Three solutions were proposed to do this. First, we could use the Picoprobe probe holders using high frequency probes in place of the MMR probe station. These probe holders had fine position control and the ability to be vacuum sealed to a surface such as the table, reducing vibration effects, but the probe spacing ordered was such that only devices on the new mask could use it. Second, the SAW device could be wire-bonded to a package that would be much more resilient to probing attempts. Finally, the thickness of the bond pads could be increased, which was only available

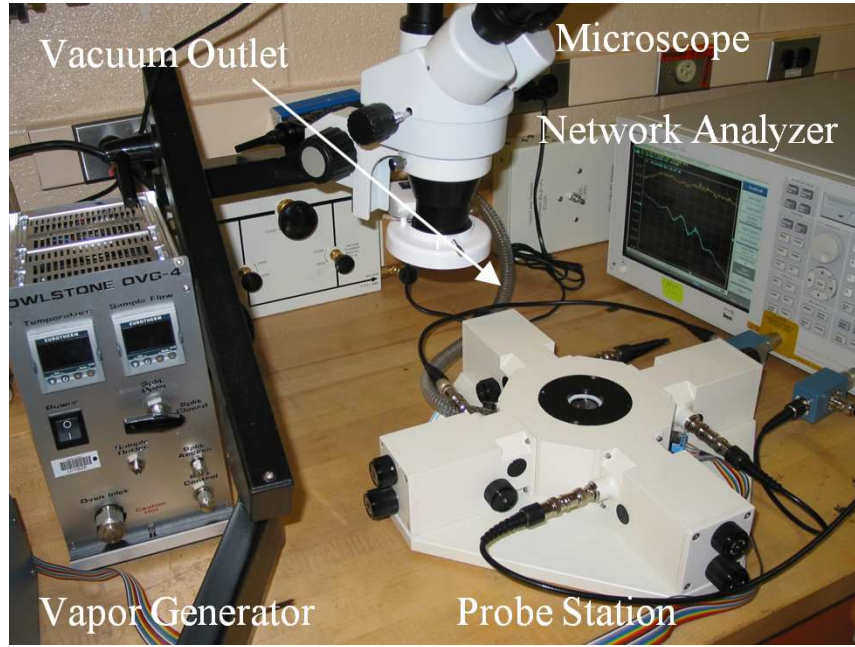


Figure 3.2: AFRL Testing Apparatus Including Owlstone OVG-4 Vapor Generator, Vacuum Outlet, Microscope, MMR Probe Station, and Agilent 5070 Network Analyzer.

on select designs from the newly designed mask. Since this mask had just arrived, further work proceeded with the second mask.

3.5 *Fabrication of AFIT-Designed SAW Devices*

Series 4-12 devices were fabricated using the newly designed mask at AFIT. Process refinements tested here included new cleaning steps, a second LOR layer to reduce bridging, the use of 1818 instead of 1805 to reduce bridging, and a quartz substrate to increase vapor sensitivity. Table 3.4 gives a brief overview of the purposes of the different series. Addition fabrication details for these series can be found in Appendix A.

3.6 *Wire Bonding*

With apparently good devices from both mask sets, the next step was to obtain reliable electrical contact to them. Wire bonding was chosen since this would allow

Table 3.4: Fabrication Series Overview

Series Number	Purpose	Notes
1	Process Refinement	Single LOR Layer
2	Process Refinement	
3	AFRL Device Fabrication	Good Devices
4	AFIT Device Fabrication	
5	AFIT Device Fabrication	Good Devices
6	AFIT Device Fabrication	2 LOR Layers; Good Devices
7	Process Refinement	Quartz Substrate
8	Process Refinement	Bond Pads Deposited First
9	Process Refinement	New Wafer
10	AFIT Device Fabrication	Good Devices
11	AFIT Device Fabrication	
12	AFIT Device Fabrication	

the probes to contact the robust packaging rather than the delicate device bond pads. The wire bonder at AFRL/RXB was selected. This bonder uses wedge bonds on both the first and second bond, with manual control of most of the process steps. Since the bonder did not have a process follower available, a wide variety of settings were used on bond pads as thick as approximately 8600 Å. Additional details on the tests run are available in Appendix A.

3.7 Testing of AFIT-designed Devices

With the arrival of the calibration substrate, the probe station and network analyzer were set up for calibration. The MMR probe station was set up to the network analyzer through the custom splitters, BNC lines, and BNC/Triax adapters as detailed earlier. Calibration measurements were taken with the network analyzer and calibration points fabricated at AFIT. Using both sets of calibration data separately, Device 6.4.1 was probed in the MMR station for SAW activity.

The high frequency probes ordered from the Micromanipulator company also arrived. These had dual probes for each probe holder to increase frequency performance. This also removed the requirement to split the cabling into 4 separate lines. One of the probe tips had a 50 ohm resistor in parallel in order to properly match

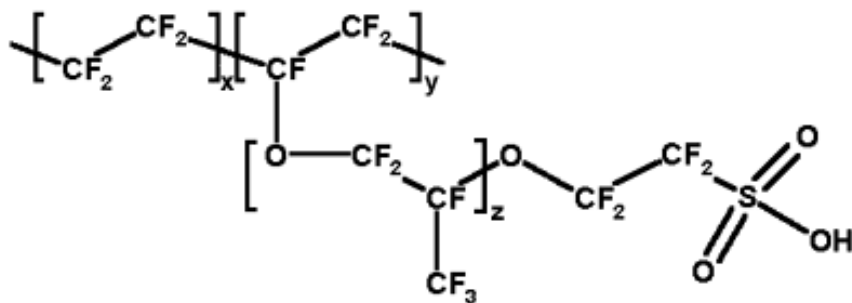


Figure 3.3: Chemical structure of Nafion [48].

the impedance of the transmission lines on the input. The other was designed with a 950 ohm resistor in series in order to keep the SAW output voltage from being overly loaded down by the measurement system. These probes were hooked to the network analyzer through an SMA/BNC adaptor, a BNC cable, and a BNC/N-type adaptor. A vacuum system was used to secure the probe holders to the table surface. Device 6.3.3 was measured using this setup.

3.8 Sensing Layer Fabrication

Several different sensing layers were selected to test. First, a sulfonated tetrafluoroethylene copolymer (Nafion) layer sensitive to ethanol vapors is used to establish the mass sensing ability of the SAW device apart from biological molecules. The chemical structure for Nafion is shown in Figure 3.3 [48]. Second, antibodies were purchased commercially through Sigma-Aldrich that were well-established to bind to TNT molecules. This would investigate the viability of biological molecules in a SAW sensing scheme. Finally, aptamers discovered by members of AFRL/RX to bind to TNT were selected. This would demonstrate the ability of the SAW sensor as a vehicle to verify new molecular interactions, as well as investigating a new sensor type never before created. Due to limited time, only the Nafion coating was tested.

The optimal placement of the sensing layer was also an unknown at the beginning of the project, therefore the sensors were designed using several methods, as allowed by the deposition methods. First, the sensing layer could be placed only in

the propagation path between the two IDTs, thus altering the phase and amplitude of the frequency response upon wave velocity change. Second, the sensing layer can be deposited directly on the IDTs. By slowing the wave down at the input and output, any velocity changes directly affect the peak frequency of the device. Finally, a coating over the entire device is feasible, combining both effects.

The antibody deposition methods were somewhat different, requiring more consideration of surface chemistry. One method planned was protein adsorption, where the SAW devices are submersed in a pH-neutral solution containing the antibodies and allowed to incubate at 40 °C to allow the antibodies to adsorb to the quartz substrate by Van der Waals forces. Using this method deposits antibodies indiscriminately and does not secure the antibodies against being washed off easily, but it does allow for preliminary sensor testing. Unfortunately, due to limited time this method was not enacted.

The thickness of two Nafion coating methods were tested using glass slides. These coatings used 5% by weight solutions of Nafion in a water/alcohol mixture. First, a draw down bar set at 250 μm above the surface of the sample was used to coat a slide. Second, a spinner set at 4000 rpm for 30 seconds was used to coat a glass slide. Both slides were allowed to dry overnight in order to dry the polymer. After drying, the thickness of the Nafion thin films were tested using a profilometer.

After cleaning with acetone and methanol and drying with nitrogen, several chips were coated on the spinner with Nafion using a variety of spin speeds. Sample 3.5 was coated with the Nafion solution on the spinner at 6000 rpm for 30 seconds and dried overnight. This sample contained a variety of working devices.

3.9 Testing of Coated SAW Devices

In order to establish the ability to create a good electrical contact to the bond pads after Nafion deposition, one of the samples that had Nafion spun at 4000 rpm

was placed into the MMR probe station. The two signal probes were placed in contact with the same bond pad on this device, and S-parameters were measured.

Sample 3.5 was placed in the chamber in order to test the sensing ability of devices coated with Nafion. Pressurized nitrogen from a tank was passed through an MMR cleaning unit to ensure high purity gas flow. After connecting the nitrogen through a flow meter into the MMR probe station, a vacuum unit was turned on, and the valve between it and the probe station partially opened. Both flow rate and pressure were measured. The flow meter was removed from the system, but all other valves remained constant for the remainder of the experiment. The electrical connection for these tests went from the network analyzer through the custom splitters, BNC cables, and necessary adaptors to the two input probes ports, with an identical setup for the output probes. In order to provide ethanol vapors, a specially designed glass beaker was used. Nitrogen could flow in one port, then had to bubble through 200 proof ethanol before reaching the output port, as shown in Figure. This setup saturates the nitrogen stream with ethanol [49].

Since they were expected to be the main indicators of sensory information based on the literature review, S_{21} amplitude and phase data was gathered for a variety of testing conditions on several devices. S_{11} amplitude and group delay data was also gathered concurrently. All data collected were averaged for 32 cycles (about 3.2 seconds) before being recorded in order to reduce the effect of random noise sources on the results. Additionally, calibration data was used in order to minimize systematic noise from probe radiation, signal leakage, and impedance mismatches.

First, data was collected while the probes were lifted above the devices in order to provide a baseline against which to demonstrate SAW activity. This data was taken approximately 15 minutes after nitrogen began being introduced to the chamber. Second, the probes were lowered to the bond pads of a 10 micron line width device and additional data was taken. Third, the ethanol bubbler was introduced into the vapor stream. After waiting 15 minutes in order to allow the ethanol to completely

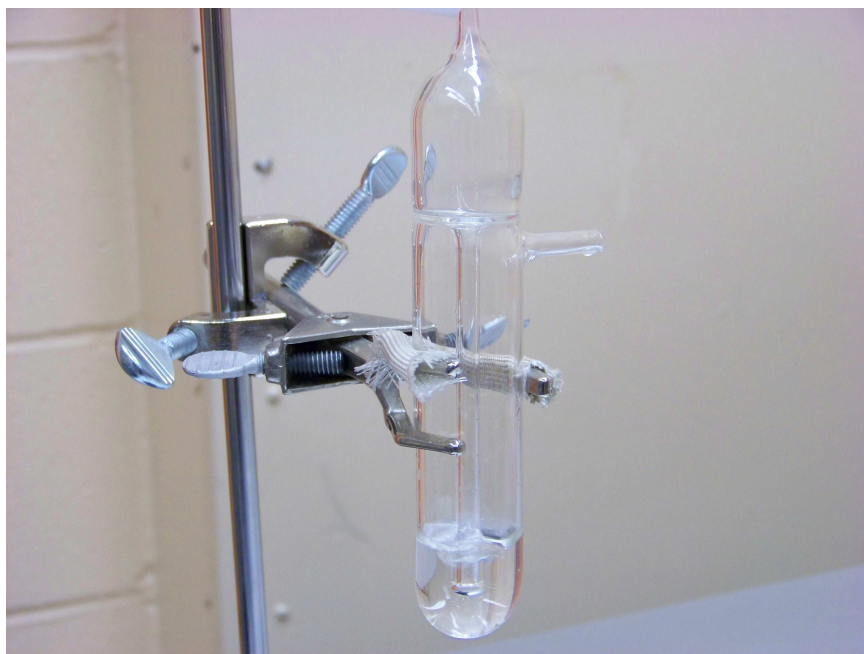


Figure 3.4: Glassware beaker for introduction of ethanol vapors into the nitrogen stream. Nitrogen is introduced at the top, then must bubble through ethanol to reach the output port on the side. Note that the beaker contains more ethanol during actual operation.

fill the vapor chamber and the Nafion coating to reach equilibrium, another set of data was taken. Finally, the bubbler was taken out of the flow and clean nitrogen was used to flush the chamber for an additional 15 minutes. After this, another set of data was taken to show sensing layer recovery.

This sequence of data collection was repeated for 6 micron and 3 micron line width devices. However, since all devices were on the same chip, the subsequent devices had already undergone previous nitrogen/ethanol/nitrogen cycles before being tested.

3.10 Chapter Summary

In summary, SAW sensors devices were designed, fabricated, and tested for sensing activity. Initial fabrication and testing was performed using a mask available from AFRL. Significant changes were designed into a new mask, from which new

devices were fabricated. Wire bonding was attempted to the devices in order to obtain good electrical contacts. Electrical characterization was performed with a network analyzer and high-frequency probe station and cabling. Several methods of coating the devices were attempted using Nafion, and these finished devices were tested for vapor sensing ability of ethanol vapors.

IV. Results

4.1 Results of Device Fabrication using AFRL Mask

Process establishment and refinement was performed using Series 1 and 2 chips. Of the variety of exposure and development times used, the combination of a 2 second exposure with 30 second development appeared the sharpest. This is shown in Figure 4.1.

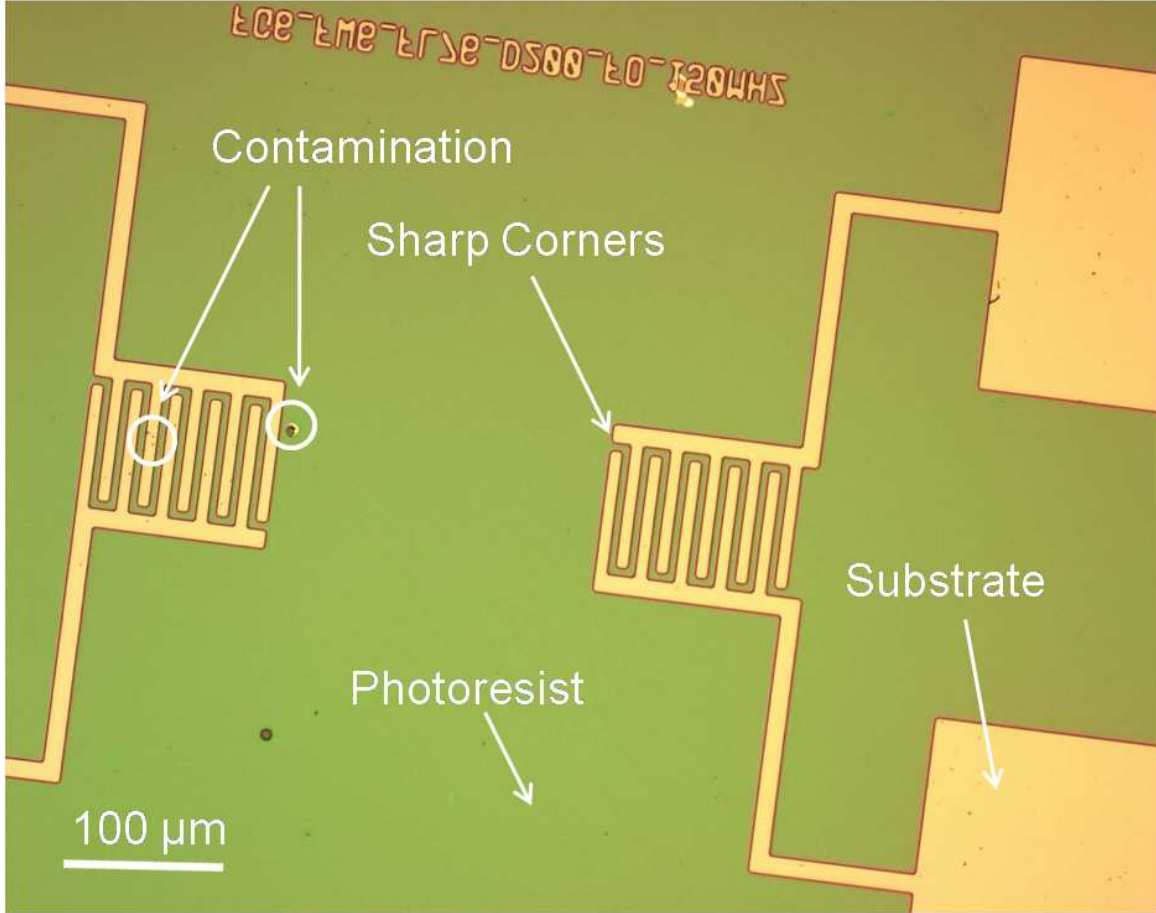
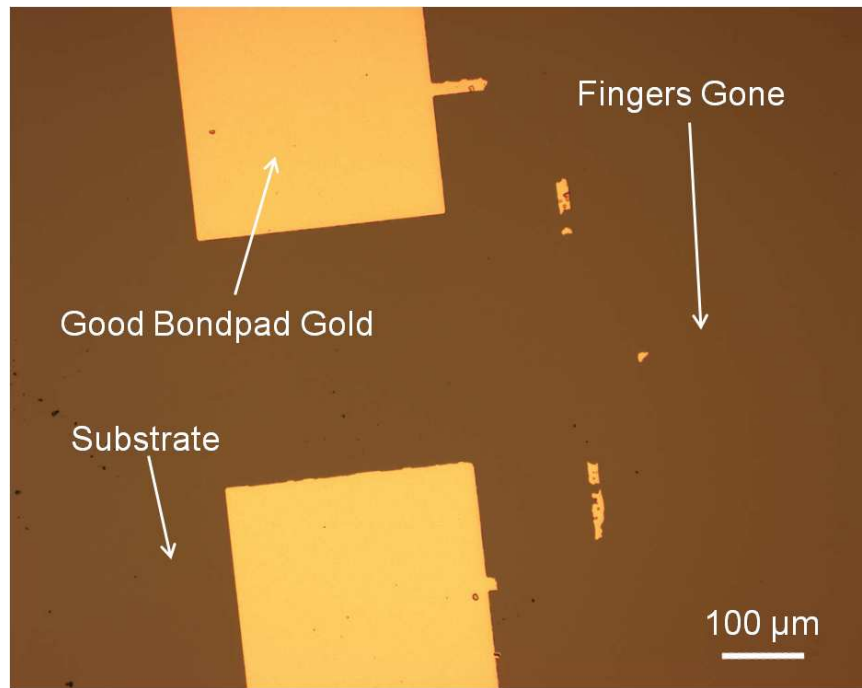


Figure 4.1: Series 1B Lithography showed that a 2 second exposure with a 30 second develop produced sharp patterns.

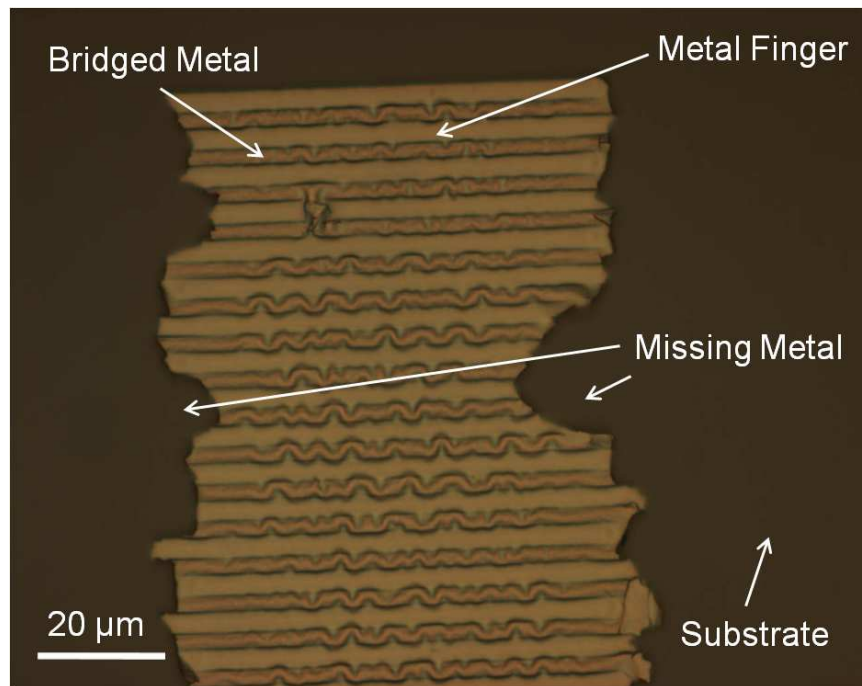
During the metal-lift-off procedure, it was noticed that some of the metal between the fingers of devices was not removed even after 20 minutes in the sonicator. This is referred to as bridging, since metal bridges the gap between fingers. The bridging could indicate that the LOR3A layer was not thick enough to support metal

liftoff. Using a profilometer on a test chip, it was found that the LOR3A layer was approximately 0.3-0.4 μm thick, which is well over the 125 percent of the metal deposition thickness (0.1 μm) recommended by Microchem [39]. Other areas of the samples lost significant portions of metal during sonication, which will be referred to as voiding. Examples of these defects are shown in Figure 4.2.

The chips that had been plasma ashed turned out to have the worst devices after sonication. This was likely a result of the photoresist being thinned from 0.75 to ~ 0.65 microns according to the profilometer. The second most important variable seemed to be the exposure and development time, where the 2 second develop and 30 second exposure produced the best devices. Finally, of the devices that had not gone through the asher, the ones with the titanium layer produced slightly better devices due to better adhesion to the substrate. Several of the devices made are shown in Figure 4.3. The procedure that produced the best devices was replicated in Series 3, producing a number of devices ready for testing. An image of these devices using a scanning electron microscope(SEM) is shown in Figure 4.4.

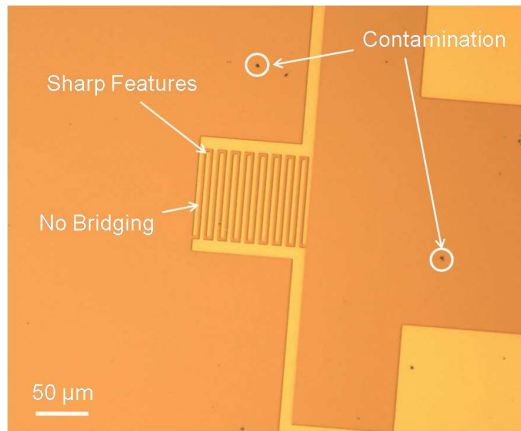


(a)

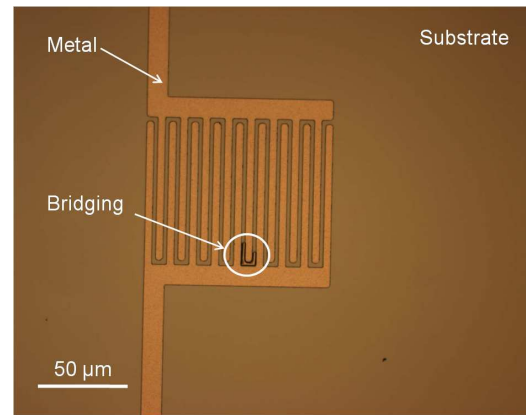


(b)

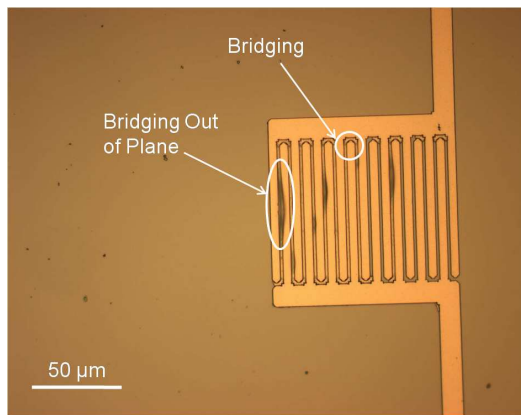
Figure 4.2: Series 1B Metal Lift-off (a) Sample 1B.1 is missing portions of metal. (b) Sample 1B.4 has its fingers bridged.



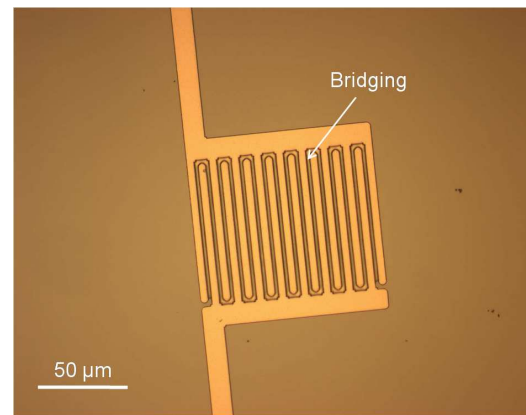
(a)



(b)



(c)



(d)

Figure 4.3: Series 2 Devices (a) 2 s exposure, 30 s develop, titanium (b) 2 s exposure, 30 s develop (c) 2 s exposure, 30 s develop, plasma ash, titanium (d) 1.5 s exposure, 45 s develop, titanium.

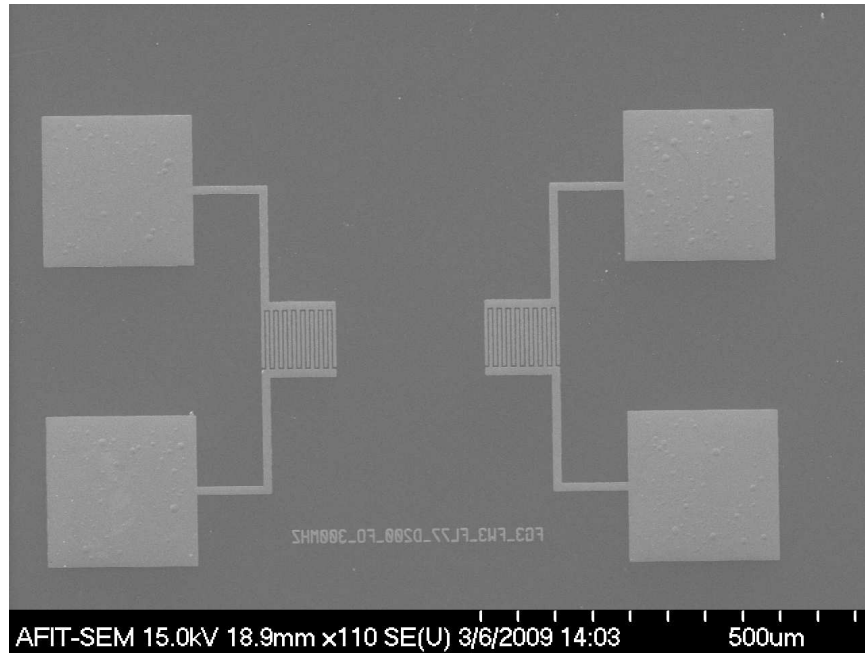


Figure 4.4: SEM image of one of the devices from Series 3.

4.2 Testing AFRL-Designed SAW Devices

Through measurement testing was conducted with the network analyzer and the custom built signal splitters connected by BNC cables. The results of this test are shown in Figure 4.5. The low S_{11} values and S_{21} near 0 dB demonstrate that the splitter and the cabling contribute low amounts of error into the data, since these characteristics are expected from a perfect short.

A device on sample 3.6 with 6 micron critical dimensions was tested using the MMR probe station, adaptors, BNC cabling, and the custom splitters. The results of this test are shown in Figure 4.6. These show the frequency response when the probes are both open and when the probes are connected to the SAW device. The highest point in the peak measured was at 145.25 MHz, although the center of the peak seemed to be closer to 146.25 MHz. Since peak frequency calculations using Equation 2.2 return values of 145.33 MHz, these results strongly confirm both surface acoustic wave generation and detection. Additionally, side lobes are seen as expected.

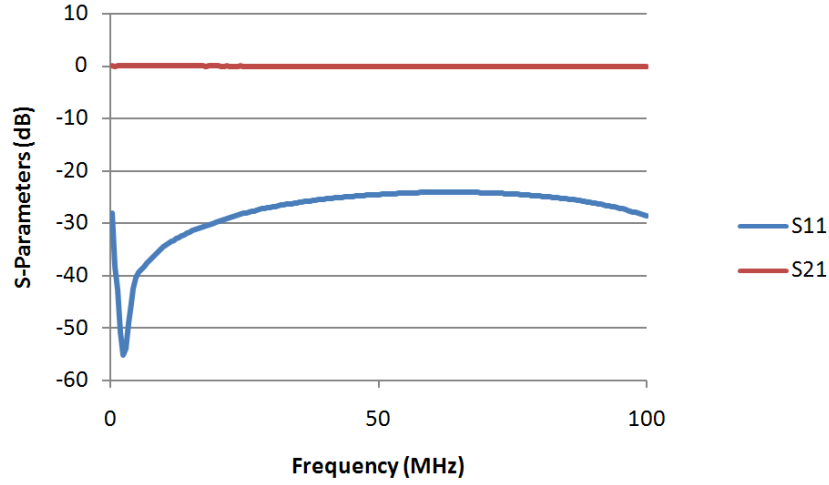


Figure 4.5: S-Parameters from shorting the network analyzer through custom signal splitters and BNC cables.

The general slope to the frequency response is due to imperfections in the cabling and probe station. It was observed that the measured frequency response changed significantly when the table was bumped even slightly. This was attributed to poor connections from the probes to the bond pads caused by pad damage.

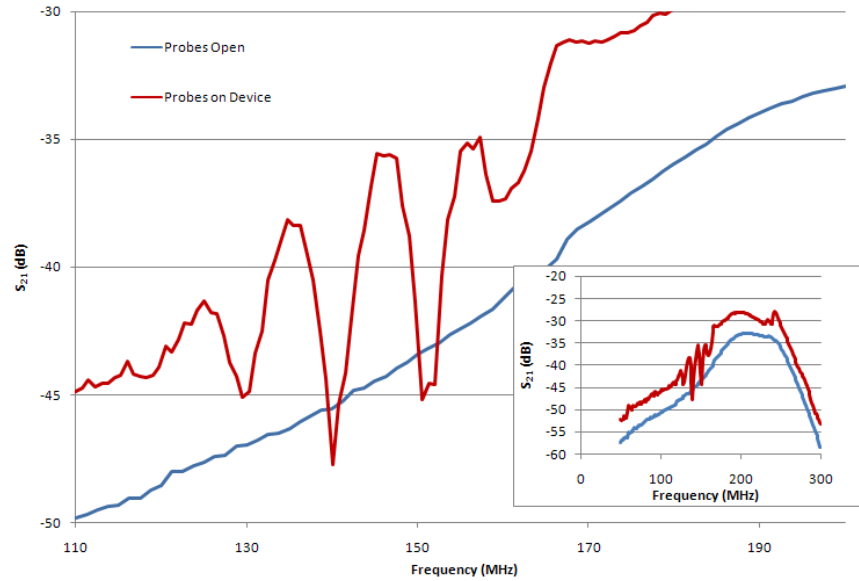


Figure 4.6: Frequency spectrums measured when probes are open and when connected to a 6 micron SAW device of 3.6. The inset shows the broader spectrum

4.3 Device Fabrication using AFIT Mask

When fabricating devices using the new mask, issues such as contamination became important considerations. Since the IDTs were much larger, the chance of a contaminant landing on the IDT was much larger, increasing the likelihood of device failure. An example of this is shown in Figure 4.7. Both additional cleaning steps using acetone-soaked cotton swabs and an 1818 protection layer during wafer dicing were implemented to increase device yield. These steps significantly reduced contamination issues.

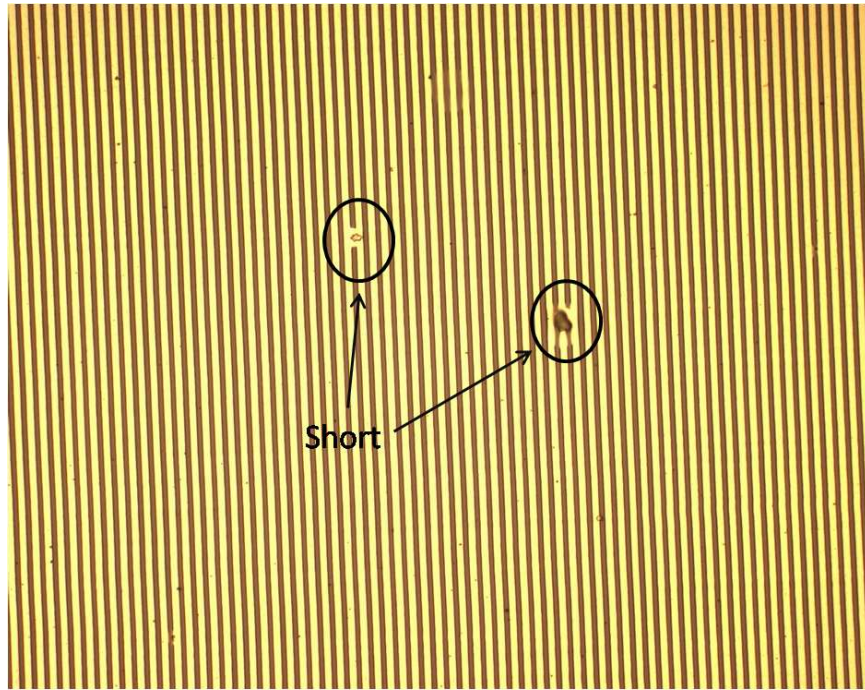


Figure 4.7: Sample 4.4 after metal lift-off and 1165 strip. Contamination caused several fingers to short together on half of the IDTs, while the other half fabricated successfully.

Wafers 6.1-6.4 were fabricated using a double LOR3A layer and an 1818 layer. It was found that an exposure time of 3.3 seconds with a development in LDD-26W of 70 seconds produced a number of good devices. Examples of these devices are shown in Figure ???. The SEM image in Figure 4.8 shows metal side walls still remaining on the edges of some fingers.

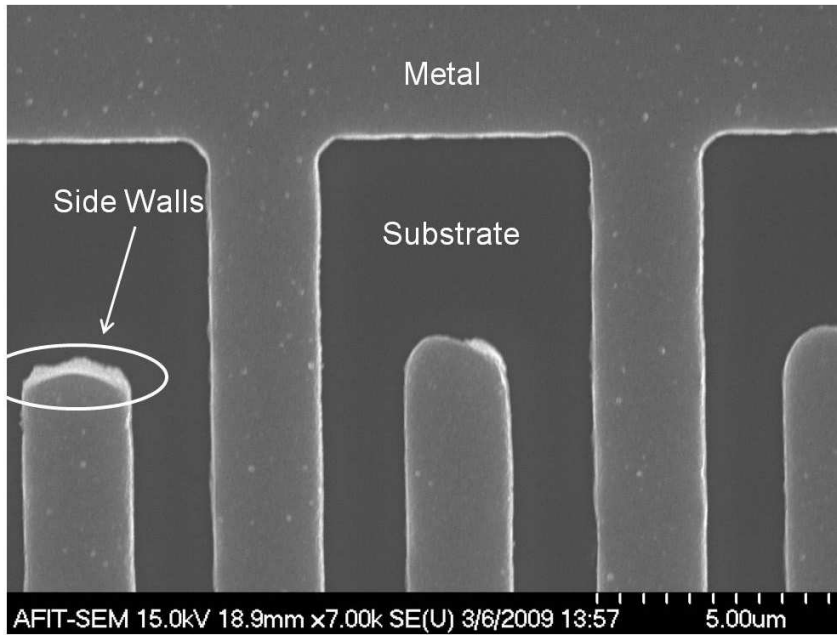


Figure 4.8: This SEM image of a Series 6 device appears to show vertical side walls remaining on some of the fingers.

Several of the devices that were fabricated using titanium/aluminum/gold fingers displayed interesting results. When current was passed through the fingers of a device that had been shorted, some fingers changed color from a yellowish gold to red immediately, as shown in Figure 4.9. This color shift was also observed after several weeks across the entire IDT for all devices with the same layering scheme even if no current had been run through them.

4.3.1 Wire Bonding. After several days of learning the equipment and process refinement, it was found that the bonding process was very forgiving when bonding to the gold-plated chip carrier. Conversely, no settings were found that created a successful bond to the SAW device bond pads. Both experimental results and online research suggest that the metal layer was too thin to create reliable bonding. Rather, it should be a minimum of 1.3 microns to create a good bond [51]. Another possible solution to poor bonding could be increasing the adhesion between the different metal layers.

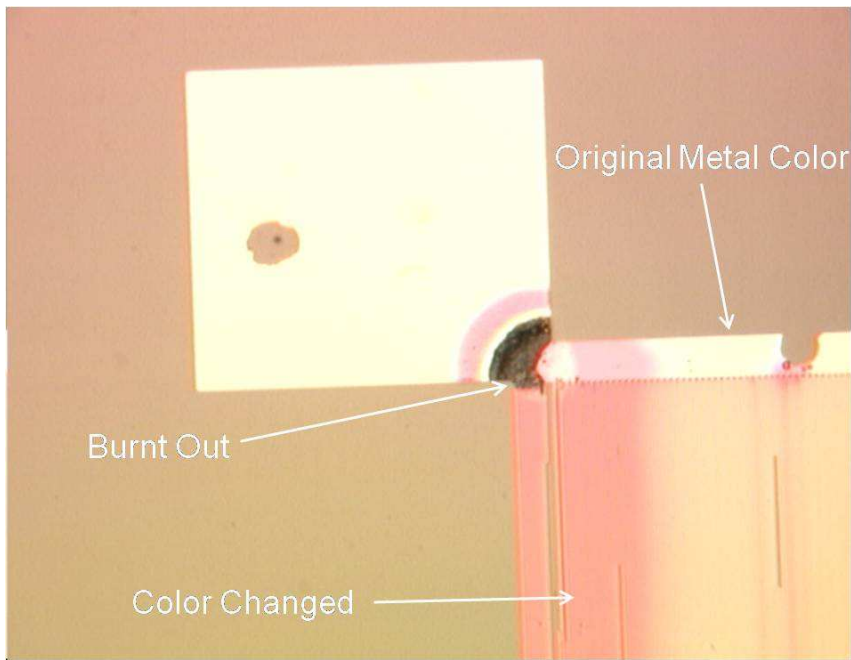


Figure 4.9: This SEM image of a Series 6 device appears to show vertical side walls remaining on some of the fingers.

4.4 *Testing AFIT-Designed Devices*

Data was taken using Micromanipulator probes on Device 6.3.3 revealing a peak at 433.2 MHz, as shown in Figure 4.10. Calculations predicted the peak at 436 MHz. One possible explanation for this is a slight misalignment of the device from the ideal crystallographic propagation axis during fabrication. A linear phase slope was observed near the resonance frequency, as expected.

4.5 *Testing of Coated SAW Sensors*

4.5.1 Electrical Characterization. The test to determine how the Nafion coating affected the ability of the probes to electrically contact the bond pads was successful. As shown in Figure 4.11, the DC S_{21} parameters increased from -78 dB to -0.04 dB. Since Nafion does not conduct electrons well, this high level of conductance indicates that the probes are piercing the Nafion layer and directly contacting the bond pads.

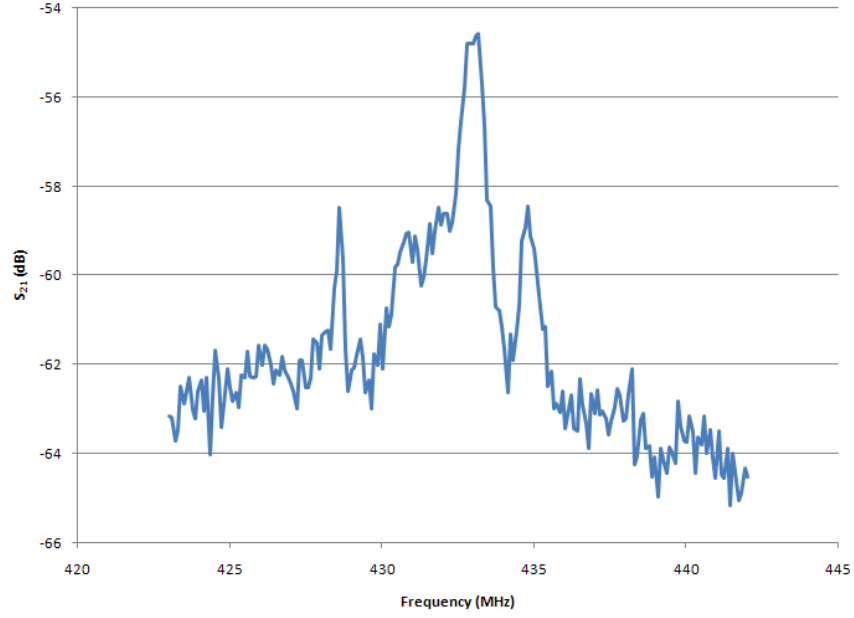


Figure 4.10: Testing of Device 6.3.3 using Micromanipulator probes

Table 4.1: Nafion Coated Resonance

Line Width (μm)	Calculated (MHz)	Measured (MHz)	Difference
3	291	313	7.56%
6	145	154	6.21%
10	87.2	93.2	6.88%

All three Nafion-coated devices tested displayed the characteristic sinc function shape of a SAW frequency response when tested for transmission. In each case the center of the sinc function indicated a resonant frequency 6-8% higher than expected from calculations, as shown in Table 4.1. Additionally, all of the devices displayed time-independent waves in the frequency response, which, although of significantly smaller amplitude than the SAW peaks, were not predicted by the analysis in the literature review. On the other hand, drastically different results were obtained from the different devices when tested for ethanol sensitivity.

4.5.2 Vapor Sensing. The 10 micron finger width device showed little difference in the S_{21} amplitude and phase when ethanol was introduced into the system. When the nitrogen was returned to the system, the amplitude peak dropped by 0.34

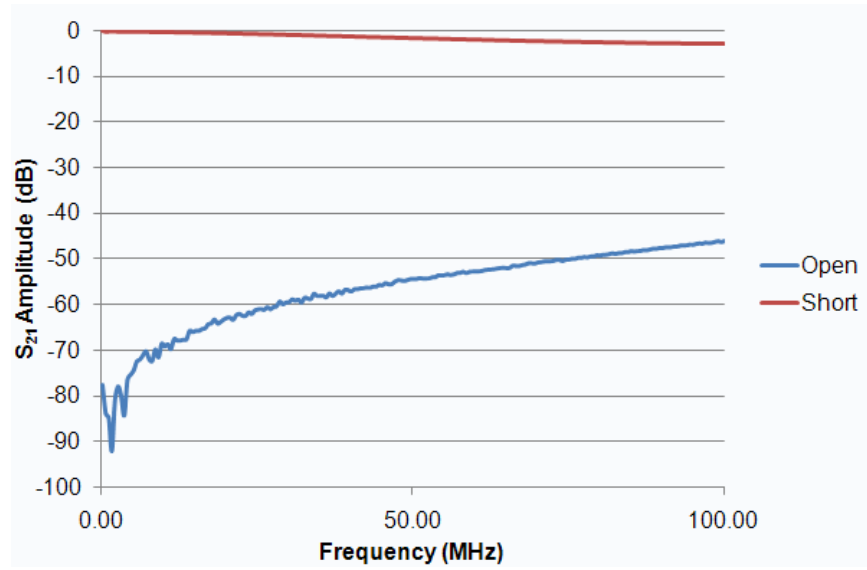
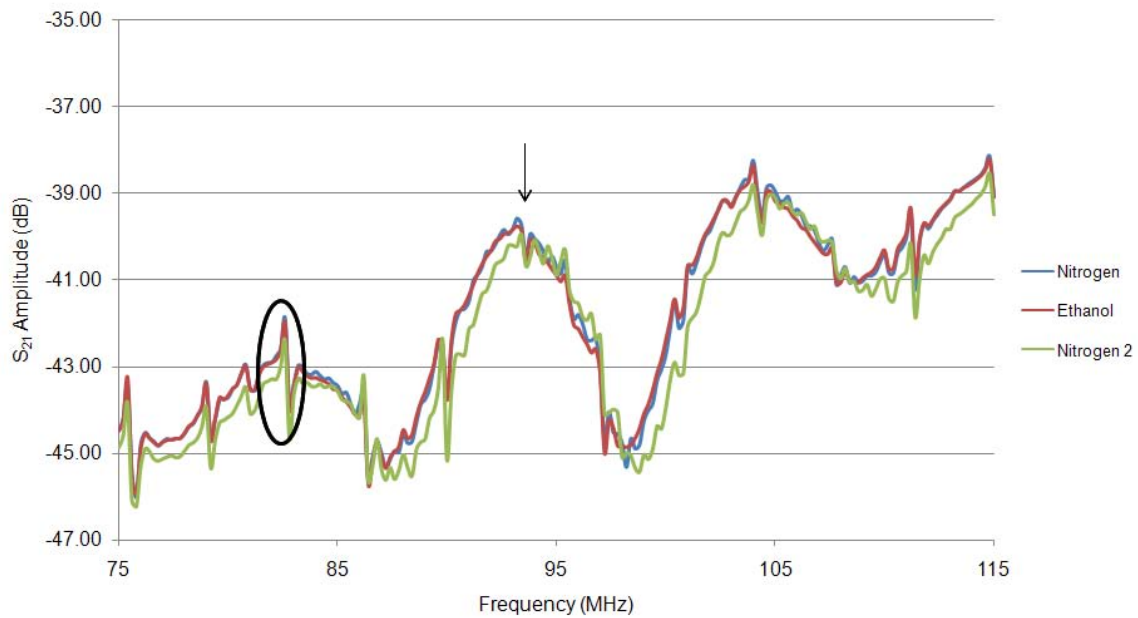


Figure 4.11: S_{21} amplitude measured with probes open and shorted across a bond pad coated with Nafion.

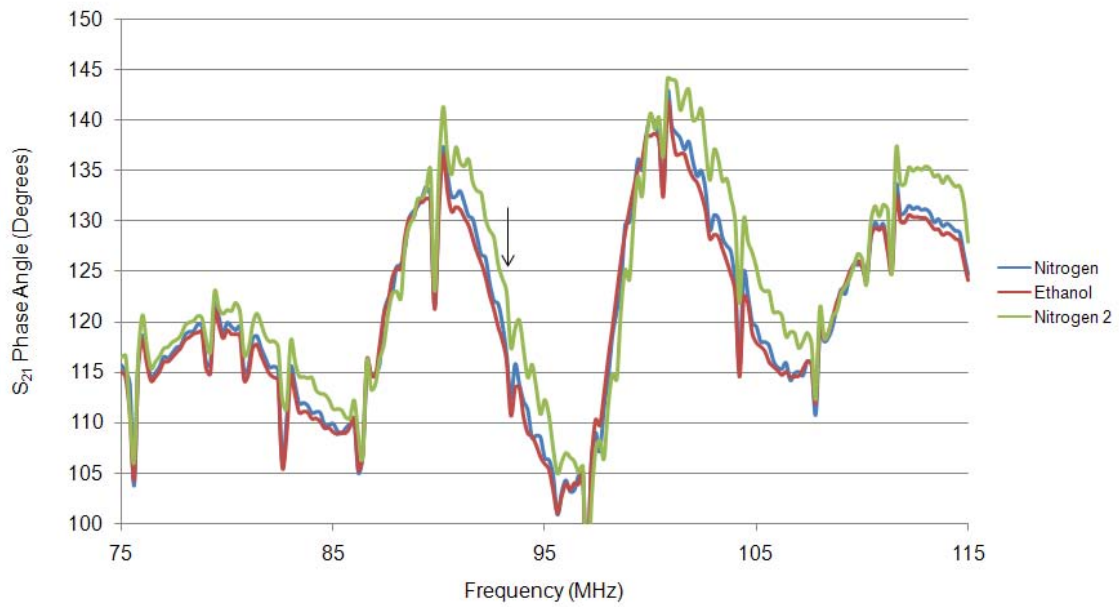
dB and the center of the main lobe was shifted up in frequency approximately 1 MHz. Similarly, the phase shift at resonance displayed an upward shift of approximately 1 MHz. This data is shown in Figure 4.12.

The 6 micron device showed only a negligible amplitude loss of 0.1 dB at the 154 MHz resonant peak upon the introduction of ethanol, with no frequency shift. Neither was a phase difference observed at resonance, although some minor differences are observed off resonance. The entire frequency response returned closely to the original levels upon return of the nitrogen. This data is shown in Figure 4.13.

The 3 micron device displayed the most convincing evidence of ethanol vapor sensing. The resonance peak at 313 MHz was both reduced in amplitude and shifted up in frequency when ethanol was introduced to the system. The exact shift amounts are obscured by a peak frequency unrelated to SAW activity, as shown by its presence in the frequency response of open probes. Additionally, both the slope and frequency of the linear phase at resonance were changed significantly. Upon return of the clean nitrogen, both the amplitude and phase of the frequency response returned closely to the original levels. This data is shown in Figure 4.14. The frequency span of the

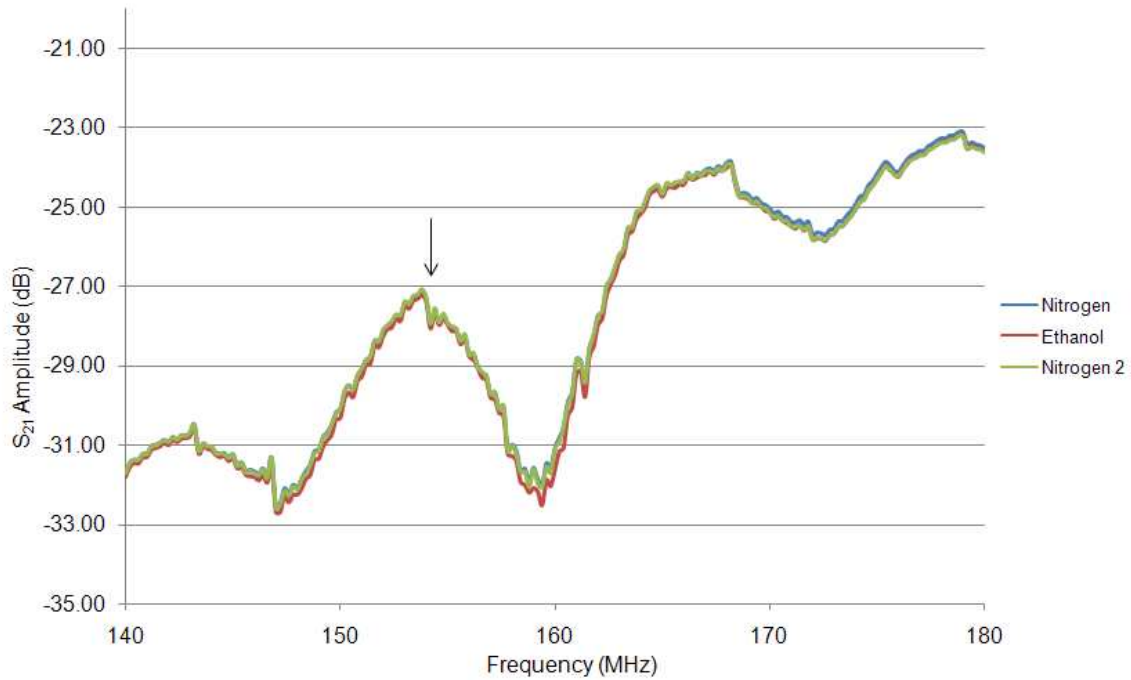


(a)

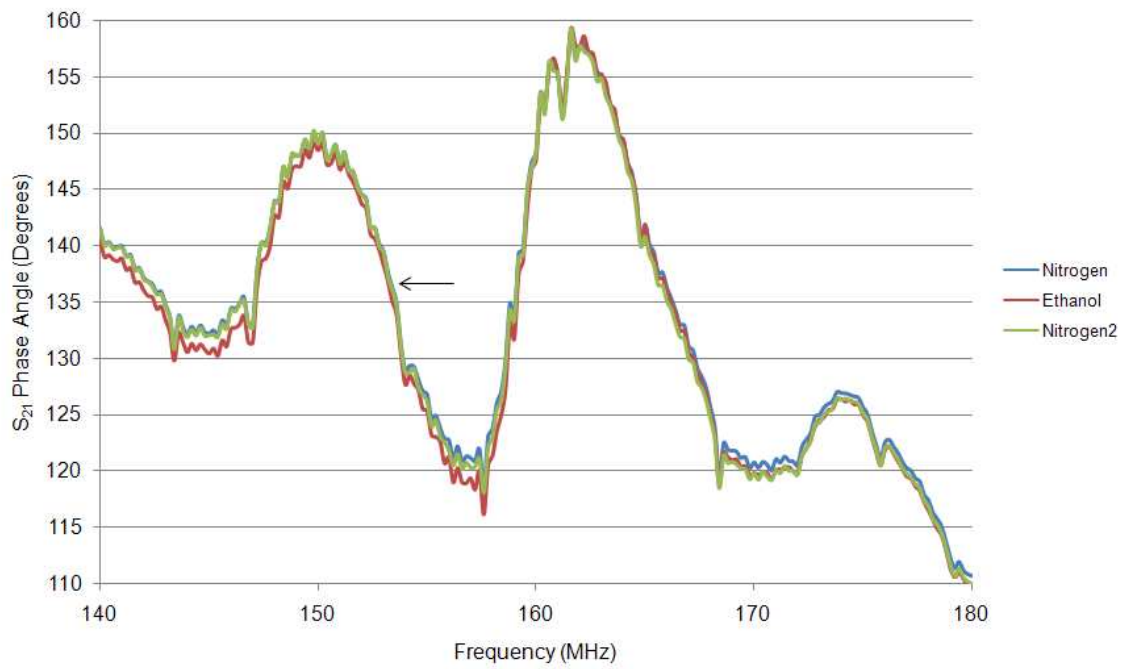


(b)

Figure 4.12: 10 micron Nafion coated device testing. Arrows indicate the resonance frequency. (a) S_{21} amplitude. Notice the circled unexpected frequency waves and the shifted resonance peak for the second nitrogen cycle (b) The second nitrogen cycle phase data is also shifted in frequency.



(a)



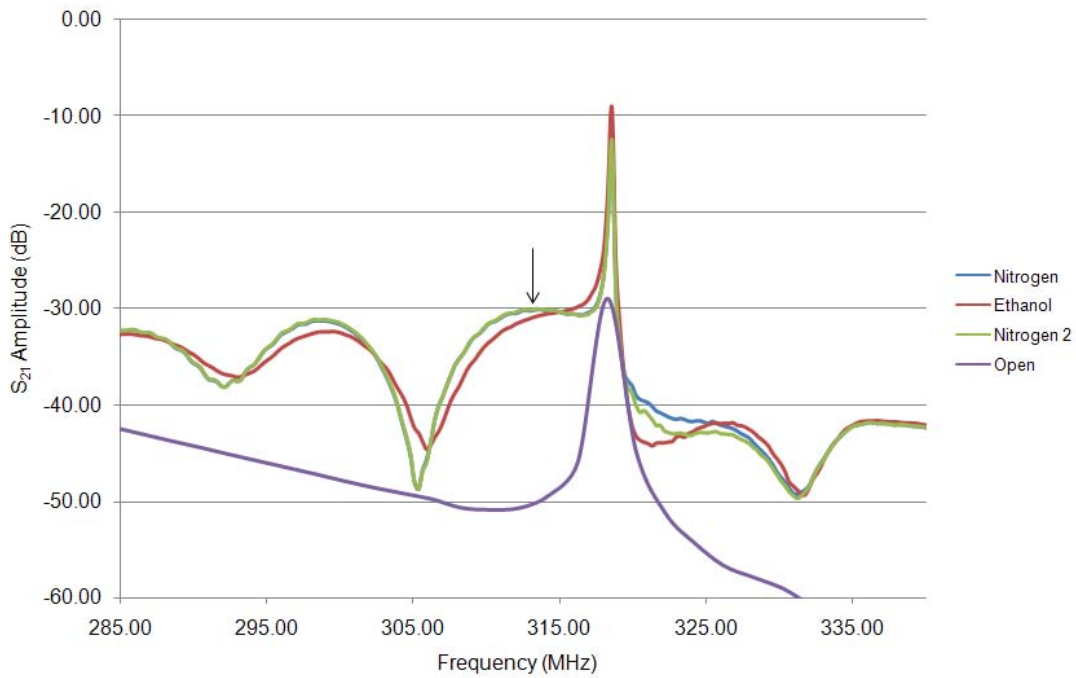
(b)

Figure 4.13: 6 micron Nafion coated device testing. Arrows indicate the resonance frequency, where data points are remarkably close. (a) S_{21} amplitude. (b) S_{21} phase.

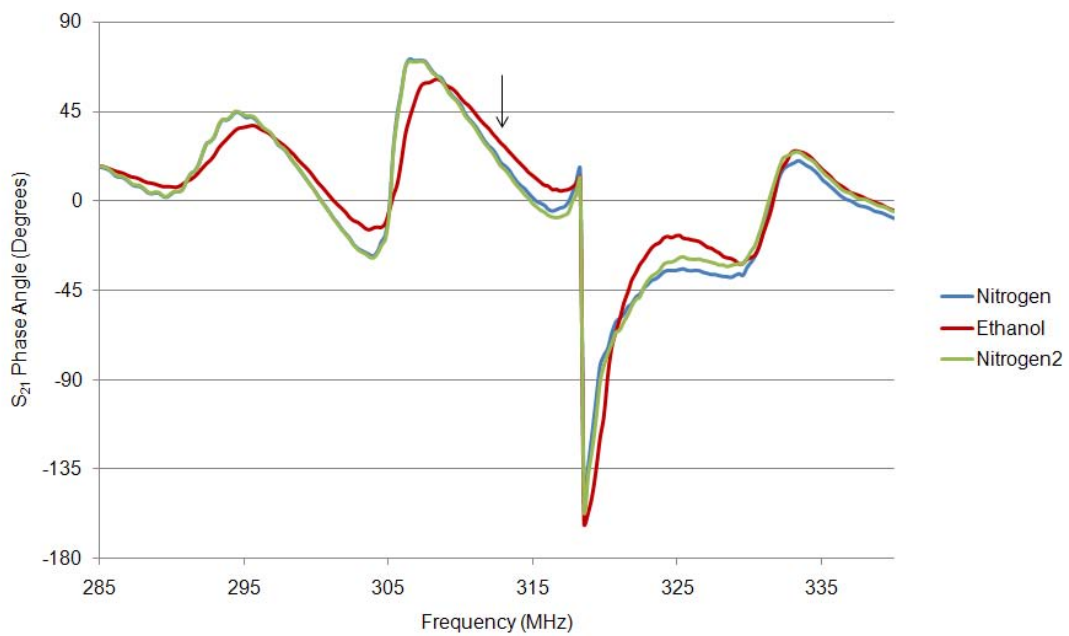
network analyzer was zoomed into several portions of the frequency response and the experiments repeated with similar results, confirming sensor activity. This data can be found in Appendix B.

4.6 Chapter Summary

A fabrication process was successfully developed using the initial mask available from AFRL. These devices demonstrated acoustic wave activity during electrical testing, but the electrical connections at the probes were found to be inconsistent. Due to increased device area and tighter tolerances, fabrication yields were reduced using the mask set designed at AFIT, but acceptable devices were fabricated and tested using this mask. Wire bonding to the devices was unsuccessful due to poor adhesion or thin bond pad layers, but alternate methods of creating stable electrical connections were obtained by stabilizing the probe station. Ethanol sensing was observed in both the phase and amplitude of the frequency response of one of the coated devices.



(a)



(b)

Figure 4.14: 3 micron Nafion-coated device testing. Arrows indicate the resonance frequency. (a) S_{21} amplitude. Notice the difference of the ethanol response from the nearly identical responses of the two nitrogen cycles. (b) The S_{21} phase also shows significant differences near resonance.

V. Conclusions

5.1 Results Analysis

5.1.1 Fabrication. The fabrication process is still not fully mature, as displayed by poor yields even in the final fabrication runs. Even with photoresist thicknesses well into the recommended ranges, bridging and poor metal adherence are observed on many of the devices. The root of this problem could eventually be traced to the method used to mount the chips to a larger wafer for metal evaporation. It is possible that the 110 °C heat used to cure the 1818 photoresist used as an adhesive is causing significant reflow of the 1805 imaging photoresist being used. Curved sidewalls could be leading to bridging while photoresist reforming in between the photoresist fingers could be preventing metal from adhering well to the substrate. Also, additional investigation of exposure and development times may be necessary, especially for doubled LOR3A layer lithography.

Using the plasma asher during fabrication has in general caused poor fabrication results. This seems to be caused by over-thinning of the photoresist layers, leading to bridging. On the other hand, the fabrication processes used have produced good devices. So far, the process that has created the best devices is that used in Series 6 devices. It is shown here in Table 5.1.

The color shift to red of the fingers with a layering scheme of titanium/aluminum/gold could be the result of intermetallics forming between the aluminum and gold layer. Since these form quickly at high temperatures, a barrier layer should be included if further high-temperature is required after deposition, and is possibly required for long-term material stability. Another possibility proposed for the color shift is some form of unknown contamination left on the devices after cleaning.

5.1.2 SAW Activity. Surface acoustic waves were successfully generated and detected using both first and second generation SAW devices fabricated in-house. This is demonstrated by the appearance of a sinc-shaped frequency response around the resonant frequencies as predicted by theory. Not only does this verify a workable

Table 5.1: Recommended Fabrication Process

Clean Chips Scrub samples with acetone soaked cotton swab Acetone spray for 20 seconds at 500 rpm Methanol rinse for 20 seconds at 500 rpm Nitrogen dry for 15 seconds at 500 rpm Bake on hotplate at 110 °C for 2 minutes
Photoresist Application (Spread/Spin) LOR3A at 500/3000 rpm for 5/30 seconds Bake on hotplate at 170 °C for 2 minutes Repeat LOR3A application and bake steps 1818 at 500/3000 rpm for 5/30 seconds* Bake on hotplate at 110 °C for 2 minutes
Exposure and Development Expose in EVG620 for 3 seconds Develop with LDD26W on spinner for 70 seconds Dry with nitrogen for 15 seconds
Premetallization Spin 1818 at 500 rpm on 3" wafer Arrange samples on wafer Bake at 110 °C for 3 minutes
Metal Deposition 100 Å Ti 750 Å Al 100 Å Ni 150 Å Au
Metal Liftoff Soak wafer in acetone for 30 minutes Remove chip from wafer Immerse chip in acetone filled dish Sonicate in phases until metal removal complete Immerse in 1165 at 110 °C for 10 min

fabrication process, but it also gives credibility to the SAW device design decisions and electrical testing setup.

5.1.3 Testing of Coated Chips. Whereas the center frequency of the uncoated devices was tested to be almost exactly at the calculated resonance frequency, the coated devices resonated at higher resonance frequency than predicted. This is the exact opposite of what was expected according to the mass-loading effect, which indicates that any added film should decrease the resonance frequency. While it is possible that the deposition of the Nafion film induced a stress in the substrate and led to a higher acoustic velocity, no precedent for this has been found. Since both cuts of lithium niobate substrate were used in the fabrication of the Series 3 wafers being tested, it is more likely that a 128° rotated-Y cut chip was accidentally switched with a Y-cut chip. The higher acoustic velocity of this cut would over-predict the measured resonance frequency somewhat, which would be expected if the Nafion film had lowered the resonance frequency due to mass loading.

All three devices showed small amplitude waves in the frequency response that are not predicted by the literature review. By observing these over time, it was apparent that they are systematic anomalies, not merely noise. These waves may result from the imperfect mathematical description of the spatial geometry of the IDTs. One assumption made in order to predict a sinc frequency response was to model the IDT as a spatial square wave multiplied by a pure sinusoid. This results in a frequency response formed by convolution of those component's respective Fourier Transforms: a sinc function and an impulse. However, the fabrication process used does not result in finger electrodes shaped like a sinusoid. Instead, the repeated finger pattern could be more accurately modeled as a spatial train of square waves. Since these square waves are composed of an infinite combination of sinusoids according to a Fourier series, the sinc function in the frequency domain is really convolved with an infinite ordered set of impulse functions, although only a few are non-negligible. The primary term falls at the resonance frequency originally predicted, but the smaller secondary and

tertiary terms may be responsible for the periodic waves in the frequency spectrum unexplained by the original model.

The primary difference between the devices tested was the critical line width and thus the resonant frequency of the devices. However, due to low fabrication yields, testable devices were only available that contained other variables, such as acoustic aperture, number of fingers, and IDT spacing. It is not clear why the samples did not all show sensing activity. Although the sensitivity of the 3 micron device was expected to be the largest due to the relationship between sensitivity and the square of the resonance frequency, this is not sufficient to explain the lack of sensing in the other devices. On the other hand, repeatable differences in the frequency response of the 3 micron device upon exposure to ethanol give strong evidence that it was indeed sensing the vapor. Testing on additional devices is necessary in order to fully explore this question.

Assuming that the shifts in the resonance peaks were due to ethanol vapor absorption by the Nafion film, several conclusions can be made. First, the decreasing amplitude of the S_{21} parameter indicates that additional attenuation is taking place as expected. On the other hand, the frequency shifts observed in both the amplitude and phase indicate a surface velocity increase upon vapor absorption. Because of this, it is reasonable to suggest that viscoelastic effects are dominant, and the film can be considered acoustically thick. Increased sensitivity could be investigated by experimenting with the thickness of the Nafion coating. Thicker films could enhance the viscoelastic effects as long as the additional attenuation does not prevent device operation. The film could also be made thinner in order to attempt to make the mass-loading effect dominant, although new deposition methods may be required to do so given the high spin speeds already used (6000 rpm).

5.2 *Future Project Recommendations*

5.2.1 Fabrication. We currently do not have sufficient devices to proceed with testing, thus future work will include additional fabrication. One of the first ideas to investigate is whether or not photoresist reflow is reducing resolution limits during adherence to the larger wafers. This can be done by inspecting the lithograph with an optical microscope and SEM before and after adhering them to a wafer with 1818.

Fabrication using larger wafers should be investigated. The inconsistency of the photoresist layers due to edge effects on the 1 cm² samples may have led to a large portion of the fabrication difficulties encountered. By fabricating with larger wafers, less time can be spent on each fabrication run while still obtaining larger yields.

Another possible direction in order to increase yield is to perform a metal etch rather than a liftoff procedure in order to form the metallic fingers. This involves safety hazards and extensive testing to generate a good etch process, so it should be used only if lift-off procedures continue to cause fabrication difficulties.

5.2.2 Investigation of Intermetallics. Further investigation could be attempted to discover the cause of the discoloration observed in the metal fingers of the acoustic wave device. This could be accomplished using XPS analysis on the samples, which should be able to distinguish between the two proposed possibilities of gold/aluminum intermetallics or wafer contamination.

5.2.3 Sensor Testing. Additional sensing layers should be prepared for testing. These should include the investigation of both different methods to deposit Nafion and different methods to attach biological molecules to the substrate without denaturing them. All sensing layers fabricated should be tested with the network analyzer for sensitivity. This should help explain the inconsistent results during sensing.

The vapor testing setup should be investigated further so that exact concentrations of ethanol are known. This would allow the Nafion sensors created to be compared to other sensor types available in literature.

The time dependence of the frequency response should be investigated. Since speed of detection can be a critical issue in battlefield sensors, the figures of merit of the fabricated devices should be tested. This will be limited by the speed at which the network analyzer can save samples in manual mode, but it should be enough to provide sufficient information.

Since fabrication difficulties limited the variety of devices available for test, there are still several design variables that have not been optimized for sensing, such as IDT spacing, the number of finger pairs, and the width of the acoustic aperture. With additional fabrication, these parameters may be investigated in order to find how to best design SAW sensors.

5.2.4 Oscillator Design. While the network analyzer setup may be sufficient for initial testing, in order to transition this technology to the warfighter a more mobile, robust, and inexpensive measurement technology is required. Work should begin in order to integrate a SAW sensor chip into an oscillator circuit. Not only is this much more inexpensive and portable, but it also encourages the development of arrays of acoustic wave sensors that would allow for more advanced pattern recognition and selectivity. An oscillator unit could be as simple as a few discrete elements on a printed circuit board with a microcontroller used to perform the pulse counting.

5.2.5 Preconcentrator Design. One of the most important criteria for a vapor sensing device is high sensitivity to the vapor of interest. Since many explosives have very low partial pressures, any sensors created for explosives detection should be designed to be as sensitive as possible. One method of increasing a sensor's effective sensitivity is to use a preconcentrator to deliver a concentration of analyte to the sensor higher than what is present in the air.

5.2.6 Packaging. Since the SAW sensor device must be open to ambient air in order to function, environmental effects must be considered. The electrodes can be made largely resistant to corrosion by fabricating the outermost layer with gold, as was done during this thesis. The effects of frequency drift due to non-specific mass adsorption can be minimized by incorporating a nanoporous filter on the vapor flow inlet to remove the vast majority of interfering large particles. The sensing layer will likely be the most difficult component of the SAW system to maintain, since biological molecules tend to break down over time if not properly stored frozen in a buffer solution. One possibility for increasing the lifetime of devices coated with biological molecules is to support them in a semi-aqueous environment such as a hydrogel.

5.3 Conclusions

In conclusion, this thesis contributed significant progress towards the goals of this project, but much remains to be done. Devices were successfully designed, fabricated, and coated with a polymer sensing layer. The sensing of ethanol due to viscoelastic effects was conclusively demonstrated using frequency response analysis. Future work includes application of a biomolecular sensing layer, circuitry design for handheld devices, and a MEMS preconcentrator. This work should remain a priority for future AFIT and AFRL research.

Appendix A. Fabrication Details

A.1 Fabrication of AFRL-Designed Devices

Series 1 was split into two separate runs, ‘A’ and ‘B’. When the results of the lithography were observed, it was decided to remove the photoresist with a soak in 1165 at 120 °C for 10 minutes. The lithography steps were then repeated on the same chips with different exposure and development times. These Series 1A chips served the purpose of initial attempts at fabricating small features using processes developed previously. .

Table A.1: Series 1a Lithography Process. *See following table for details

Clean Chips Acetone spray for 20 seconds at 500 rpm Methanol rinse for 20 seconds at 500 rpm Nitrogen dry for 15 seconds at 500 rpm Bake on hotplate at 110 °C for 2 minutes
Photoresist Application (Spread/Spin) LOR3A at 500/4000 rpm for 5/30 seconds Bake on hotplate at 170 °C for 2 minutes 1805 at 500/4000 rpm for 5/30 seconds Bake on hotplate at 110 °C for 75 seconds
Exposure and Development Expose in EVG620 for 2 seconds Developing times with LDD26W at 500 rpm* Dry with nitrogen for 15 seconds
Clean Chips Soak in 1165 at 120 °C for 10 minutes Acetone Spray for 20 seconds at 500 rpm Methanol Rinse for 20 seconds at 500 rpm Nitrogen dry for 15 seconds at 500 rpm Bake on hotplate at 110 °C for 2 minutes
Photoresist Application (Spread/Spin) LOR3A at 500/4000 rpm for 5/30 seconds Bake on hotplate at 170 °C for 2 minutes 1805 at 500/* rpm for 5/30 seconds Bake on hotplate at 110 °C for 75 seconds
Exposure and Development Exposure in EVG620* Develop with LDD26W at 500 rpm* Dry with nitrogen for 15 seconds

Table A.2: Series 1a Lithography Details

Sample	Develop 1	Spin Speed	Exposure	Develop 2
1	60 sec	2500 rpm	2	1, 30 sec, 60 sec
2	60 sec	2500 rpm	1.5 sec	30 sec
3	20 sec	4000 rpm	1.5 sec	15 sec
4	20 sec	4000 rpm	1.5 sec	5 sec
5	15 sec	4000 rpm	2 sec	60 sec
6	10 sec	4000 rpm	2 sec	30 sec
7	5 sec	4000 rpm	1.8 sec	60 sec
8	3 sec	4000 rpm	1.5 sec	30 sec

Series 1B chips helped to refine the process for better pattern transfer using a variety of different exposure and development times. The settings on the EVG620 were altered to explore the differences between contact and proximity lithography. Additionally, the better lithography results provided the first opportunity to deposit metal using the Torr-EB-4P-6KW e-beam evaporation system. After fabrication these devices were investigated with both an optical microscope and a profilometer.

Table A.3: Series 1b Lithography Process. *See following table for details

Clean Chips Soak in 1165 at 120 degrees for 10 minutes Acetone spray for 20 seconds at 500 rpm Methanol rinse for 20 seconds at 500 rpm Nitrogen dry for 15 seconds at 500 rpm Bake on hotplate at 110 °C for 2 minutes
Photoresist Application (Spread/Spin) LOR3A at 500/4000 rpm for 5/30 seconds Bake on hotplate at 170 °C for 2 minutes 1805 at 500/4000 rpm for 5/30 seconds Bake on hotplate at 110 °C for 75 seconds
Exposure and Development Exposure in EVG620* Developing times from 3-60* seconds with LDD26W at 500 rpm Dry with nitrogen for 15 seconds
Premetallization Spin 1818 at 500 rpm on 3" wafer Arrange samples on wafer Bake at 110 °C for 4 minutes
Metal Deposition 750 ÅAl 250 ÅAu
Metal Liftoff Soak wafer in acetone for 5 minutes Remove chip from wafer Immerse chip in acetone filled dish Sonicate in phases until metal removal complete Immerse in 1165 at 110 °C for 10 min

Table A.4: Series 1b Lithography Details

Sample	Exposure (sec)	Develop (sec)
1	2	30
2	2	30
3	1.5	30
4	1.5	25
5	1.5	25
6	1.5	25
7	1	25
8	1.3	25

Due to the metal bridging observed in Series 1B, it was decided to lower the photoresist deposition spin speed in order to gain thicker resist layers. There were several possible causes for poor adhesion, and thus several measures were used to attempt to fix it. First, even though the 1805 layer appeared to be patterned well, if the LOR was not completely developed through to the substrate, then the metal would not stick well. Two measures were put in place in order to avoid this problem. Extra care was taken during visual inspection of the developed photoresist to make sure it was completely developed at different focus heights. Also, a selection of chips used the plasma asher in order to clean up any remaining photoresist in the developed areas. Another possible cause of poor adhesion was poor material properties in the adhesion of aluminum to lithium niobate. In response, a 100 Å layer of titanium was introduced to several samples in order to promote adhesion.

As a result of these variety of changes, the Series 2 included a matrix of possible solutions to the problem in order to ascertain which solutions produced the best results. All of the chips were spin-coated at 3000 rpm with LOR3A and 1805. Variables included the titanium adhesion layer, the use of the asher, and two different exposure/development combinations.

Having what appeared to be a good process from the excellent results of Sample 2.1, the next run repeated the procedures that produced these results. This was done to produce a set of identical devices for testing purposes.

Table A.5: Series 2 Lithography Process

Clean Chips Acetone spray for 20 seconds at 500 rpm Methanol rinse for 20 seconds at 500 rpm Nitrogen dry for 15 seconds at 500 rpm Bake on hotplate at 110 °C for 2 minutes
Photoresist Application (Spread/Spin) LOR3A at 500/3000 rpm for 5/30 seconds Bake on hotplate at 170 °C for 2 minutes 1805 at 500/3000 rpm for 5/30 seconds Bake on hotplate at 110 °C for 90 seconds
Exposure and Development Expose in EVG620 for 2 seconds (1.5 seconds for 2.5, 2.6) Develop with LDD26W on spinner for 30 seconds (45 seconds for 2.5,2.6) Dry with nitrogen for 15 seconds
Plasma Ash 75 W for 7.5 min; 100W for 5 min (2.3 only) 100 W for 10 min (Sample 2.4 only)
Premetallization Spin 1818 at 500 rpm on 3" wafer Arrange samples on wafer Bake at 110 °C for 3 minutes
Metal Deposition 100 ÅTi (2.1, 2.3, 2.5 only) 750 ÅAl 250 ÅAu
Metal Liftoff Soak wafer in acetone for 5 minutes Remove chip from wafer Immerse chip in acetone filled dish Sonicate in phases until metal removal complete Immerse in 1165 at 110 °C for 10 min

Table A.6: Series 3 Lithography Process

Clean Chips Acetone spray for 20 seconds at 500 rpm Methanol rinse for 20 seconds at 500 rpm Nitrogen dry for 15 seconds at 500 rpm Bake on hotplate at 110 °C for 2 minutes
Photoresist Application (Spread/Spin) LOR3A at 500/3000 rpm for 5/30 seconds Bake on hotplate at 170 °C for 2 minutes 1805 at 500/3000 rpm for 5/30 seconds Bake on hotplate at 110 °C for 90 seconds
Exposure and Development Expose in EVG620 for 2 seconds Develop with LDD26W on spinner for 30 seconds (35 seconds for 3.3) Dry with nitrogen for 15 seconds
Premetallization Spin 1818 at 500 rpm on 3" wafer Arrange samples on wafer Bake at 110 °C for 3 minutes
Metal Deposition 100 ÅTi 750 ÅAl 250 ÅAu
Metal Liftoff Soak wafer in acetone for 5 minutes Remove chip from wafer Immerse chip in acetone filled dish (3.2 and 3.4 attempted alternate tape liftoff) Sonicate in phases until metal removal complete Immerse in 1165 at 110 °C for 10 min

A.2 Fabrication of AFIT-Designed SAW Devices

Series 4 chips were fabricated using the same processes as Series 3, but it was found that shorter development times were required. After metal evaporation, a number of shorts were observed due to the increased importance of wafer cleanliness on the larger devices. These shorts were attempted to be burnt out with a high applied voltage. This series was also used to test the deposition of bond pads.

Table A.7: Series 4 Development Times

Sample	Development (sec)
1	30
2	30
3	27
4	25
5	25

Series 5 included the additional cleaning step of scrubbing with cotton swabs soaked in acetone before proceeding with fabrication. A second LOR layer was tested on this series to reduce bridging. It was decided to insert a 100 Å layer of nickel between the two layers to reduce intermetallics found in Series 4 while maintaining conductivity over time.

Table A.8: Series 5 Fabrication

Clean Chips Scrub samples with acetone soaked cotton swab Acetone spray for 20 seconds at 500 rpm Methanol rinse for 20 seconds at 500 rpm Nitrogen dry for 15 seconds at 500 rpm Bake on hotplate at 110 °C for 2 minutes
Photoresist Application (Spread/Spin) LOR3A at 500/3000 rpm for 5/30 seconds (2 layers for 5.3, 5.4) Bake on hotplate at 170 °C for 2 minutes 1805 at 500/3000 rpm for 5/30 seconds Bake on hotplate at 110 °C for 90 seconds
Exposure and Development Expose in EVG620 for 2 seconds Develop with LDD26W on spinner for 22 seconds Dry with nitrogen for 15 seconds
Premetallization Spin 1818 at 500 rpm on 3" wafer Arrange samples on wafer Bake at 110 °C for 3 minutes
Metal Deposition 100 ÅTi 750 ÅAl 100 ÅNi 150 ÅAu
Metal Liftoff Soak wafer in acetone for 5 minutes Remove chip from wafer Immerse chip in acetone filled dish Sonicate in phases until metal removal complete Immerse in 1165 at 110 °C for 10 min

Series 6 lithography proceeded using two LOR layers before spinning on the imaging resist. Additionally, several of the chips replaced the 1805 photoresist with the more viscous 1818 photoresist, leading to increased thickness. Both of these alterations were designed to reduce the amount of bridging observed.

Table A.9: Series 6 Fabrication. *Samples 6.5 - 6.7 used a single 2000 rpm LOR and 3000 rpm 1805. **See following table.

Clean Chips Scrub samples with acetone soaked cotton swab Acetone spray for 20 seconds at 500 rpm Methanol rinse for 20 seconds at 500 rpm Nitrogen dry for 15 seconds at 500 rpm Bake on hotplate at 110 °C for 2 minutes
Photoresist Application (Spread/Spin) LOR3A at 500/3000 rpm for 5/30 seconds* Bake on hotplate at 170 °C for 2 minutes Repeat LOR3A application and bake steps* 1818 at 500/3000 rpm for 5/30 seconds* Bake on hotplate at 110 °C for 2 minutes
Exposure and Development Expose in EVG620** Develop with LDD26W on spinner for 22 seconds Dry with nitrogen for 15 seconds
Plasma Ash 75 W for 2 min (6.1, 6.2 only)
Premetallization Spin 1818 at 500 rpm on 3" wafer Arrange samples on wafer Bake at 110 °C for 3 minutes
Metal Deposition 100 ÅTi 750 ÅAl 100 ÅNi 150 ÅAu
Metal Liftoff Soak wafer in acetone for 30 minutes Remove chip from wafer Immerse chip in acetone filled dish Remove excess metal with tweezers Sonicate in phases until metal removal complete Immerse in 1165 at 110 °C for 10 min

Table A.10: Series 6 Lithography Details

Sample	Exposure (sec)	Development (sec)
1	2.5	65, 75, 80
2	3	65, 70
3	3	70
4	3	70
5	2	22
6	2	22
7	2	22

Table A.11: Series 6 Lithography Details.

Since all fabrication up to this point had been done using lithium niobate wafers, Series 7 chips were fabricated on quartz wafers. Since some sources suggested the need for an adhesion layer, several samples included a hexamethyldisilazane (HDMS) layer before applying photoresist. Note, the change in the metal layer was due to the delamination of the bond pads during wire bonding, which had been attempted prior to this fabrication run.

Table A.12: Series 7 Fabrication. *See following table.

Clean Chips Scrub samples with acetone soaked cotton swab Acetone spray for 20 seconds at 500 rpm Methanol rinse for 20 seconds at 500 rpm Nitrogen dry for 15 seconds at 500 rpm Bake on hotplate at 110 °C for 2 minutes
Photoresist Application (Spread/Spin) HDMS at 500/4000 rpm for 5/30 seconds (7.4, 7.5 only) Bake on hotplate at 110 °C for 75 seconds LOR3A at 500/3000 rpm for 5/30 seconds Bake on hotplate at 170 °C for 2 minutes Repeat LOR3A application and bake steps Photoresist at 500/3000 rpm for 5/30 seconds* Bake on hotplate at 110 °C for 2 minutes
Exposure and Development Expose with EVG620* Develop with LDD26W by immersion* Dry with nitrogen for 15 seconds
Premetallization Spin 1818 at 500 rpm on 3" wafer Arrange samples on wafer Bake at 110 °C for 3 minutes
Plasma Ash 75 W for 2 min
Metal Deposition 200 ÅTi 800 ÅAu
Metal Liftoff Soak wafer in acetone for 10 minutes Remove chip from wafer Immerse chip in acetone filled dish Remove excess metal with acetone stream Sonicate in phases until metal removal complete Immerse in 1165 at 110 °C for 10 min

Table A.13: Series 7 Lithography Details.

Sample	Photoresist Used	Exposure (sec)	Development (sec)
1-7	1805	2	22
8-9	1818	2.5	60
10	1818	3	60

In order to prevent the delamination that had been occurring during wire bonding, Series 8 chips began by depositing the bond pad layer before the device lithography. This put the novel metal stacking layer on top and reduced the amount of interfaces where delamination could occur. During this series, it was found that mask contamination was causing poor lithography, resulting in incomplete processing.

Table A.14: Series 8 Fabrication.

Clean Chips Scrub samples with acetone soaked cotton swab Acetone spray for 20 seconds at 500 rpm Methanol rinse for 20 seconds at 500 rpm Nitrogen dry for 15 seconds at 500 rpm Bake on hotplate at 110 °C for 2 minutes
Photoresist Application (Spread/Spin) LOR3A at 500/3000 rpm for 5/30 seconds Bake on hotplate at 170 °C for 2 minutes Repeat LOR3A application and bake steps twice 1818 at 500/3000 rpm for 5/30 seconds Bake on hotplate at 110 °C for 2 minutes
Exposure and Development Expose with EVG620 for 3 seconds Develop with LDD26W for 70 seconds Dry with nitrogen for 15 seconds

There appeared to be contamination or an aberration on the mask that was not coming off during a normal acetone cleaning. One possibility was that LOR3A photoresist had become stuck to the mask during an error with the EVG620 in which the mask contacted a chip with excessive force. In order to test this, the mask was immersed into 1165 stripper heated to 140 °C, which should have removed any LOR or 1805 on the mask easily. Attempts were made to remove the contamination with 1165 or acetone and a foam swab. Another possible cause of the contamination was damage to the mask. Since this was the only area of the mask that contained bond pads, it was decided to order another mask. This mask included a number of redundant patterns of basic SAW devices and bond pads, as well as inverted patterns

of the basic device to enable an etching process during future research. Finally, this mask included several additional designs and calibration locations.

The project was progressing to a point where continuing to attempt to salvage the lithium niobate wafer contaminated from the dicing process was no longer feasible due to a lack of time. The remaining lithium niobate wafers were diced with a diamond saw after a layer of 1818 photoresist was applied in order to collect the debris from the saw. Series 9 wafers used the newly-diced lithium niobate. Both single and double LOR layers were attempted.

Series 10 continued the attempts to fabricate additional working SAW devices. Since it was possible that the two minute bake on the hotplate was resulting in over-baked photoresist, this time was lowered to 90 seconds. Additionally, the generally poor results when using a double LOR layer could indicate immature exposure and development times. These parameters were varied on several of the chips in order to investigate this.

Table A.15: Series 9 Fabrication.

Clean Chips Acetone spray for 20 seconds at 500 rpm Methanol rinse for 20 seconds at 500 rpm Nitrogen dry for 15 seconds at 500 rpm Bake on hotplate at 110 °C for 5 minutes
Photoresist Application (Spread/Spin) LOR3A at 500/3000 rpm for 5/30 seconds Bake on hotplate at 170 °C for 2 minutes Repeat LOR3A application and bake steps (9.1-9.3 only) 1805 at 500/3000 rpm for 5/30 seconds Bake on hotplate at 110 °C for 2 minutes
Exposure and Development Expose with EVG620 for 2 seconds Develop with LDD26W on spinner for 22 seconds Dry with nitrogen for 15 seconds
Premetallization Spin 1818 at 500 rpm on 3" wafer Arrange samples on wafer Bake at 110 °C for 3 minutes
Metal Deposition 200 ÅTi 890 ÅAu
Metal Liftoff Soak wafer in acetone for 2 hours Remove chip from wafer Immerse chip in acetone filled dish Remove excess metal with acetone stream Sonicate in phases until metal removal complete Immerse in 1165 at 110 °C for 10 min

Table A.16: Series 10 Fabrication. *See following table for details.

Clean Chips Acetone spray for 20 seconds at 500 rpm Methanol rinse for 20 seconds at 500 rpm Nitrogen dry for 15 seconds at 500 rpm Bake on hotplate at 110 °C for 5 minutes
Photoresist Application (Spread/Spin) LOR3A at 500/3000 rpm for 5/30 seconds* Bake on hotplate at 170 °C for 2 minutes* Photoresist at 500/3000 rpm for 5/30 seconds* Bake on hotplate at 110 °C for 90 seconds
Exposure and Development Expose with EVG620* Develop with LDD26W on spinner* Dry with nitrogen for 15 seconds

Table A.17: Series 10 Fabrication Details.

Sample	LOR3A Layers	PR Used	Exposure	Development
1-3	1	1805	2.2 sec	22 sec
4	2	1818	2.5 sec	65 sec
5	2	1818	3.3 sec	70 sec
6	2	1818	3.6 sec	50 sec

A.3 Wire Bonding

‘Loop’ refers to the height at which the bonder returns to between bonds. Thus, a higher number results in a larger diameter wire loop connecting the two bond points. ‘Tail’ is the amount of wire left after the second bond before breaking the wire. ‘Power’ is a unitless measure of the amplitude of piezoelectric vibrations used to aid the bonding process. ‘Time’ is the time in seconds taken to create a single bond. ‘Force’ refers to the downward force applied during the bond. Finally, ‘Temperature’ is the temperature of the bonder stage, not the temperature of the device being bonded.

Wire bonding began using a clean chip carrier and settings recommended for use from previous operators of the wire bonder, as given in Appendix 1. Initial bonding tests began on the gold of the chip carrier only, since this was likely to be much easier to bond to and was more easily replaced than the fabricated SAW devices. If certain wire bonder settings created good bonds on the chip carrier, the same settings were used on nonfunctional SAW devices that still had good bond pads. The first set of tests that began with the recommended settings is referred to as Test Set A.

Table A.18: Wire Bonding Test Set A

	Loop	Tail	Power	Time	Force	Tear	Temp (°C)
First Bond	3	-	8.61	2.5 sec	1.5	-	100
Second Bond	-	8	8.81	2.5 sec	1.5	2.5	100

For Test Set B, the clamps were connected to the main package of the chip carrier in order to create a better thermal contact with the heated stage. Additionally, the temperature of the stage was increased to 120 °C. The complete settings are given in Appendix 1, which were then altered systematically in order to attempt to find good bond settings.

Table A.19: Wire Bonding Test Set B and C

	Loop	Tail	Power	Time	Force	Tear	Temp (°C)
First Bond	7.7	-	8.8	3 sec	1.5	-	120
Second Bond	-	3	8.8	3 sec	1.5	2.5	120

Test Set C used a new chip carrier whose leads were designed such that the main carrier stood significantly off the surface of the stage. To obtain good thermal contact, a smaller chip carrier was placed underneath the one being bonded to. To test the relative temperature difference, an electronic thermocouple was clamped to the top of the chip carrier. Again a variety of settings were used, but at a substrate temperature of 160 °C.

Test Set D was based on recommended settings found in the wire-bonding manual. Since the diameter of the wire was not known initially, both the recommended settings for 25 micron and 18 micron wire were attempted, as well as variations of them.

Table A.20: Wire Bonding Test Set D - 18 Micron Wire

	Loop	Tail	Power	Time	Force	Tear	Temperature (°C)
First Bond	3	-	0-1	3 sec	0-1	-	150
Second Bond	-	3	1-2	3 sec	0-1	4	150

As shown in the results section, it became apparent that the bond pads needed to be thicker in order to wire bond to them successfully. Since the SAW devices must stay thin in order to minimize acoustic impedance changes on the substrate, it was necessary to build thicker bond pads as a separate lithography step. This was tested using the Series 4 chips to allow process testing without risking the few good chips available. This procedure used 3 coats of LOR3A and 1818 to prepare for a 5000 Å gold deposition. This thickness was chosen based on advice from experienced MEMS experts as a sufficiently thick layer in order to bond with. Thicker metal would possibly increase the chances of successful bond, but would also increase the chances of poor lithography from an improper ratio of LOR3A to metal thickness.

The wire bonder was used to attempt to connect these thicker pads to a chip carrier. Again, a variety of settings beginning with those recommended by the equipment manufacturer were attempted. Every time the settings were changed, the wire bonding was tested on the chip carrier. This ensured that the weak link in the bonding process was indeed the SAW device, not an error with the gold thread, which

occurred fairly often. Bonding to the SAW devices was attempted on both the first and second bonds. These wire bonding attempts are referred to as Test Set E.

Since several chips from Series 5 and 6 that appeared to have good devices were still unused, it was decided to put bond pads on them in order to increase the likelihood of successful probe measurements. Three layers of LOR3A and a layer of 1818 were deposited using the spinner at 3000 rpm to prepare for metal evaporation of 7500 Å of gold. This layer was decided due to the continuing poor results from wire bonding to the thickened bond pads of Series 4.

The completed SAW devices with bond pads from Series 5 and 6 were taken to the wire bonder. With the additional metal thickness from the bond pad lithography, the metal was now 8500 Å thick, which should have been sufficient to create a good metal bond. To test this, these devices were brought to the wire bonder at AFR-L/RXB. Numerous tests based on the recommended settings for 25 micron diameter wire were run as a part of Test Set F.

Table A.21: Wire Bonding Test Set D - 25 Micron Wire

	Loop	Tail	Power	Time	Force	Tear	Temp (°C)
First Bond	4	-	1-2	5 sec	1-2	-	150
Second Bond	-	5	2	5 sec	1-2	5	150

Appendix B. Additional Results

B.1 Fabrication

B.1.1 Wafer Dicing. When attempting to cleave a lithium niobate wafer using a diamond tipped pen, the first wafer cleaved along a curved path. As was discovered from further research, lithium niobate crystallizes into a hexagonal structure, which makes cleaving the wafers into square segments highly difficult. This crystal structure also explained the 120 degree offset between the two cleavage lines. It was found that quartz also possesses hexagonal symmetry.

Two lithium niobate wafers were sent to AFRL/RY to be diced using a diamond saw. This procedure was successfully able to make square wafer samples with sides of 1 cm, but left a significant amount of debris on the samples. Some chipping was observed near the edges of the diced wafer. Additionally, when removing the diced wafers from the sticky backing, additional chipping occurred due to contact between samples. This led to increasing amounts of debris as more samples were removed from the backing. Since the initial wafers diced did not have a protective photoresist layer at the time of dicing, the debris directly contaminated the surface of the samples. This resulted in continual difficulties during lithography, as will be seen in the following discussions on fabrication. When the diamond saw was used to dice the wafers protected by 1818 photoresist, excellent cleanliness was observed.

When the quartz wafers were diced using the diamond saw, the protective photoresist delaminated from the wafer surface early in the process. A possible solution to this could be a deposition of HDMS prior to the photoresist to act as an adhesion layer. The delamination resulted in similar surface contamination as the lithium niobate wafer that was diced without a protective photoresist.

B.1.2 Series 1-3 Fabrication. When Series 1A wafers were developed for a range of 5 to 60 seconds, either none of the photoresist remained as shown in Figure B.1 or only poor patterns developed as in Figure B.2.

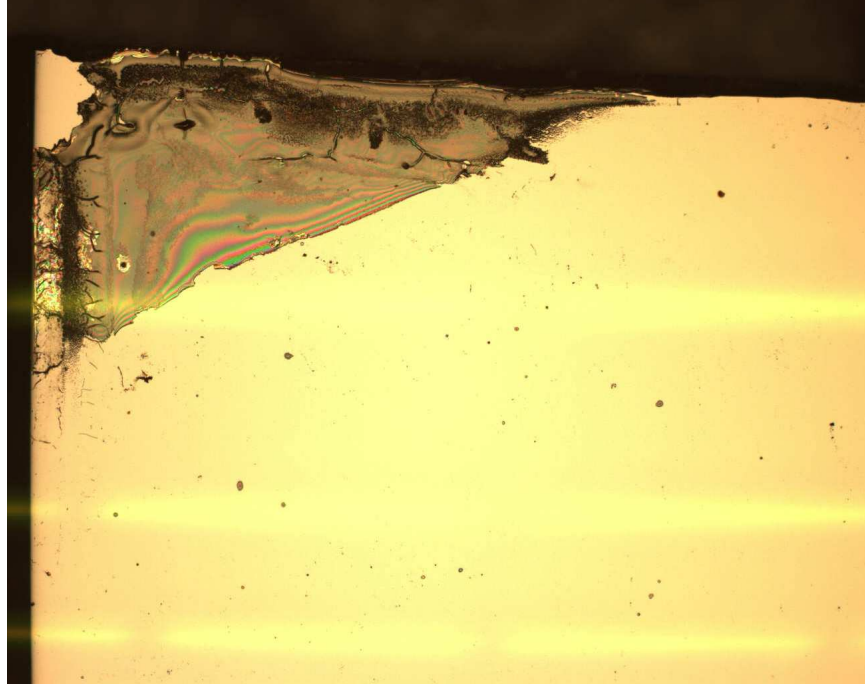


Figure B.1: Sample 1A wafer

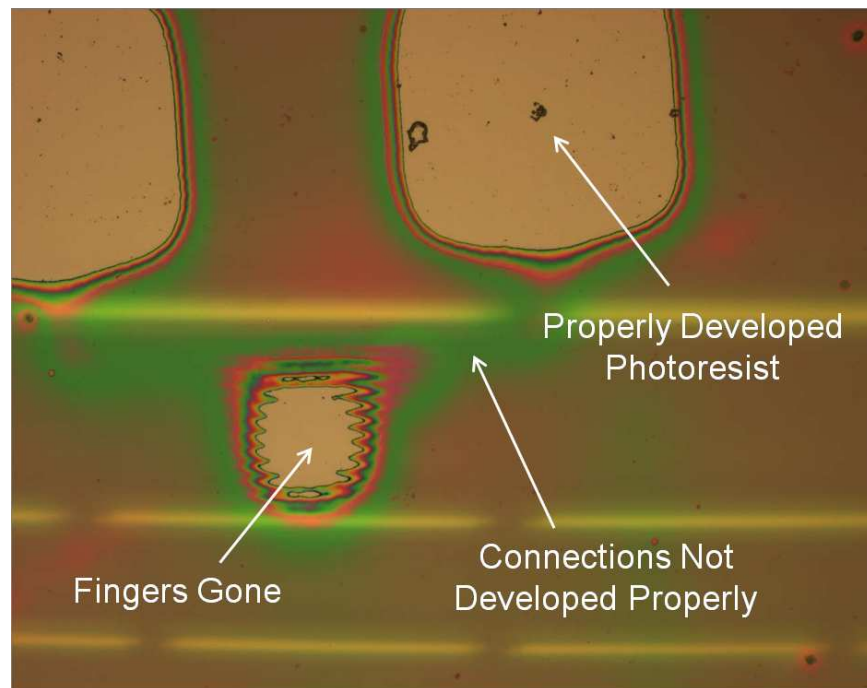


Figure B.2: Second run of sample 1a.8b after LOR3A and 1805 at 3000 rpm. Exposed 1.5 seconds and developed 45 seconds

It was found that the mask was inserted into the EVG620 incorrectly due to the mask not being mirrored. Once the mask was flipped over, patterns began to come out much better, but surprisingly low development times were needed in the range of 5 seconds. It was theorized the photoresist was not soft-baked long enough, so subsequent runs used a longer bake time.

After fabricating Series 3 wafers according to the best results from Series 2, metal lift-off was attempted using cellophane tape on Samples 3.2 and 3.4 with poor results. Lift-off using an acetone soak and sonication generally resulted in much better devices as shown in Figure B.3. A number of devices were judged to be satisfactory due to no observed bridging or voiding under an optical microscope.

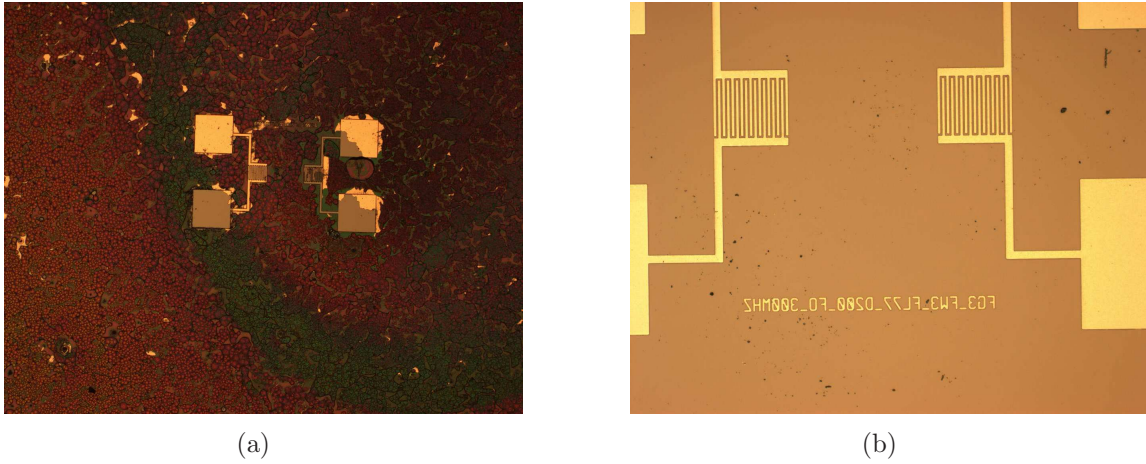


Figure B.3: Series 3 Lift-off (a) Tape lift-off. (b) Acetone soak and ultrasonic bath lift-off.

While performing the lithography on Series 3, areas of contamination were observed in the LOR3A layer even before baking, as shown in Figure B.4. The only chips where this was not observed were 3.5 and 3.6. It is likely that this phenomenon was observed due to crystals formed in the eyedropper used to transfer photoresist to the chips. Once enough fresh photoresist was drawn into the eyedropper, the problem disappeared.

These problems continued when the photoresist was developed. The areas with the contamination tended to have significant abnormalities, as shown in Figures B.5.

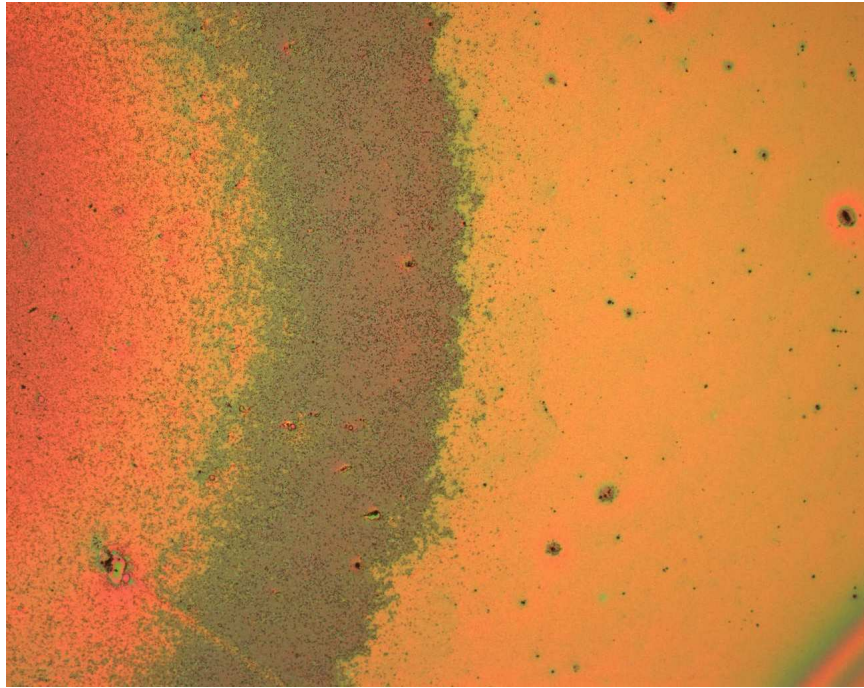


Figure B.4: Sample 3.2 shows contamination in the LOR3A photoresist layer

On the other hand, in non-contaminated areas the lithography turned out well, such as in Figure B.6, although overdevelopment was still occasionally observed as in Figure B.7.

After metallization, a large amount of dunes were observed in the metal layers of 3.1, 3.2, 3.4, and 3.5. An example of this is shown in Figure B.8. This phenomenon was localized to the area away from the devices, and did not appear to have an effect on them.

B.2 Testing at AFIT with Micromanipulator Probe Station

Sufficient devices were fabricated successfully out of Series 3 to proceed to electronic testing. For the first test using the Micromanipulator Company probe station at AFIT, BNC cables, and N-type to BNC adapters to connect the network analyzer to a good SAW device on Sample 3.1, the network analyzer displayed a peak in S_{21} at 85 MHz regardless of whether or not the probes were in contact with the SAW device. In this case, an alligator clip was used to connect the ground of the BNC to

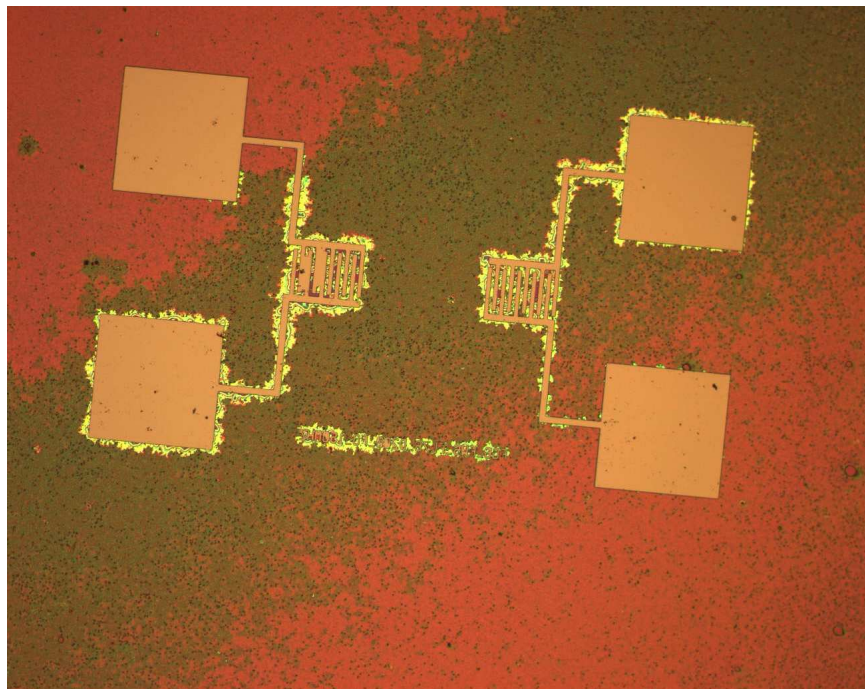


Figure B.5: Sample 3.2 shows unusual photoresist after development

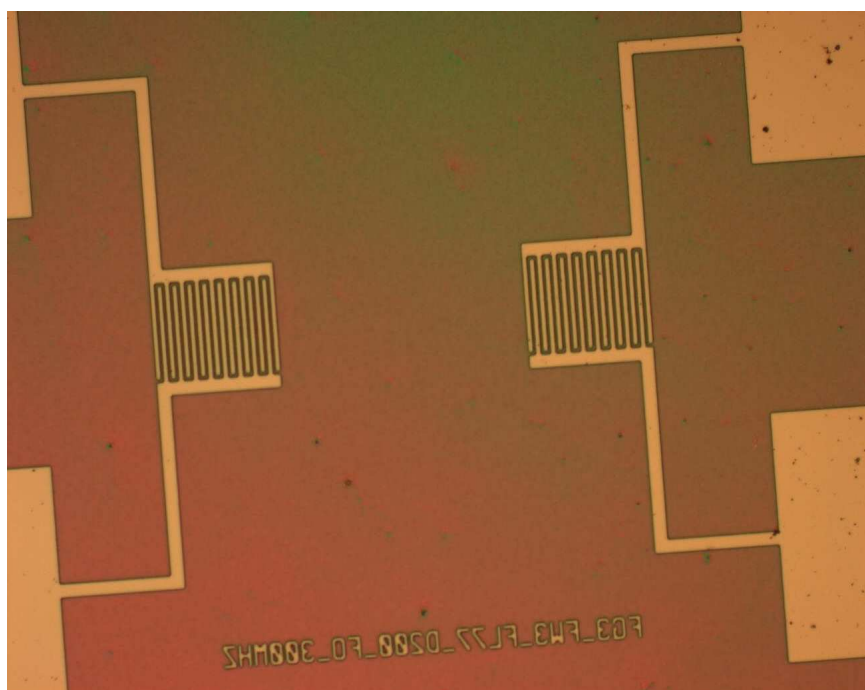


Figure B.6: Sample 3.1 shows good patterning outside of contaminated area.

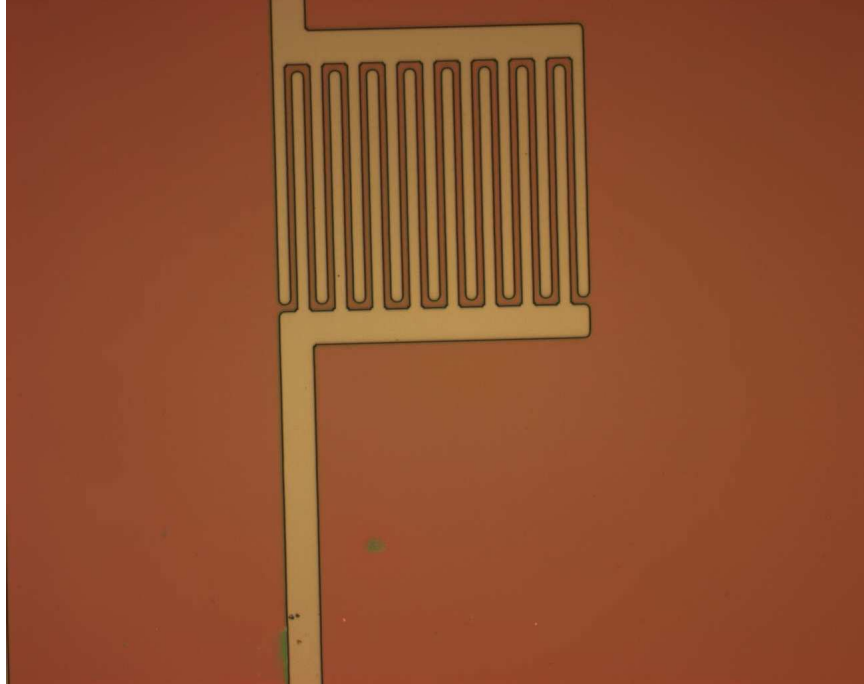


Figure B.7: Sample 3.6 is slightly overdeveloped as shown by over-wide fingers and the rounding of corners.

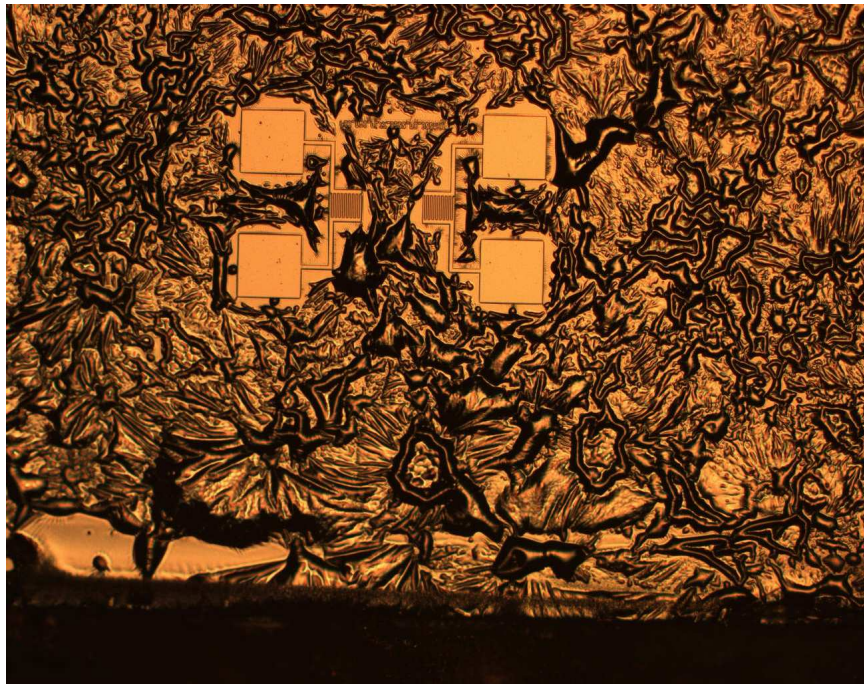


Figure B.8: Sample 3.1 showing dunes after metallization.

another probe. In the second test, a BNC to butterfly adaptor cable was used to split the signal to separate probes, with nearly identical results.

Testing an 88 MHz device on sample 3.1 using an Agilent 33250 function generator and an Agilent 54641D oscilloscope resulted in data with periodic amplitude peaks across frequency. While initial calculations showed a strange inverse correlation with predicted values, further testing revealed that the frequency spectrum collected did not change when the probes were lifted off of the SAW device. Additionally, the amplitude of the data was dependant on the distance the raised probes were from each other. This indicated that there was crosstalk between the probes to the extent that effects from the SAW device were negligible.

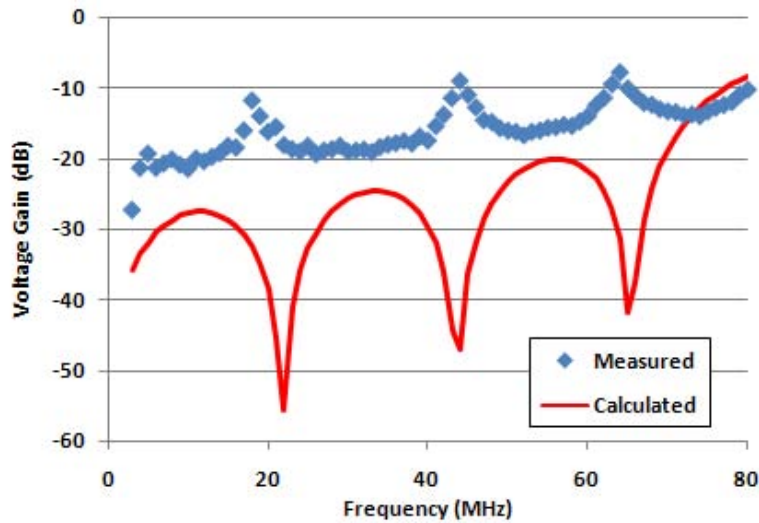


Figure B.9: The frequency spectrum peaks gathered from 3.1 using a function generator and oscilloscope was inversely related to calculated values.

Testing of S_{21} parameters for several devices on sample 3.6 was inconclusive when new probe tips were used on the AFIT probe station. When the probes were contacted to the 87 MHz device, very minor changes were seen in the frequency response near the expected resonance point. Similar results were seen for the 120 MHz device. The 290 MHz device returned the most promising results, as shown in Figure B.10. Additional peaks were observed near the expected resonance peak when the probes contacted the device, but enough other changes were seen in the frequency

spectrum that this was not considered conclusive evidence of SAW activity. Many of the features in the frequency spectrum caused by the cables, connections, and probes could be calibrated out of the data if a calibration substrate had been available or by using connections designed for high frequency operation.

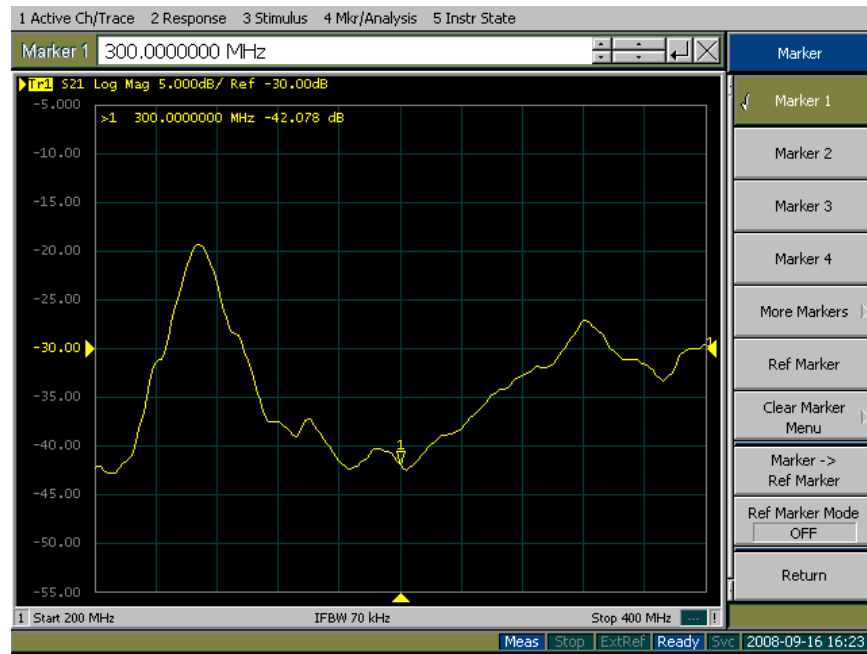
When the input and output ports of the network analyzer were shorted together through BNC to N-type adaptors and a BNC cable, the data taken in Figure B.11 was recorded. The S_{21} value near 0 dB across frequency indicates that a large portion of the signal is transmitted through the adaptors and cabling without distortion. This also indicates that the impedances are closely matched between the network analyzer, adaptors, and cabling.

B.3 Series 3 Testing at AFRL

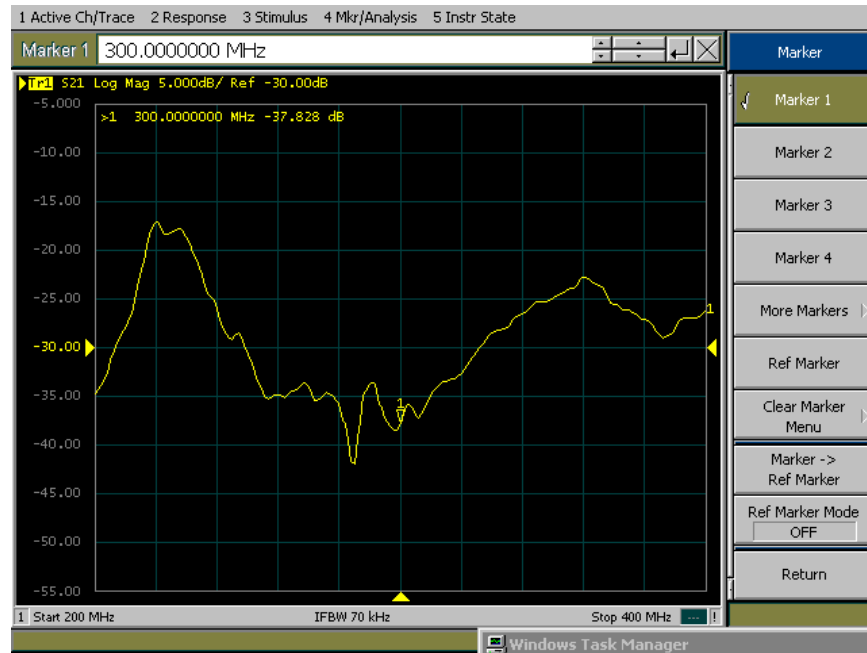
The frequency response measurement was repeated for a different device on Sample 3.6. The data recorded from this test more clearly shows differing frequency spectrums caused by probe movement, as shown in Figure B.12. Peaks are observed at 82.1 MHz and 93.0 MHz, although the main peak was calculated to occur at 87.2 MHz using Equation 2.2 with 10 micron finger widths and spacing. Later examination of the L-Edit file used to manufacture the data revealed several design errors where the spacing between fingers was slightly more than 10 microns. This likely contributed to the lowering of the main lobe.

Finally, tests were performed for the 3 micron device on Sample 3.6. Calculations predict a resonance peak at 290.67 MHz. As seen from Figure B.13, a resonance peak is found at 290.75 MHz. This is within the resolution of a single step in the frequency sweep settings on the network analyzer.

B.3.1 COTS SAW testing. A COTS SAW device was connected to the network analyzer through the BNC to N-type adaptors and a BNC to alligator clip cable. None of the characteristic sinc function shape was seen in the frequency response of the SAW while testing. This indicates that the measurement setup was not sufficient

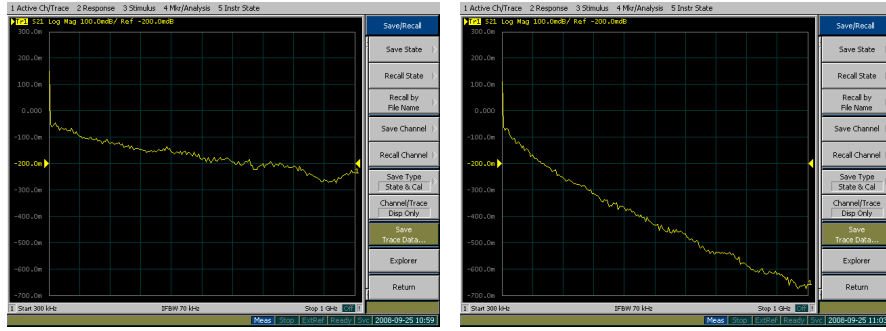


(a)



(b)

Figure B.10: S_{21} testing of 290 MHz device on Sample 3.6. (a) Probes raised above device. (b) Probes in contact with pads.



(a)

(b)

Figure B.11: S_{21} for path including BNC to N-type adaptors and BNC cable (a) 12 inch BNC cable (b) 18 inch BNC cable

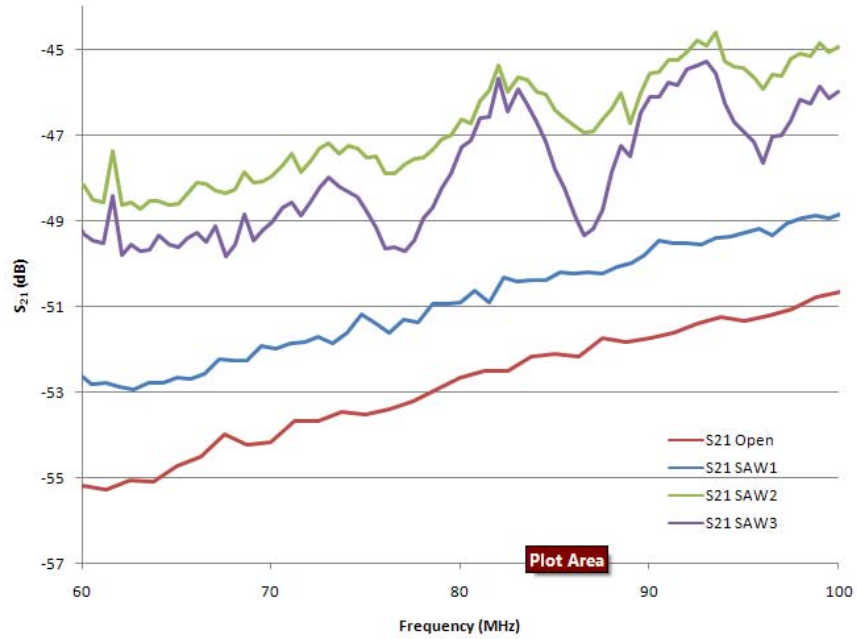


Figure B.12: Frequency spectrum when probes are open and 3 readings of when connected to a 10 micron SAW device on Sample 3.6.

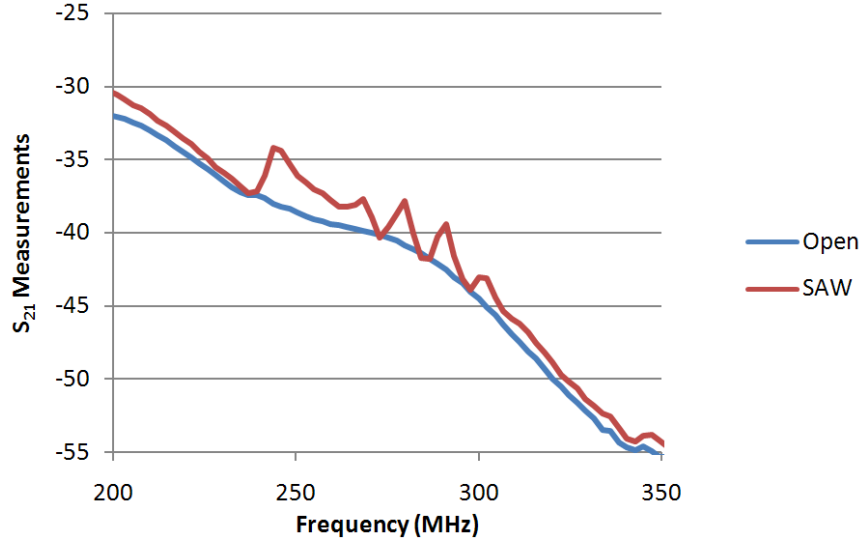


Figure B.13: Frequency spectrum when probes are open and when connected to a 3 micron SAW device on Sample 3.6.

to discern the location of the peak. The recorded data was later found to be unusable, so no figures are available for these tests.

B.4 Second Generation Device Fabrication

B.4.1 Series 4 Fabrication. Lithography of the Series 4 chips using the new mask turned out poorly. First, the smaller critical dimensions and larger device area caused contamination of the wafer surface to have a much greater effect, as shown in Figure B.14. This contamination would carry through the fabrication process to produce electrical shorts between fingers in the final devices. Second, fingers were noticed to be somewhat wavy, which was traced back to the fabrication tolerances of the photomask. Third, significantly more overdevelopment was observed, as shown by the ratio of photoresist developed away to that remaining in the fingers and the rounding of the corners in Figure B.15. This was attributed to the long period of time between fabrication runs. In this period, it is possible that any number of variables could have drifted such as photoresist viscosity, UV bulb intensity, hot plate temperature, room temperature, or humidity. It is also possible that due to smaller critical dimensions the overdevelopment was simply more noticeable. When the development

time was reduced from 30 seconds to 25, the lines widths of photoresist more closely match the spaces between them.

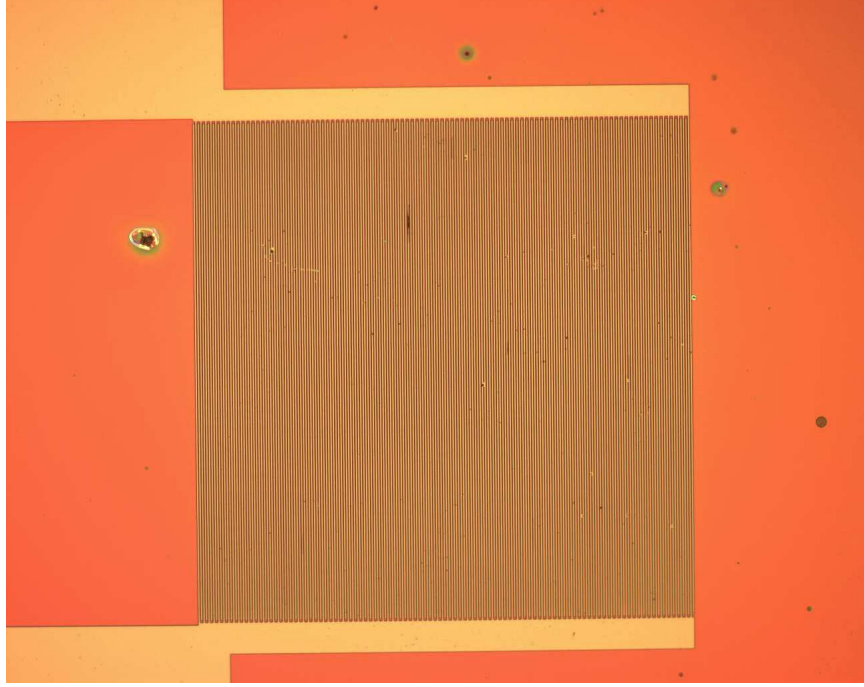


Figure B.14: Sample 4.2 Lithography. Some areas of photoresist developed excellently, but contamination affected fabrication success.

After e-beam metal evaporation onto the samples and subsequent sonication, a variety of results were observed for this series, including areas of bridging, poor adhesion, shorts caused by contamination, and perfect fabrication. Additionally, the results varied significantly across even a single sample, which was attributed to photoresist thickness variations due to working with small chips. On some samples, such as 4.3, the electrical shorts were attempted to be fixed by additional sonication. This worked to some extent, but the longer a sample was in the sonicator, the more fingers were removed. Figures B.16-B.18 show a sampling of the results from this run.

The right IDT of the second device of Sample 4.3 contained a number of shorts, so this was attempted to be burnt out first. The resistance across the IDT was measured to be 25.56Ω . After increasing the voltage to around 6V, the connection between the pad and the fingers burnt out, and the resistance was measured as 4.5

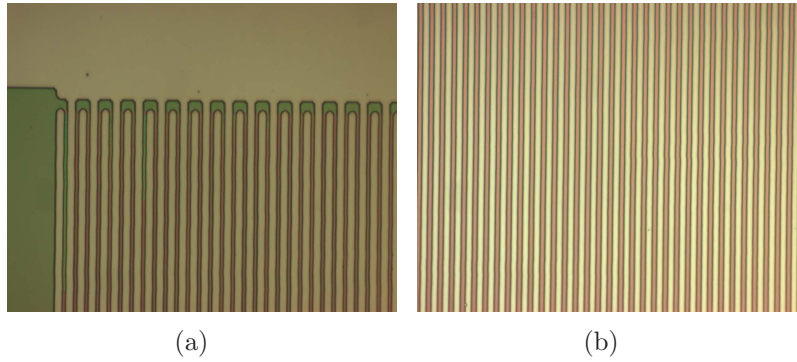


Figure B.15: Series 4 lithography development (a) Sample 4.1 used a 30 second development in LDD26W. Notice overly wide fingers, rounded corners, and wavy lines. (b) By reducing the development time to 25 seconds, a finger-to-photoresist ratio was closer to 1 was observed on Sample 4.4.

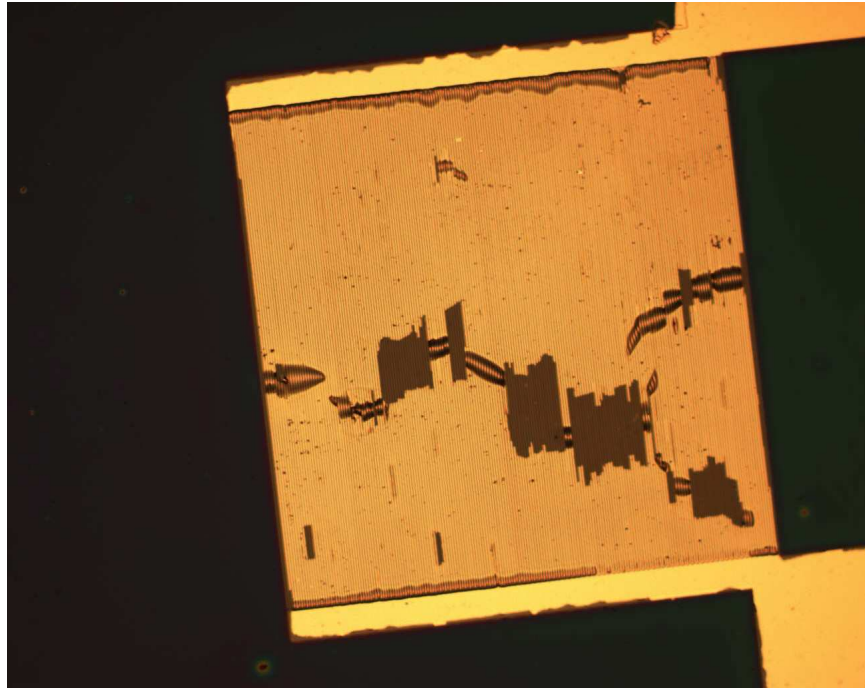


Figure B.16: Sample 4.2 after metal lift-off. Some areas of gold unexpectedly lifted off the substrate.

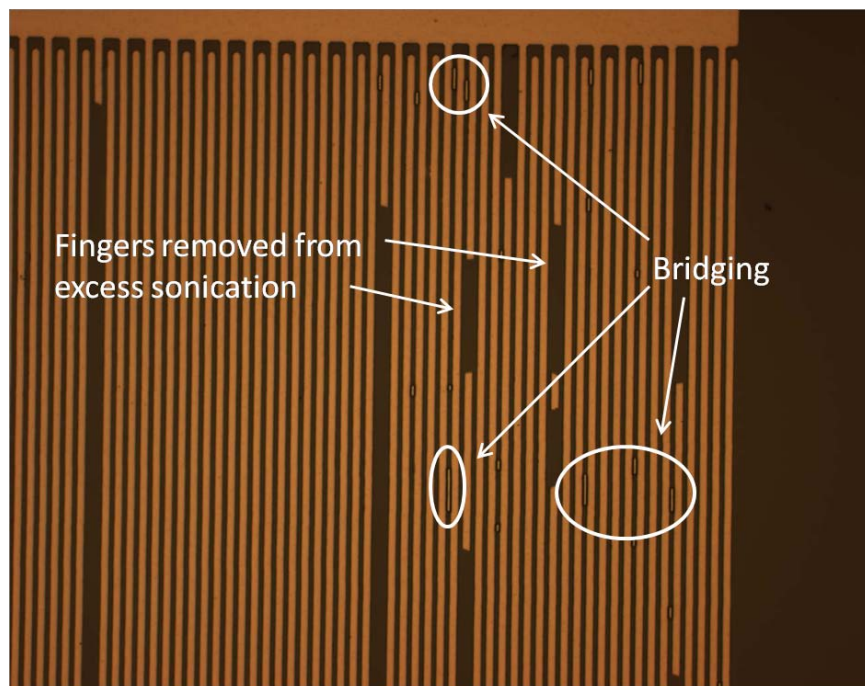


Figure B.17: Sample 4.3 after metal lift-off and 1165 strip. Sonication to reduce bridging removed several fingers.

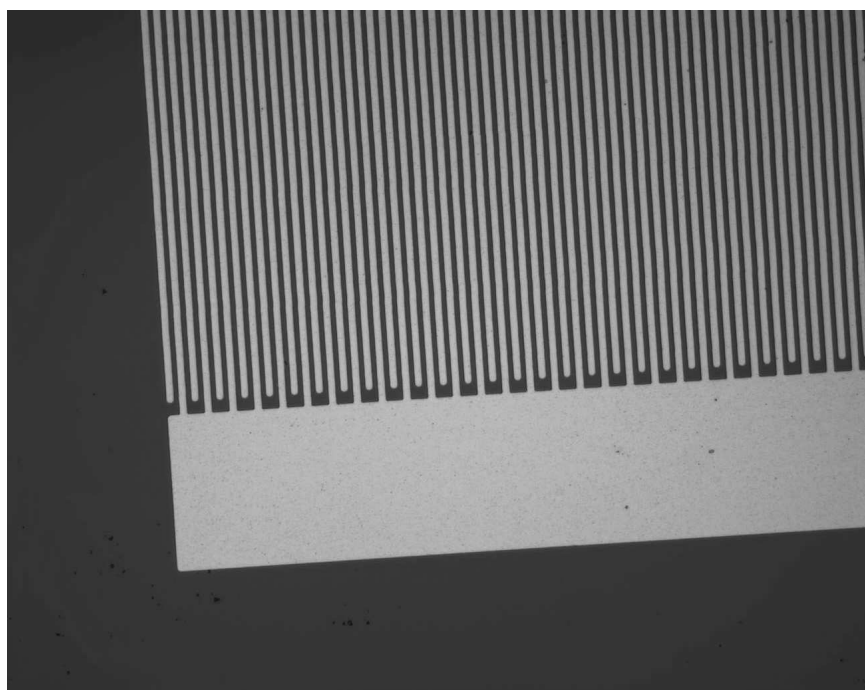


Figure B.18: One of the devices on sample 4.5 after metal lift-off and 1165 strip appeared acceptable.

M Ω . 4.3.2L visually appeared to have fewer shorts in the fingers. It began to discolor around 5 V, and shorted out in the same location as 4.3.2R at 7 V, as shown in Figure B.19. Similar results were obtained for 4.3.1L.

The strange discoloration observed during chip burnout of Series 4 prompted additional research in which it was discovered that a gold/aluminum interface produces intermetallic compounds that degrade performance [52]. This reduces conductivity significantly, so a work around was necessary to continue using the novel layered electrode structure.

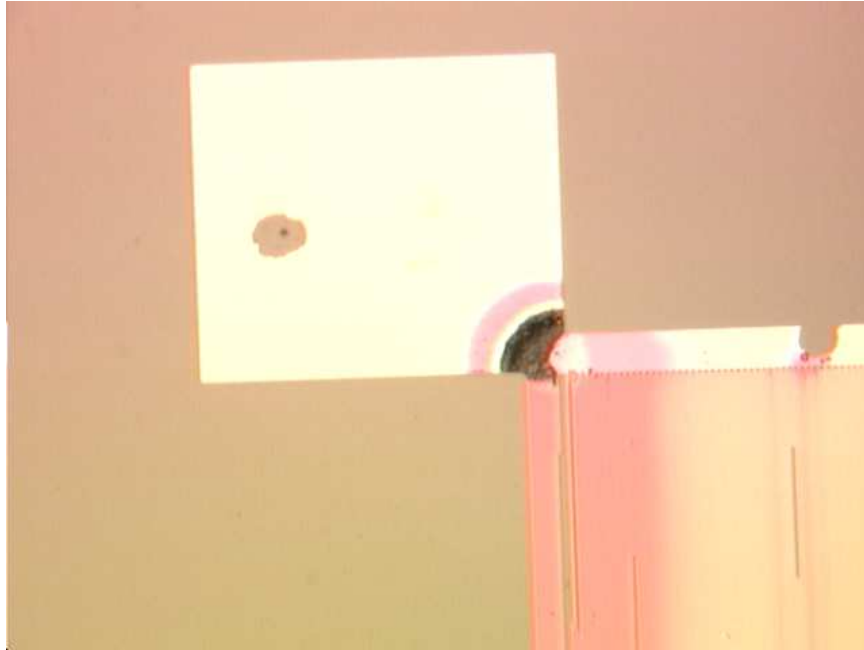


Figure B.19: Device 4.3.2 burnt out at the pad, not the shorts in the fingers. Note the discoloration of the metal.

Series 4 wafers were later used to test the fabrication of thicker bond pads. The lithography alignment was off several microns on most samples, but this was judged to be acceptable given the size of the bond pads. Spots of photoresist that remained after development were observed, as shown in Figure B.20.

After metallization and lift-off, the metal did not appear smooth even on the bond pads. This was likely due to the spots of photoresist that remained after development. The corners of the pads also tended to have “wings” where metal was

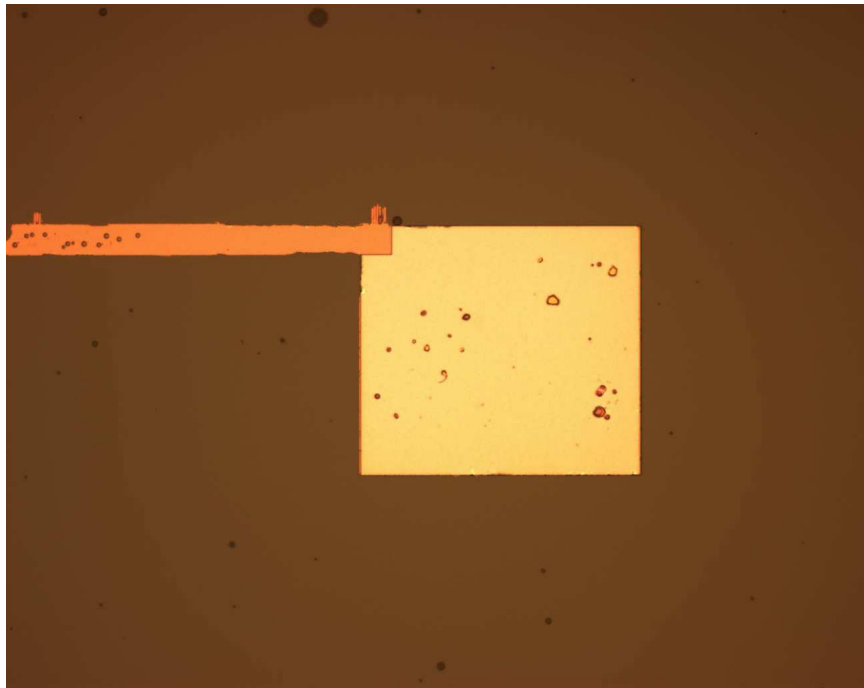


Figure B.20: Device 4.1 had spots of photoresist remaining after development.

still attached that should not have been. It is possible that this was due to pulling the metal off with tweezers rather than sonication. Figure B.21 shows an example of these effects.

Wire bonding the Series 4 chips after application of the 5000 Å bond pads was not successful. A variety of settings were attempted with the wire bonder. Those with low force and power tended to make a small hole in the bond pad, as shown in Figure B.22. Higher powers and forces closer to the recommended values would either partially or fully remove the pad from the substrate, as shown in Figure B.23. When removed, it was apparent that some of the metal from the original layer remained. This indicates that the bond is successfully being created at higher powers, but either the gold layer or layer interface strength is not sufficient to prevent delamination.

B.4.2 Series 5 Fabrication. The new cleaning procedure using cotton swabs in acetone worked well for Series 5. The contamination was almost completely removed. This contributed to a higher probability of success during the subsequent

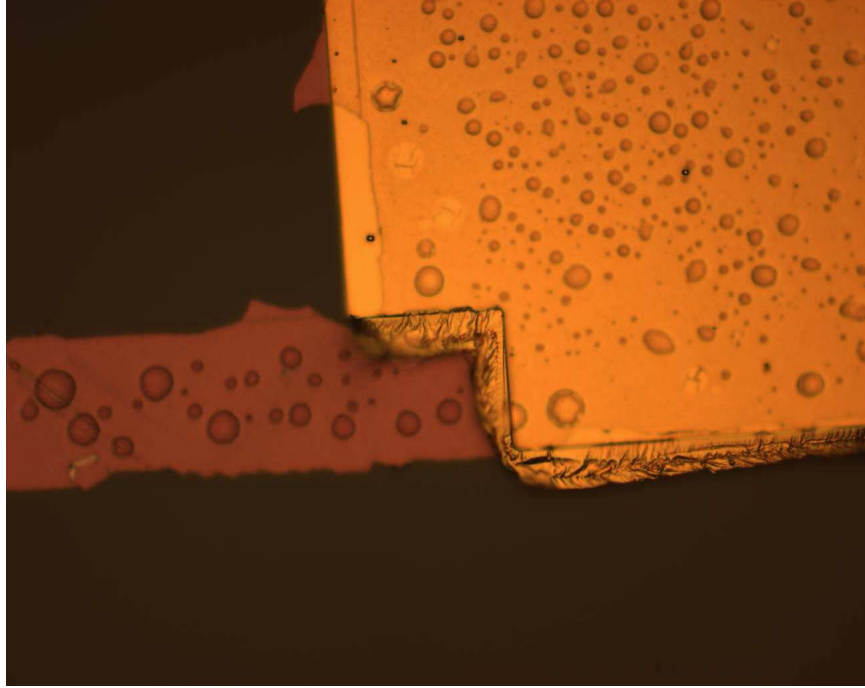


Figure B.21: Device 4.5.1 shows both a bumpy surface and metal “wings.”

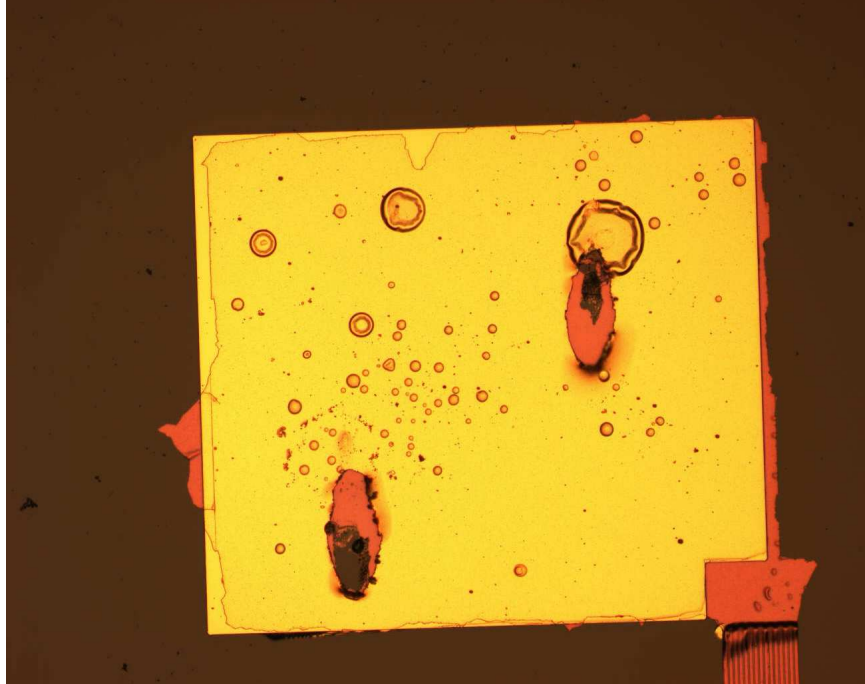


Figure B.22: Device 4.2 shows holes from low-power wire-bonding attempts.

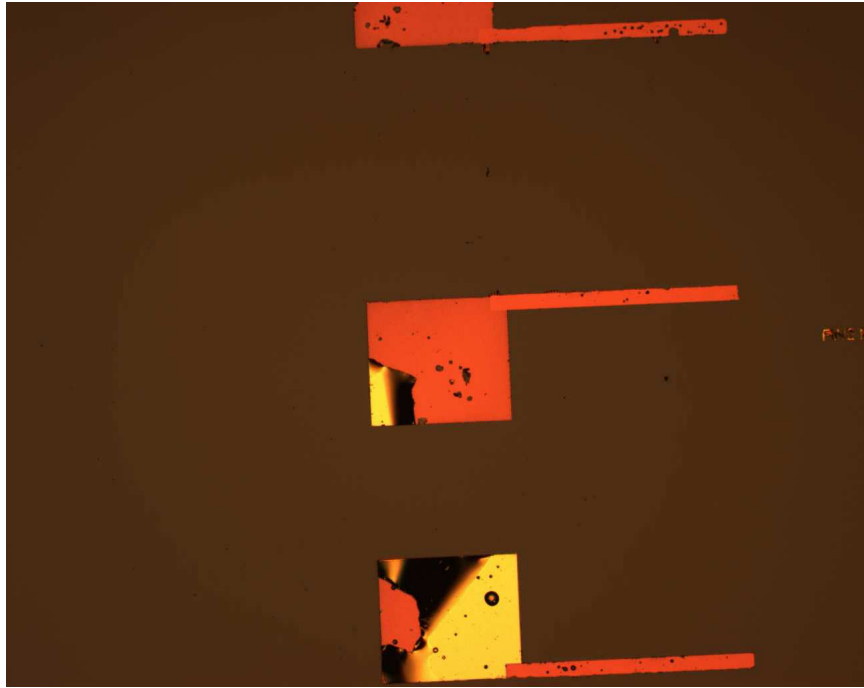


Figure B.23: Device 4.1 shows varying degrees of pad pull-off from wire-bonding attempts.

lithography steps. During the lithography, some excellent looking devices were made, although a few areas with imperfections were still apparent. Several examples are shown in Figures B.24 - B.26. Also, Samples 5.3 and 5.4, the chips which used a double LOR3A layer, both failed due to immature development of that process. It is possible that the devices were underexposed.

After metallization, it was found that the 100 \AA nickel layer preventing inter-metallics from forming was accidentally deposited as titanium. Many of the devices had features were either bridged together or completely gone, as shown in Figure B.27. Where the metal had not remained, the profilometer was able to measure the remaining LOR3A layer to be around $0.8\text{-}1.1 \text{ }\mu\text{m}$ thick. This measurement is likely lower than the actual thickness since some may have come off in the acetone. After stripping in 1165, the metal layer was measured to be $0.6\text{-}0.8 \text{ }\mu\text{m}$ thick. Although the profilometer readings suggest that most of the devices should have lifted off correctly,

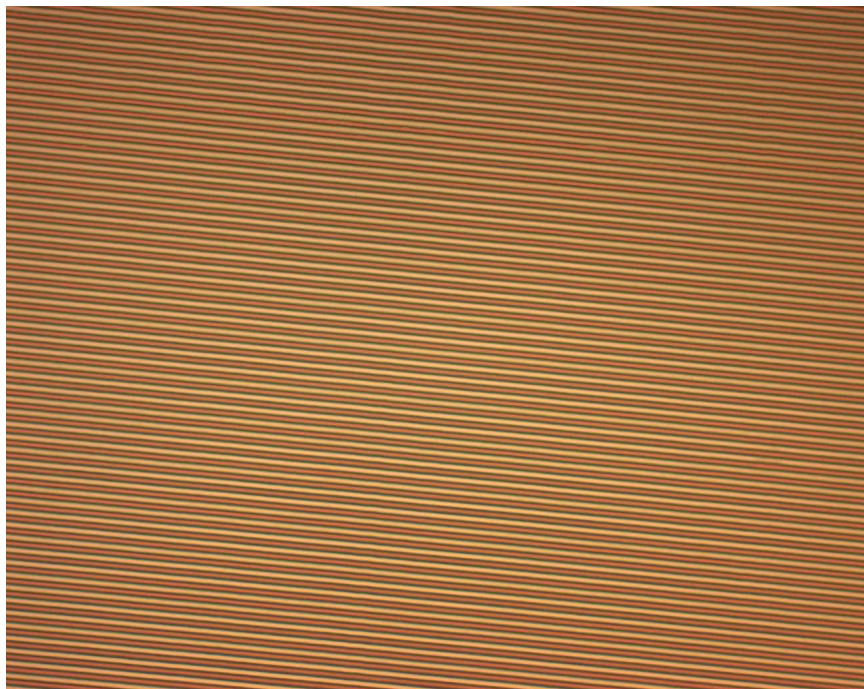


Figure B.24: Sample 5.1 shows excellent lithography on several devices.

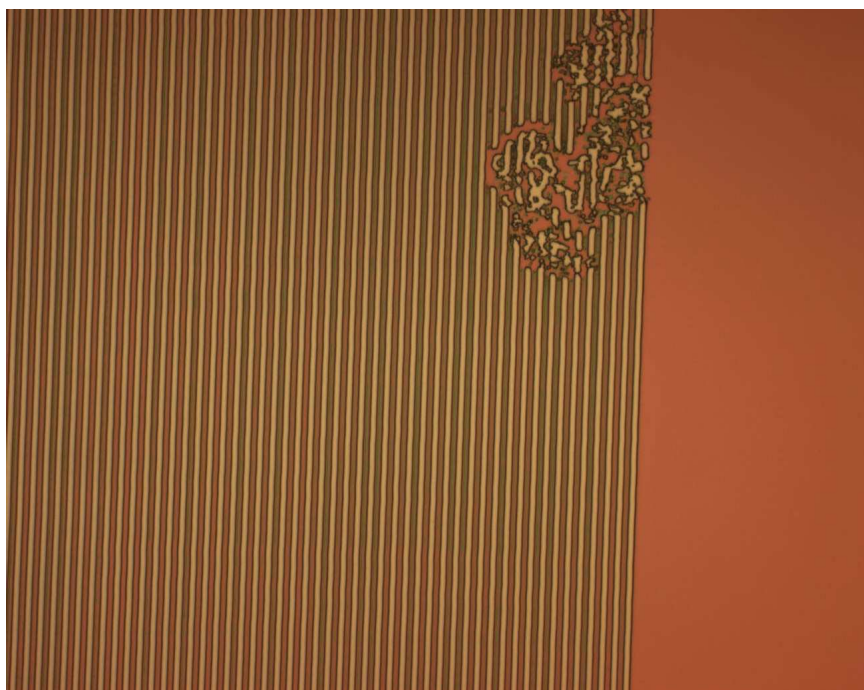


Figure B.25: Sample 5.5 shows area defect possibly caused by mask contamination.

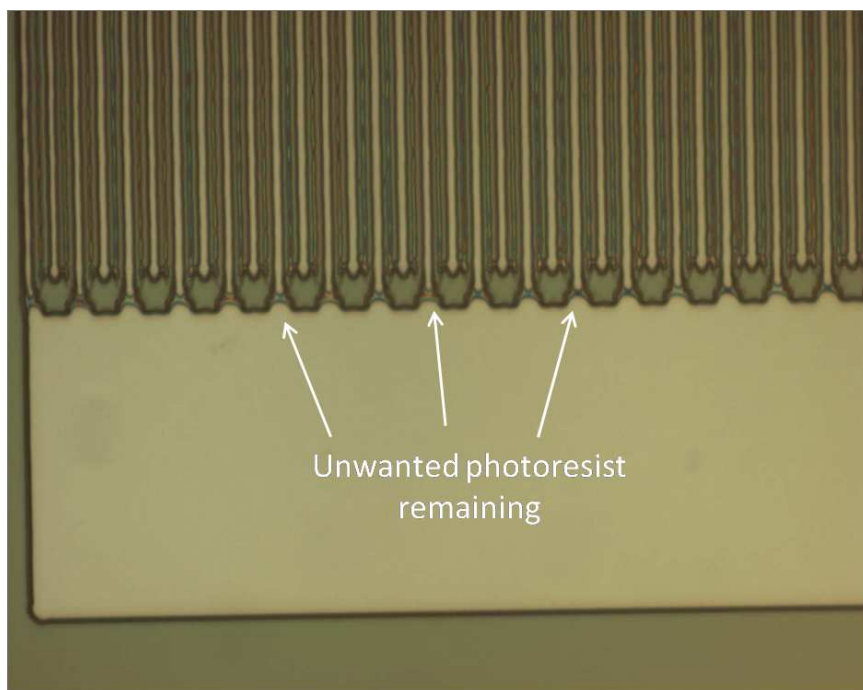


Figure B.26: The fingers of Sample 5.4 with 2 LOR layers did not fully develop out.

this process was still not working correctly. For this reason, subsequent lithography was attempted with double LOR layers.

The best looking chip was Sample 5.5, which was larger than the others. This was attributed to more consistent photoresist application in the center of wafers. This wafer had several perfect IDTs, while those not perfect generally only had a single defect, as shown in Figure B.27. Even with a well-cleaned surface, it appears that statistically the chance of a single particle landing on one of the two IDTs was fairly high due to the greatly increased surface area of the new design.

B.4.3 Series 6 Fabrication. Wafers 6.1-6.4 were fabricated using a double LOR3A layer and an 1818 layer. It was found that if the first development time was set to 70 seconds, the lithography turned out well. Examples from this process development are shown in Figure B.28.

Samples 6.5-6.7 used a LOR3A layer spun at 2000 rpm and an 1805 layer, requiring different development, which produced excellent results. Two examples

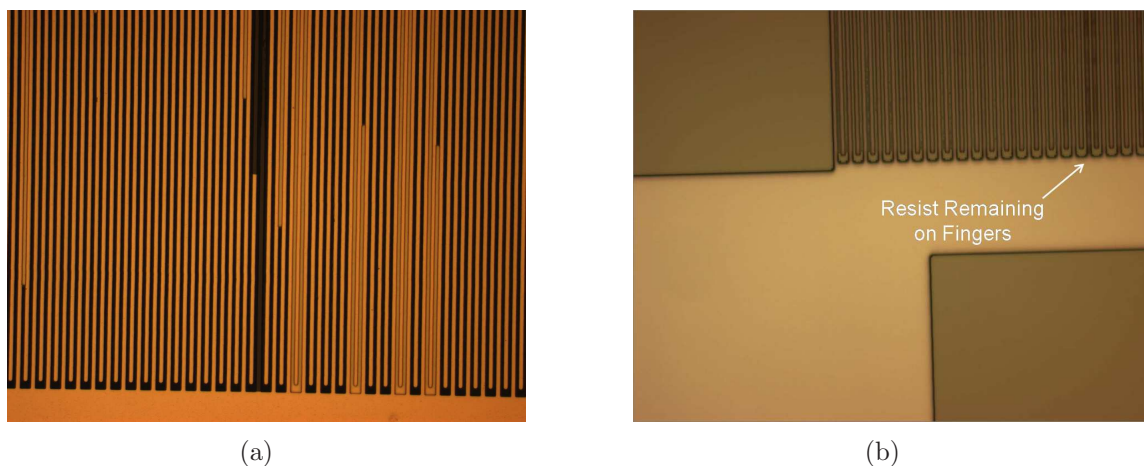


Figure B.27: Series 5 metal lift-off (a) Sample 5.1 showing bridging and missing fingers. (b) Sample 5.5 resulted in nearly perfect devices.

from 6.7 are shown in Figure B.29, including a defect type found to occur occasionally without a clear cause.

After metallization and metal lift-off, Series 6 devices were examined visually for defects. Samples 6.1 and 6.2, the samples that had been plasma ashed for 2 minutes after lithography, both displayed significant amounts of bridging and some finger removal as shown in Figure B.30a. Acceptable devices were found on 6.3.2, 6.3.3, 6.4.4, with the others from 6.3 and 6.4 having minor defects from contamination during lithography, as shown in Figure ???. It appeared on some devices that the metal had been torn off where it should have stayed. This may have been a result of lift-off using tweezers. Samples 6.5-6.7 also had major difficulties with bridging and missing metal as shown in Figure B.30b. This showed that 2000 rpm was too slow to permit consistent coatings, which resulted in poor devices.

Bond pad lithography proceeded with Series 6 wafers, along with the one usable sample from Series 5. A few minor misalignments were observed but fell into the acceptable range, as shown in Figure B.31. After 7500 Å metallization and lift-off, areas of low adhesion where the metal had “bubbled” out from the surface were observed on some of the pads, as shown in Figure B.32. This was likely due to incomplete development. At least four devices appeared functional at this stage,

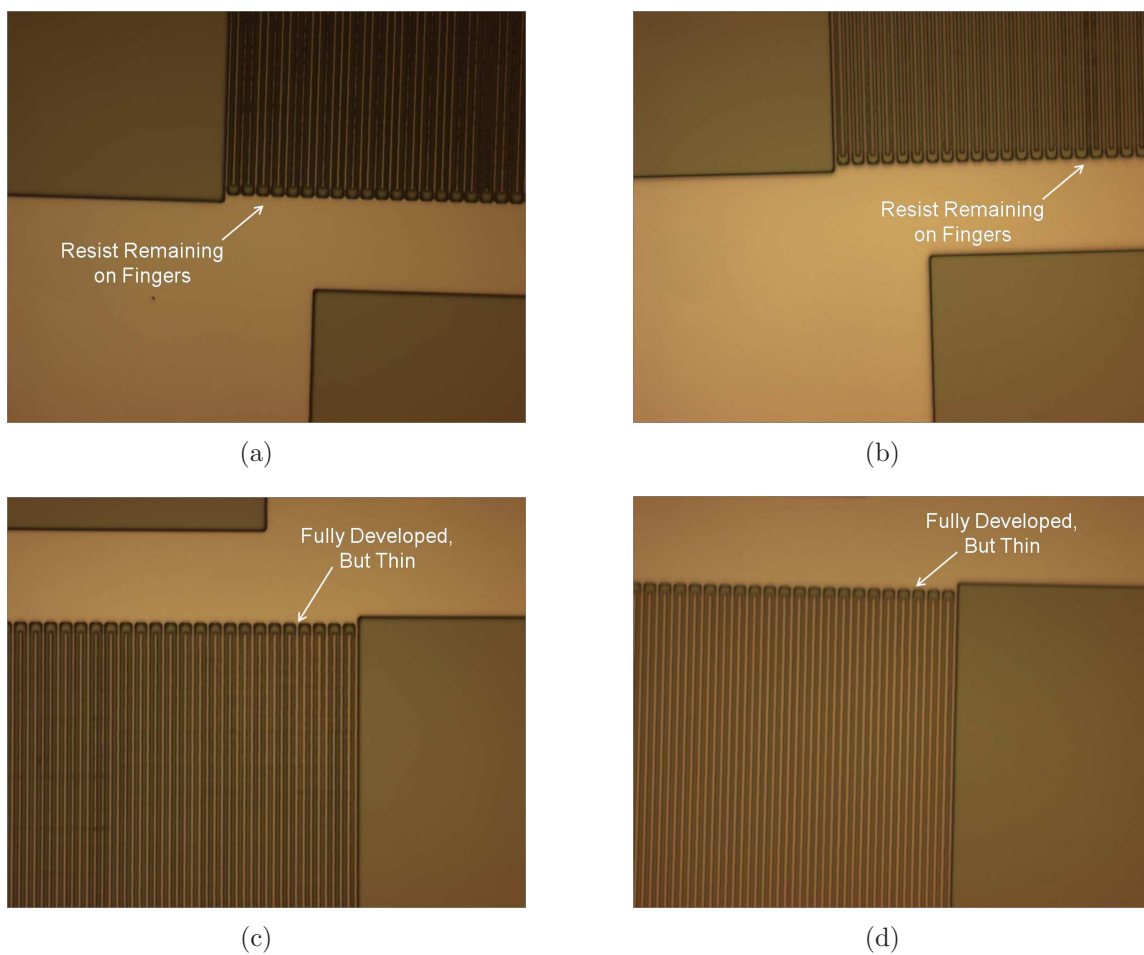


Figure B.28: Series 6 Double LOR3A lithography development (a) Sample 6.1 after 65 second develop. (b) Sample 6.1 after 75 second total develop. (c) Sample 6.1 after 80 second total develop. (d) Sample 6.3 after 70 second develop.

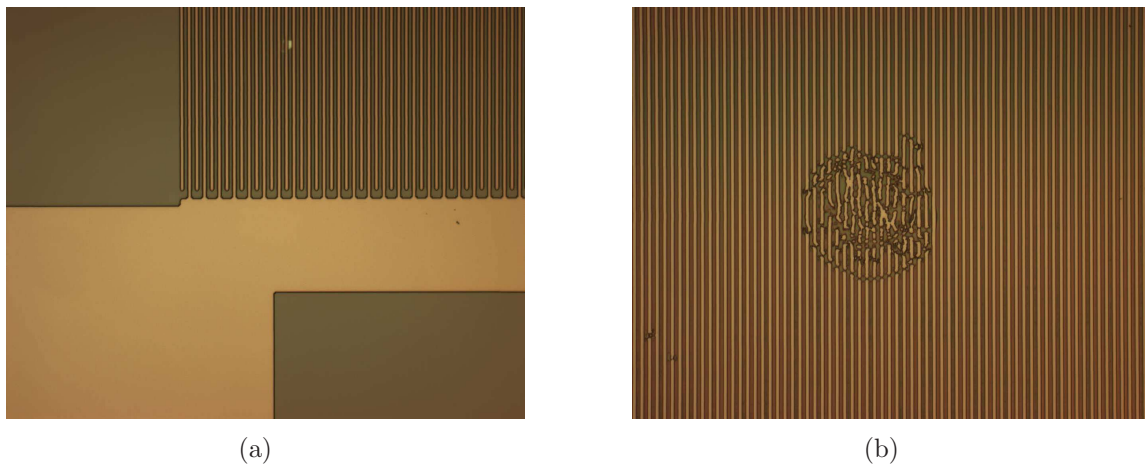


Figure B.29: Series 6 Single LOR3A lithography development (a) Sample 6.7 after 22 second develop. (b) Example of circular defect from Sample 6.7.

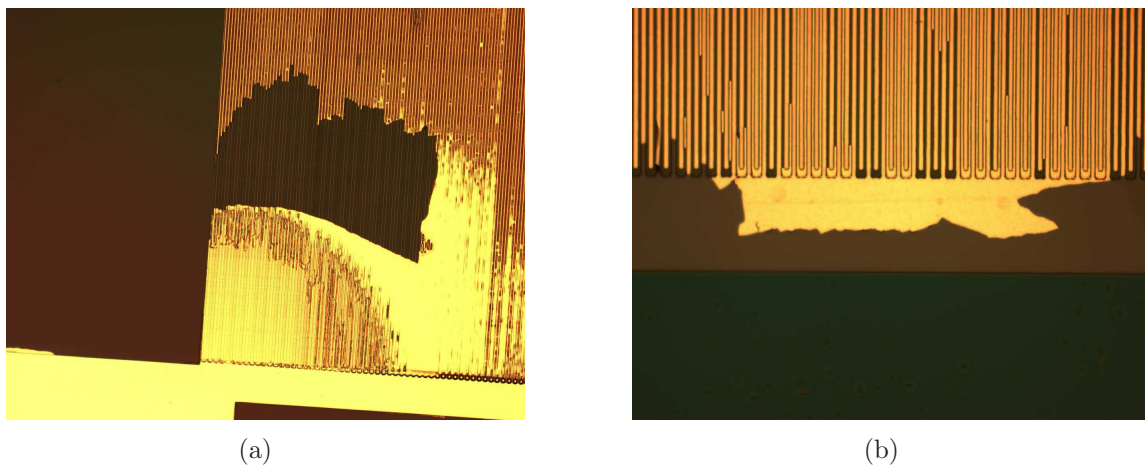


Figure B.30: Series 6 metal lift-off showing bridging and missing metal (a) Sample 6.1 (b) Sample 6.6.

with several more possible successful devices. Figure B.33 shows multiple views of successful IDTs.

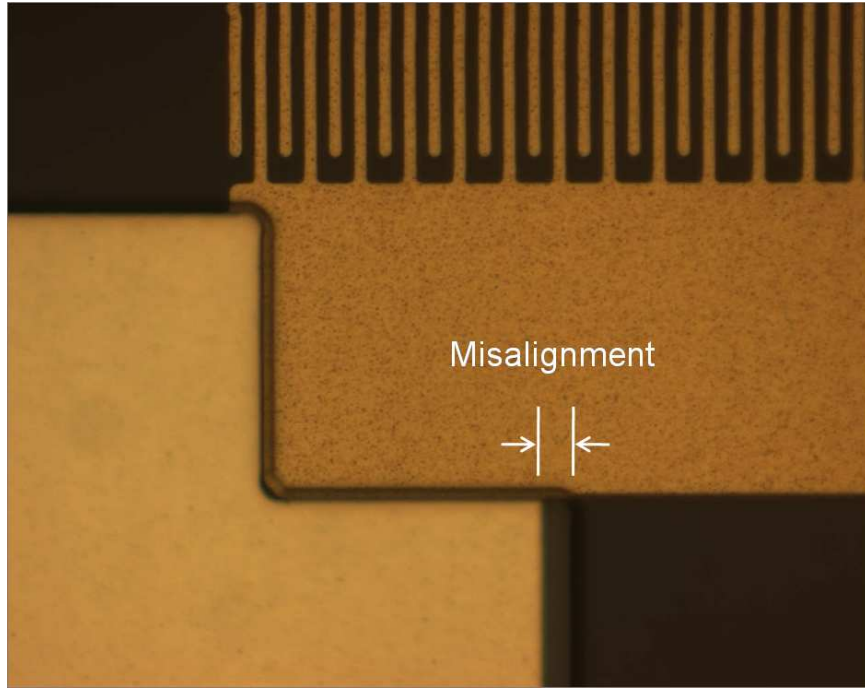


Figure B.31: Sample 6.2 bond pad lithography shows misalignment.

Wire bonding to the thick bond pads was attempted with Samples 6.2 and 6.7. These chips did not have acceptable devices, but the bond pads looked excellent, allowing testing with the wire bonder without risking good devices. Low power and force bonds, even with long bond times, created small holes in the bond pad, not resulting in successful bonds. Bonds created with larger force pulled the pad off the substrate, even after increasing the size of the loop parameter. All of the bond settings attempted on devices were successful when applied to the thicker gold on the chip carrier.

B.4.4 Series 7 Fabrication. After the development step of 7.1, it was found that a portion of the photoresist fingers had completely come off of the substrate. Developing the photoresist for 7.2 and 7.3 by immersion only resulted in better photoresist adhesion. Several acceptable patterns were observed using this method, although

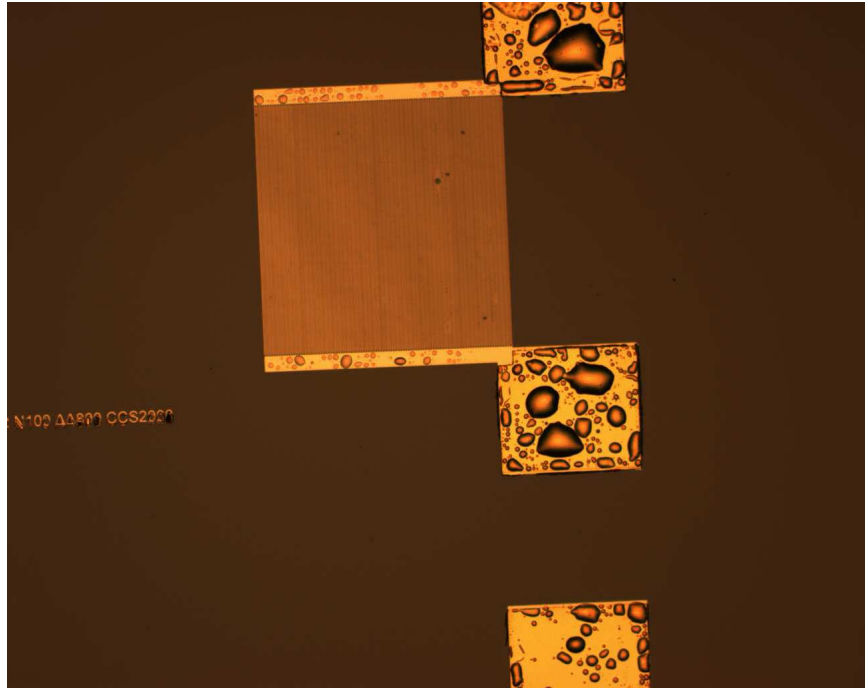
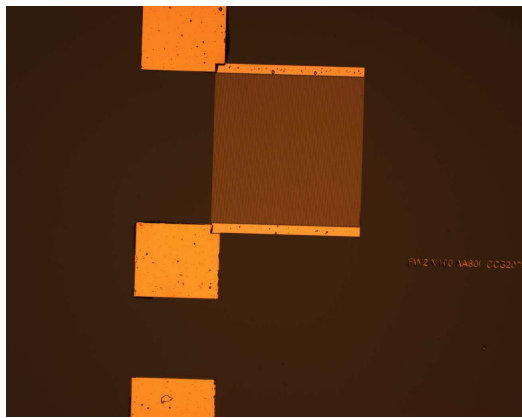
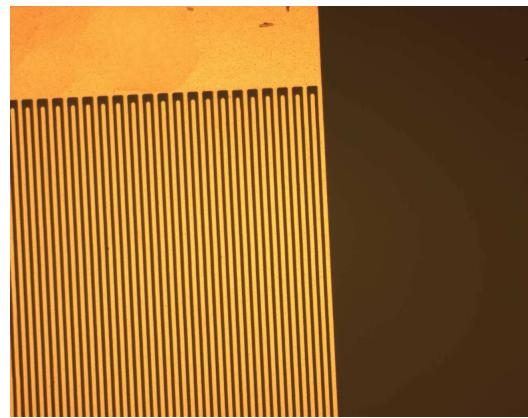


Figure B.32: Sample 6.3 with thickened bond pad metal. Notice the bubbly texture to the gold.



(a)



(b)

Figure B.33: Series 5 and 6 successful bondpad deposition (a) Sample 5.5.1L (b) Sample 6.4.1L shows undamaged fingers after bondpad fabrication.

defects were also observed on some devices. Several examples from these chips are shown in Figure B.34

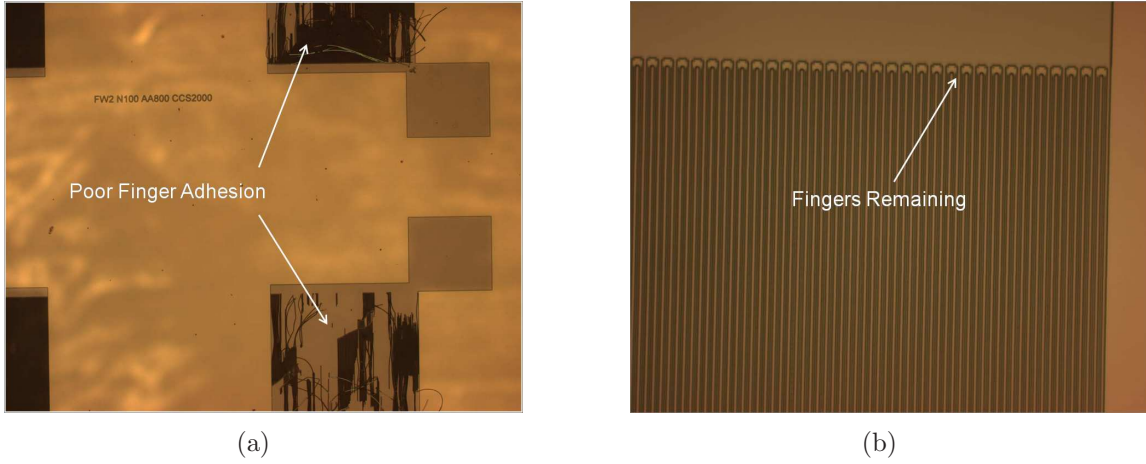
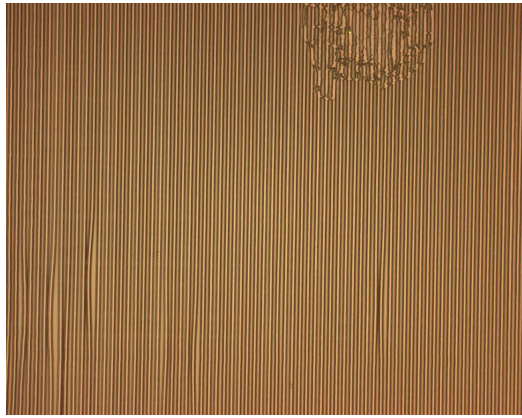


Figure B.34: Series 7 Quartz Lithography (a) Sample 7.1 after development on spinner. (b) Device 7.3.2 after development by immersion.

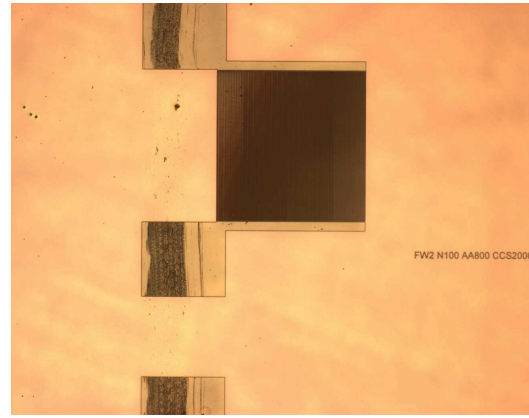
Samples 7.4 and 7.5, the chips that used the HDMS adhesion layer, did not have as many difficulties during development, indicating that it helped photoresist adhesion. A number of devices showed apparently good lithography, although some contamination was observed on the bond pads. This may be attributed to remaining HDMS that did not have sufficient time to develop. Examples from 7.4 and 7.5 are shown in Figure B.35.

Series 7 wafers displayed poor results after metal lift-off. The gold was almost completely removed from the majority of devices, while the remaining devices had a large proportion of bridged fingers. This was attributed to the poor adhesion of metal to quartz. No usable devices were fabricated. A sample of these devices are shown in Figure B.36.

B.4.5 Series 8 Fabrication. Since the openings in the mask for bond pad lithography were not in the center of the mask and there were no previous markings on the chips to align to, it was difficult to align the bond pads with the center of the samples. For instance, only half of the pads on Sample 8.1 were found on the

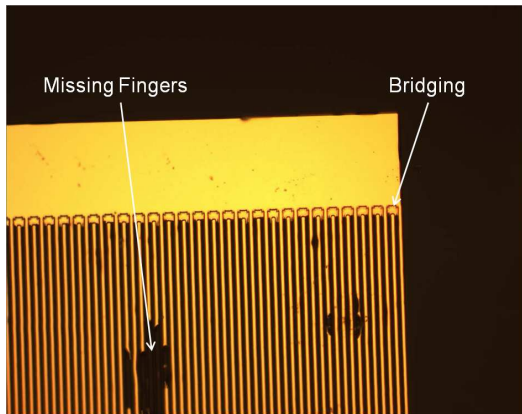


(a)

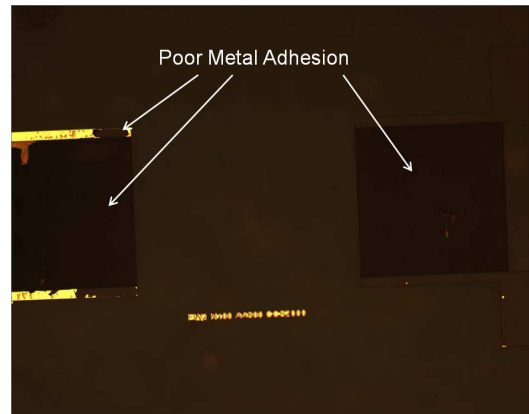


(b)

Figure B.35: Series 7 Quartz Lithography with HDMS (a) Device 7.4.4 showing wavy photoresist and a possible terminal defect after development on spinner (b) Sample 7.5.2 showing acceptable IDT and contaminated pads.



(a)



(b)

Figure B.36: Series 7 Metal Lift-off (a) Left IDT of Device 7.1.2 (b) Most of the metal from device 7.5.2 was removed.

substrate. This problem was corrected for in subsequent chips. These chips displayed similar patterns of residual undeveloped photoresist which were traced back to mask contamination, as shown in Figure B.37. No further processing was done with this series beyond lithography.

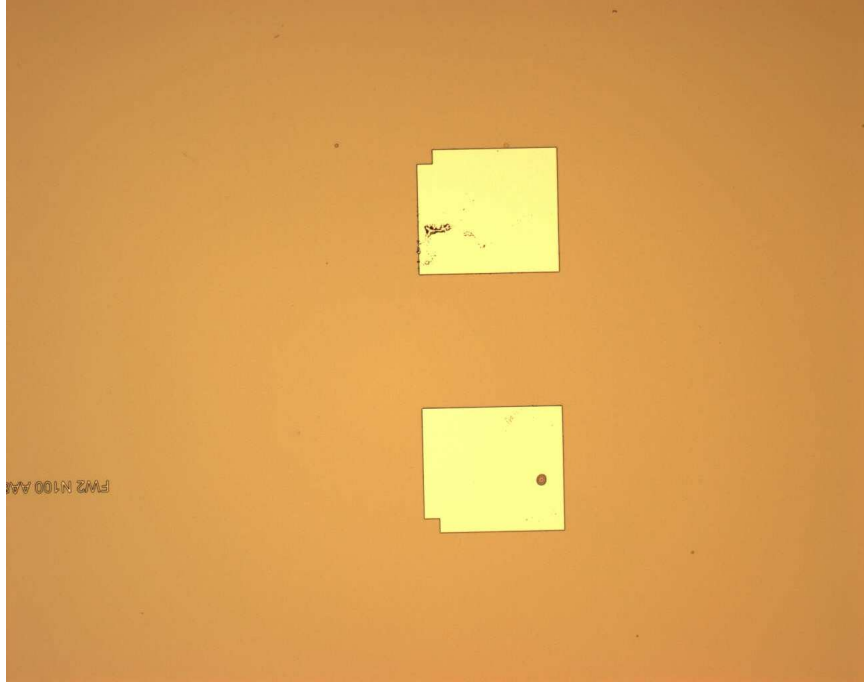


Figure B.37: Sample 8.4 Lithography.

B.4.6 Series 9 Fabrication. The newly diced Y-Z lithium niobate wafer was extremely clean to the point where it was difficult to focus the microscope on the surface of the chip after spray cleaning. Samples 9.1 and 9.2 both showed poor photoresist development around the finger connections to the main arm, as shown in Figure B.38. Even after significant overdevelopment, there was still photoresist remaining at the base of the fingers, indicating localized underexposure. This led to subsequent exposure using a new mask site. Sample 9.3 was dropped during lithography, but 9.4 - 9.6 did not display the earlier difficulties with poor finger connections. Sample 9.4 appeared slightly underdeveloped after 22 seconds, possibly due to exposure closer to the edge of the mask where light intensity was slightly lower. Sample 9.5 displayed a line of discontinuity in the photoresist that was later found to be a

hairline fracture in the substrate. Defects due to contamination on the wafer surface were significantly reduced. Several pictures from 9.4 - 9.6 are shown in Figure B.39.

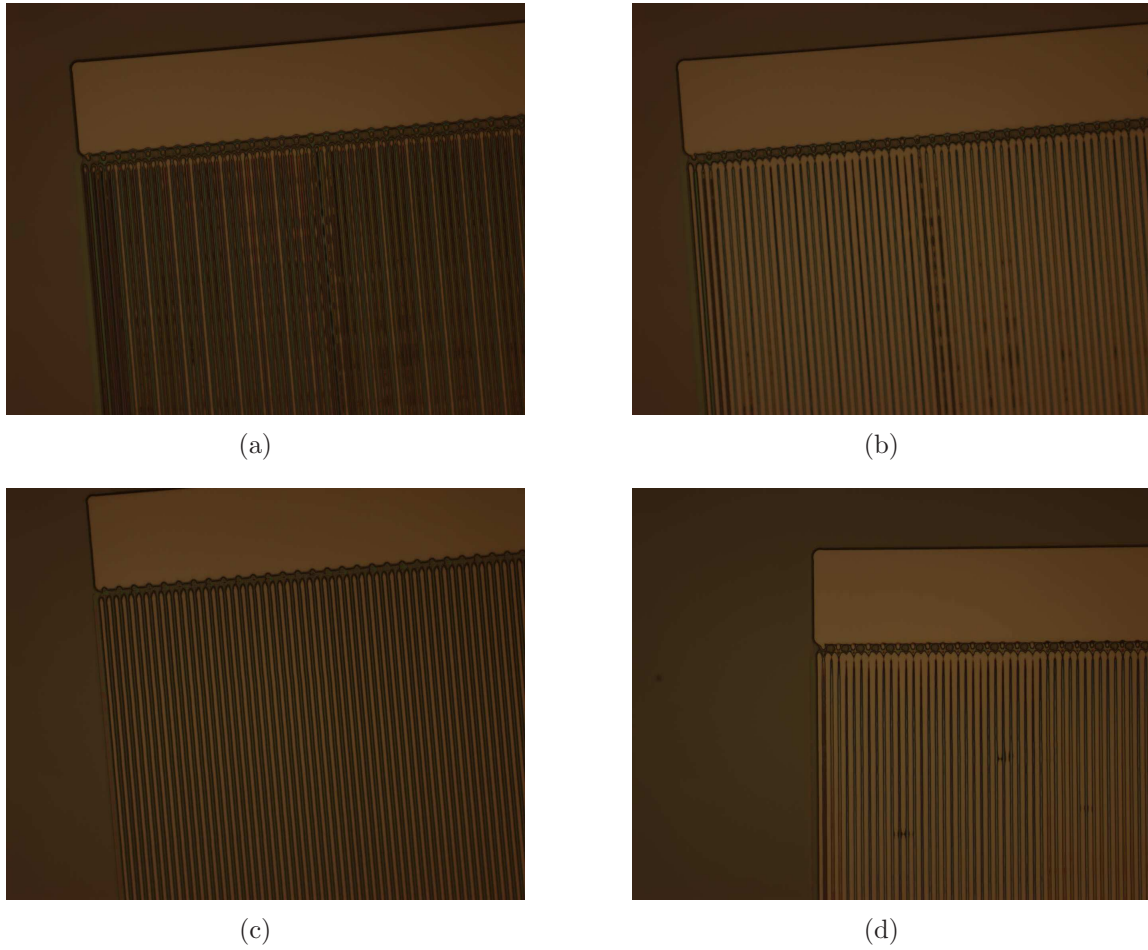
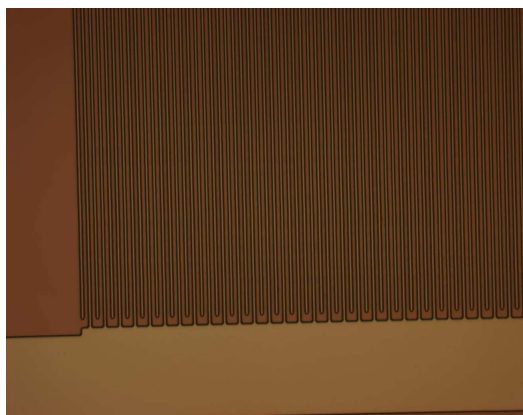
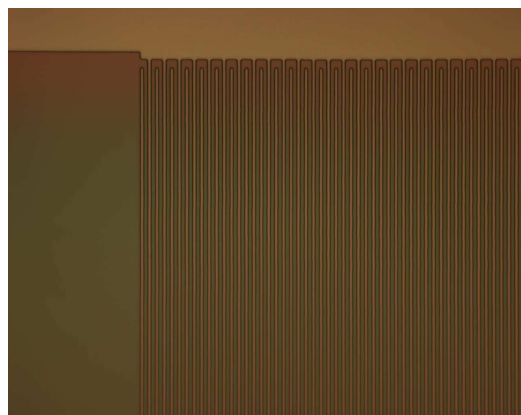


Figure B.38: 9.1 and 9.2 Lithography (a) 9.1.2 after 27 second develop (b) 9.1.2 after 32 second develop (c) 9.1.3 after 27 second develop (d) 9.2.3 after 28 second develop

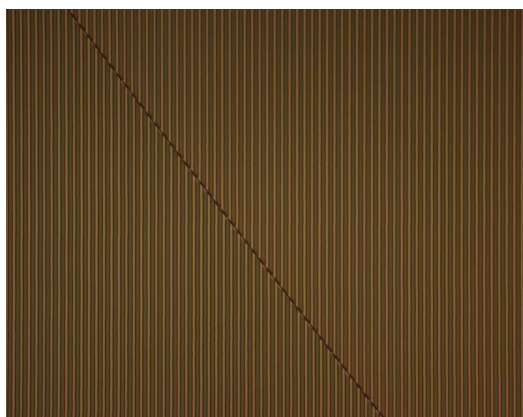
As expected from the lithography step, 9.1 and 9.2 appeared unusable after metallization. 9.4 initially showed significant bridging after the first 15 second sonication. Some of this was able to be removed by an additional 45 second sonication, but other areas of the chip still had bridging after as long as 6 minutes of sonication. Additionally, the long sonication time began to remove good fingers in some areas of the chip. Sample 9.5 broke along the hairline fracture when placed into the sonicator. Occasional bridging occurred that could not be removed by sonication, but several



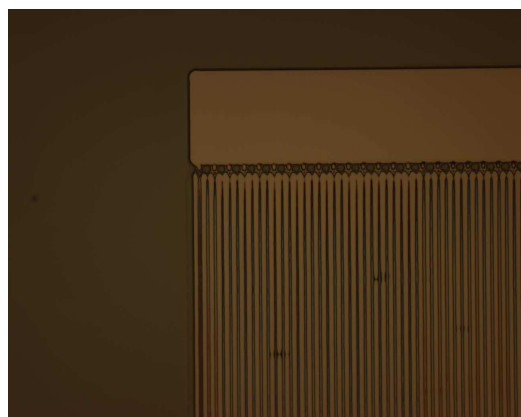
(a)



(b)



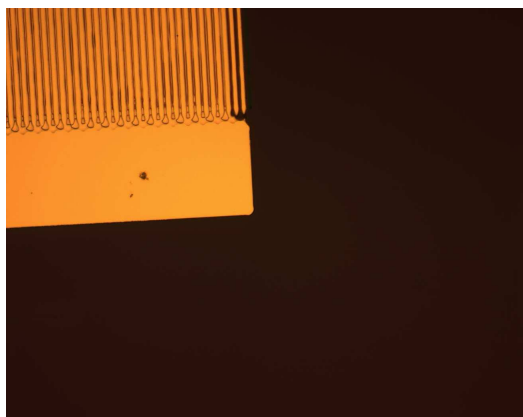
(c)



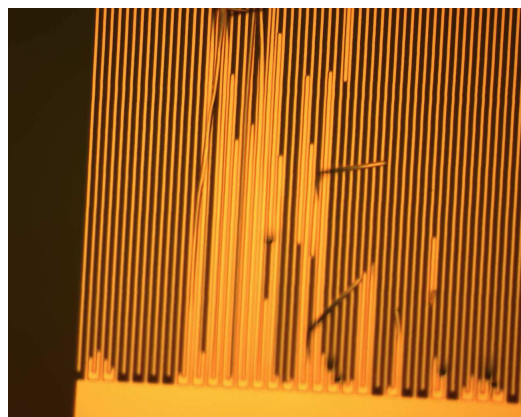
(d)

Figure B.39: 9.4 - 9.6 Lithography (a) 9.4.1 after 22 second development showing slight underdevelopment (b) 9.5.1 (c) 9.5.2 with hairline crack (d) 9.6.1 shows one of the chip's few nonterminal defects

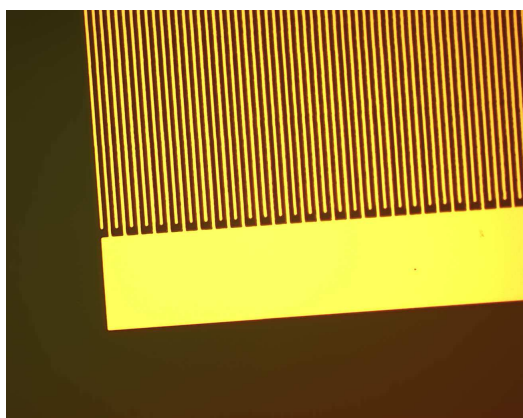
devices would have turned out perfectly if the wafer had not been broken. Sample 9.6 turned out several devices with bridging and finger removal. This was unexpected due to the apparently good lithography observed on this wafer before metal evaporation. Figure B.40 contains samples from Series 9 after metal evaporation.



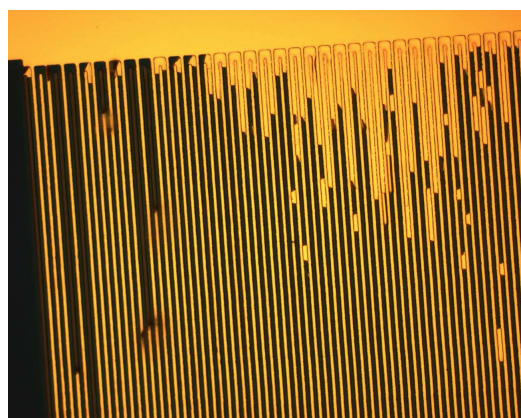
(a)



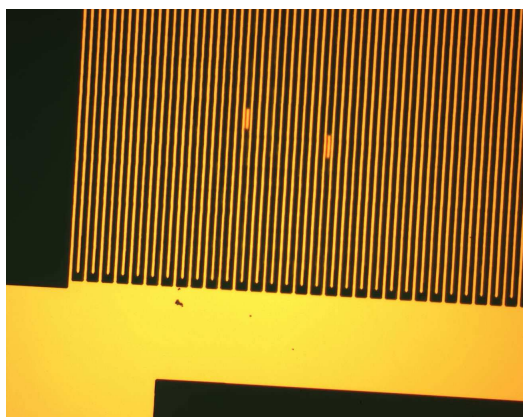
(b)



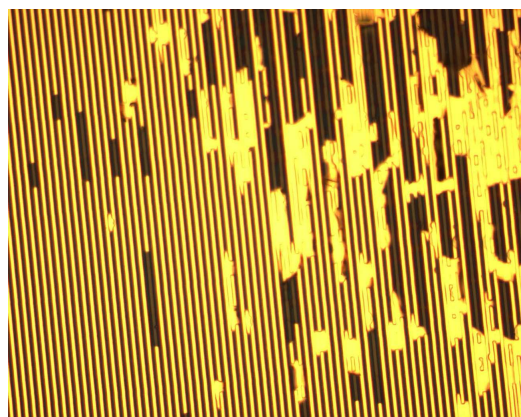
(c)



(d)



(e)



(f)

Figure B.40: Series 9 metal lift-off and corresponding sonication times (a) Device 9.2.3 after acetone soak only (b) 9.4.2R after 15 seconds (c) 9.4.2R after 6 minutes (d) 9.4.2L after 6 minutes (e) 9.5.3 after 3 minutes (f) 9.6.1 after 1 minute.

B.4.7 Series 10 Fabrication. Series 10 lithography produced mixed results. Sample 10.1 showed excellent lithography on all of the output IDTs, but the corresponding input IDTs were completely unusable. This could have been a result of uneven photoresist dispersal across the wafer surface. The photoresist between the fingers of Sample 10.2 was all removed during development. This was traced to a plastic holder left on the stage during exposure, which prevented the mask from coming fully in contact with the chip. Sample 10.3 turned out similar to 10.1 in that exactly half of the chip produced good patterns. In this case however, the top half was usable, resulting in two devices that looked excellent. Sample 10.4 appeared underexposed or over baked due to remaining photoresist within the patterned area after a 3 minute total development. 10.5 was exposed for 2.5 seconds initially by accident. This was immediately corrected before moving the chip from the machine, but the second exposure was misaligned by approximately 20 microns. The results from 10.6 varied widely across the chip and with development time, but the best devices appeared to be from 60 second exposures. These results are found in Figure B.41

B.5 Testing Newly Designed Devices

B.5.1 Calibration with MMR Probe Station. Before testing, calibration was attempted using the calibration substrate ordered from the Micromanipulator Company. After through calibration, S_{21} measurements with the signal probes shorted through the same pad and grounds touching returned readings 50 dB too high. These results remain unexplained. A similar calibration by shorting the signals and grounds together on different pads was used, which had a significantly shorter through path. The S_{21} measurements of Device 6.4.1 using both calibrated and uncalibrated data are shown in Figure B.42. When the predicted peak was later calculated to check the measurements, it was found to be outside the range of measurements taken.

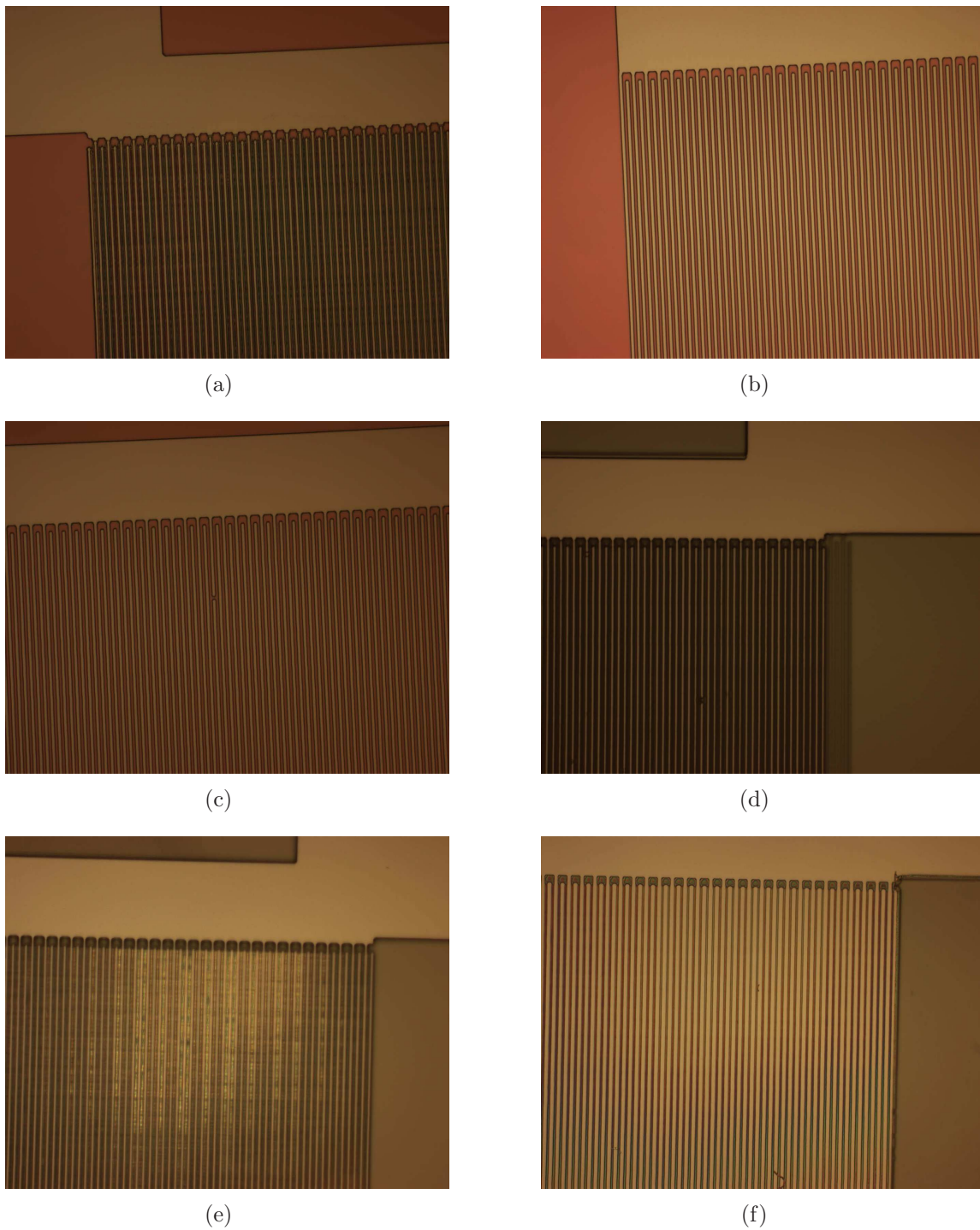


Figure B.41: Series 10 Lithography (a) Left IDT of 10.1.1 (b) Right IDT of 10.1.1 (c) 10.3.1 shows acceptable results (d) 10.5.2 shows inconsistent alignment for multiple exposures (e) 10.6.1 after 60 second development (f) 10.6.1 after 70 second development.

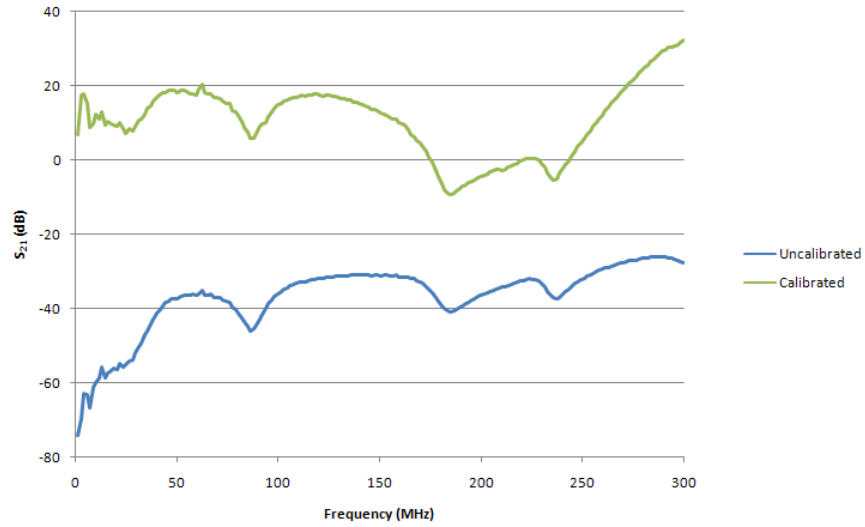


Figure B.42: Calibrated Testing of Device 6.4.1

B.6 Additional Vapor Testing

Vapor tests were repeated on the 3 micron line width device that showed initial ethanol sensing ability. The results of these tests are shown in Figures B.43 and B.44. The devices responded similarly to the original tests when exposed to ethanol vapors, showing sensing repeatability.

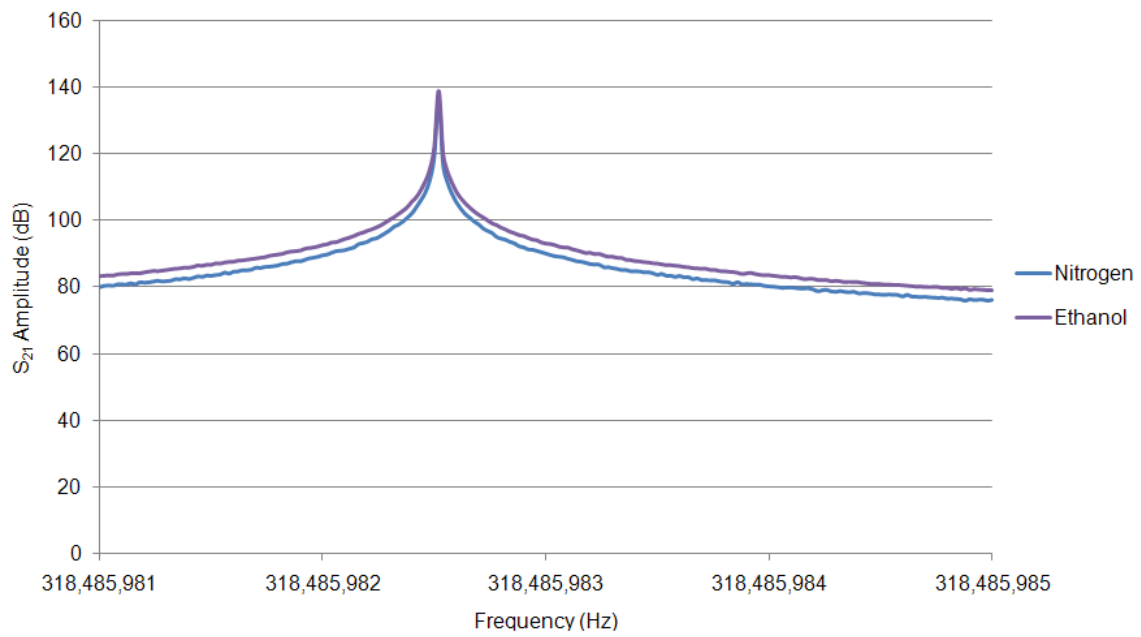
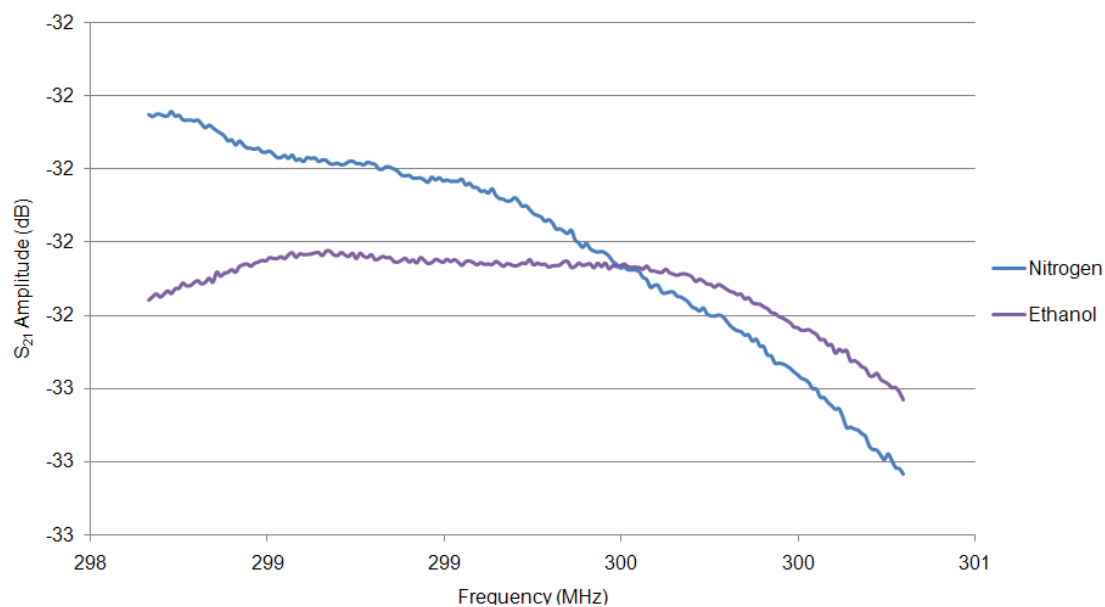
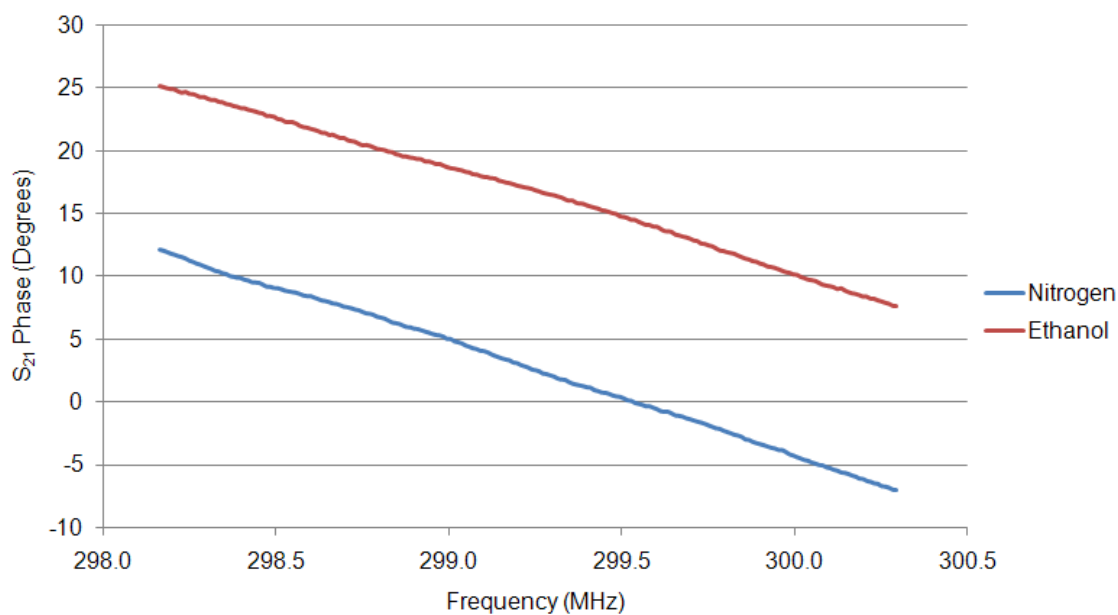


Figure B.43: S_{21} amplitude changes replicated the results of the previous vapor sensing experiment on the 3 micron device when scanned near the peak at 318 MHz.



(a)



(b)

Figure B.44: S_{21} measurements replicated the results of the original vapor sensing experiment on the 3 micron device when scanned near the side lobe peak at 298 MHz. (a) S_{21} amplitude showing a shifted peak upon ethanol exposure (b) The S_{21} phase also shifts near the resonance peak nearly 2 MHz.

Appendix C. Lessons Learned

C.1 Equipment

There are several symptoms that may be expressed when the EVG620 is low on nitrogen. First, the light may not ignite during startup, so one should always take a glance to check for this. More subtly, the bulb may turn off when it overheats during use. This may only be noticed when a development comes out with no visible pattern. If this happens, the nitrogen should be one of the first things to check. Finally, the vacuum may not be able to hold the mask properly. This is a dangerous condition, since the machine seems to be unable to reverse the process upon vacuum failure, gives an error, and continues with the process, possibly causing damage to the mask or mask aligner. Because of the dangers here one should always check the nitrogen levels before loading a mask, making sure that the gauge reads above 5.

Double check to make sure the mask is loaded properly with the chrome side facing down. If the mask is mirrored, then any writing designed into the mask should be readable from above.

The ultrasonic bath contains a heating element that defaults to the “on” position. To avoid heating the bath excessively, thus causing process variations, the temperature should be set to 0 °C. This does not induce cooling, but does prevent the bath from heating up unnecessarily.

The chip holder on the MMR probe station should always be screwed into the main body of the vacuum chamber before probing the devices. This reduces the vibrations between the probes and samples, leading to better quality contacts and a lower chance of device damage.

C.2 Processing

Always use a smaller chuck on the spinner than the size of the chips. While this may increase the chances of dropping the chip in the wafer, techniques are quickly learned in order to reduce this, such as extra care during placement and turning

on the vacuum before placing the chip. By using a smaller chuck, one ensures that photoresist does not get on the back of the chip, which can cause significant problems during lithography by pushing the chip out of plane with respect to the mask.

Be as consistent as possible during fabrication. Even small things like using a different hot plate can cause process variations. These variations can lead to inconsistent fabrication results. Doing this will also require keeping track of details.

Always put photoresist on a wafer before dicing it with a diamond saw. 1818 spun at 500 rpm and baked on the hotplate for 2 minutes at 110 °C works well. This prevents debris from the dicing process from adhering to the surface of the wafer, which will cause significant difficulties during subsequent fabrication steps. Keep the photoresist on the individual chips until ready to use them, since additional debris is created when edges are chipped off in removing the samples from the sticky backing.

Clean the mask both before and after contact lithography. If one only cleans the mask before exposing devices, the photoresist residue that sticks on the mask has a chance to harden, which makes it much more difficult to remove in the future. If one does find hardened photoresist on a mask, the best results seem to come from hard scrubbing with an acetone-soaked cotton swab.

When sonicating to release a metal lift-off layer, there are several steps that can be taken to increase the chances of positive results. First, allow the wafers to soak in acetone before sonication. This allows less time in the ultrasonic bath, which tends to damage chips if left for a long period of time. Second, ensure that enough water is in the ultrasonic bath to allow the petri dish to float. Too little water seems to contribute to the breaking up of the wafer. Third, each piece sonicated should have its own petri dish to avoid damage from other samples. Finally, make sure that the acetone in the petri dishes stays full. Since the acetone evaporates very quickly, it is easy to let a sample dry during sonication. Not only does this allow released metal to stick to the device surface, but wafers that are sonicated while dry seem to experience increased amounts of damage.

C.3 Design

Design the mask with redundancy in mind. Often in order to optimize an unknown design, a number of variations of a device may be incorporated into a mask in order to test different variables. Since areas of a mask may be damaged during processing, it is important to have redundant devices on different sections of the mask. This reduces down both cost and down time in the case of mask damage.

Use larger wafers if possible. This reduces thickness variations in the photoresist during photolithography due to edge effect. Performing photolithography on chips as small as 1 cm² is possible, but device uniformity becomes much more difficult. Areas where the photoresist is too thick may be subject to underdevelopment at the same time that thinner sections show overdevelopment.

The base of the fingers between the acoustic aperture and main electrical bus was a common area for bridging to occur. This could be due to diffraction effects partially exposing the photoresist protecting this area of the substrate. Increasing the length of the base of the fingers to 3λ may reduce this phenomenon by spatially separating the diffraction sources.

C.4 Planning

Always write down everything in detail, even things that could be considered obvious. When writing a thesis, these details will be critical. As an even better alternative, write the thesis as the work progresses. Not only does this maximize the accuracy of the document, but it allows significant more time during the final quarter to finish experimentation and breaks the writing into more manageable chunks.

Develop a thesis completion timeline with buffer room built in. This forces one to think through the steps of what needs to be done, reducing the likelihood of overlooking something or running out of time. Additionally, this allows one to allocate the proper amount of time to the project and prepare necessary resources before they are needed.

Lithography is not an exact science. Developing a process takes a lot of trial and error and time. Plan this into the timeline and start fabrication as early as possible.

Bibliography

1. L. J. Rose, *Air Force Research Laboratory's Focused Long Term Challenges*. Air Force Research Laboratory, Munitions Directorate.
2. "Joint Requirements Area BAA for Topics Related to Detection of Person-Borne and Vehicle-Borne Improvised Explosive Devices," Tech. Rep. BAA09-04, U.S. Department of Homeland Security, October 2008.
3. S. Singh, "Sensors: An Effective Approach for the Detection of Explosives," *Journal of Hazardous Materials*, vol. 144, pp. 15–28, June 2007.
4. M. H. Ervin, S. J. Kilpatrick, C. Lombardo, B. M. Nichols, A. C. Perrella, and A. E. Wickenden, "The Present State of Amperometric Nanowire Sensors for Chemical and Biological Detection," Tech. Rep. ARL-TR-3962, Army Research Laboratory, October 2006.
5. K. J. Krieg, *Department of Defense Chemical and Biological Defense Program Annual Report to Congress*, 2007.
6. N. Kingsbury, *Land Mine Detection: DOD's Research Program Needs a Comprehensive Evaluation Strategy*. United States General Accounting Office, 2001.
7. G. K. Kannan, A. T. Nimal, U. Mittal, R. D. S. Yadava, and J. C. Kapoor, "Adsorption Studies of Carbowax Coated Surface Acoustic Wave (SAW) Sensor for 2,4-Dinitro Toluene (DNT) Vapour Detection," *Sensors and Actuators B: Chemical*, vol. 101, no. 3, pp. 328–334, 2004.
8. Board on Army Science and Technology, National Research Council, *Opportunities in Biotechnology for Future Army Applications*. Washington DC: National Academy Press, 2001.
9. M. Allard, 2008.
10. M. Penza, M. A. Tagliente, P. Aversa, and G. Cassano, "Organic-Vapor Detection Using Carbon-Nanotubes Nanocomposite Microacoustic Sensors," *Chemical Physics Letters*, vol. 409, pp. 349–354, June 2005.
11. O. K. Varghese, D. Gong, W. R. Dreschel, K. G. Ong, and C. A. Grimes, "Ammonia detection using nanoporous alumina resistive and surface acoustic wave sensors," *Sensors and Actuators B: Chemical*, vol. 94, pp. 27–35, August 2003.
12. J. W. Grate, "Chemical Information from Polymer-Coated Acoustic Wave Sensor Arrays," *Proceedings of SPIE, the international society for optical engineering*, vol. 3857, pp. 170–173, 1999.
13. M. C. Horrillo, M. J. Fernandez, J. L. Fontecha, I. Sayago, M. Garcia, M. Alexandre, J. P. Santos, L. Araos, J. Gutierrez, I. Gracia, and C. Canao, "Detection of Volatile Organic Compounds Using Surface Acoustic Wave Sensors with Different Polymer Coatings," *Thin Solid Films*, vol. 467, pp. 234–238, November 2004.

14. A. E. Hoyt, A. J. Ricco, J. W. Bartholomew, and G. C. Osbourn, "Simultaneous Measurement of CO₂ and Humidity Using a Pair of SAW Devices and Cluster-Analysis Pattern Recognition," *Solid State Sensors and Actuators, 1997. TRANSDUCERS '97 Chicago., 1997 International Conference on*, vol. 2, p. 1339, 1997.
15. M. G. Milner, "Detection/Classification/Quantification of Chemical Agents Using an Array of Surface Acoustic Wave (SAW) Devices," *Proceedings of SPIE, the international society for optical engineering*, vol. 5778, p. 305.
16. E. T. Zellers, "Effects of Temperature and Humidity on the Performance of Polymer-Coated Surface Acoustic Wave Vapor Sensor Arrays," *Analytical Chemistry (Washington)*, vol. 68, no. 14, pp. 2409–2418, 1996.
17. J. R. Vig, "Quartz Crystal Resonators and Oscillators For Frequency Control and Timing Applications - A Tutorial," January 2007.
18. D. S. Ballantine, R. M. White, S. J. Martin, A. J. Ricco, E. T. Zellers, G. C. Frye, and H. Wohltjen, *Acoustic Wave Sensors*. San Diego, CA: Academic Press, 1997.
19. G. Kovacs, *Micromachined Transducers Sourcebook*. Boston, MA: McGraw-Hill, 1998.
20. M. Thompson and D. C. Stone, *Surface-Launched Acoustic Wave Sensors*. New York: John Wiley and Sons, 1997.
21. C. K. Campbell, *Surface Acoustic Wave Devices for Mobile and Wireless Communications*. San Diego: Academic Press, 1998.
22. J. D. N. Cheeke, N. Tashtoush, and N. Eddy, "Surface Acoustic Wave Humidity Sensor Based on the Changes in the Viscoelastic Properties of a Polymer Film," *IEEE Ultrasonics Symposium Proceedings*, vol. 1, p. 449, 1996.
23. D. D. Stubbs, W. D. Hunt, S. H. Lee, and D. F. Doyle, "Gas Phase Activity of Anti-FITC Antibodies Immobilized on a Surface Acoustic Wave Resonator Device," *Biosensors and Bioelectronics*, vol. 17, 2002.
24. D. D. Stubbs, S. H. Lee, and W. D. Hunt, "Vapor Phase Detection of a Narcotic Using Surface Acoustic Wave Immunoassay Sensors," *IEEE Sensors Journal*, vol. 5, no. 3, p. 335, 2005.
25. W. D. Hunt, D. D. Stubbs, and S.-H. Lee, "Time-Dependent Signatures of Acoustic Wave Biosensors," *Proceedings of the IEEE*, vol. 91, no. 6, pp. 890–901, 2003.
26. I. D. Avramov, S. Kurosawa, M. Rapp, P. Krawczak, and E. I. Radeva, "Investigations on Plasma-Polymer-Coated SAW and STW Resonators for Chemical Gas-Sensing...", *IEEE Transactions on Microwave Theory and Techniques*, vol. 49, p. 827, April 2001.
27. R. D. S. Yadava, "Enhancing Mass Sensitivity of SAW Delay Line Sensors by Chirping Transducers," *Sensors and Actuators B: Chemical*, vol. 114, pp. 127–131, March 2006.

28. W. Wen, H. Shitang, L. Shunzhou, L. Minghua, and P. Yong, "Enhanced Sensitivity of SAW Gas Sensor Coated Molecularly Imprinted Polymer Incorporating High Frequency Stability Oscillator," *Sensors and Actuators B: Chemical*, vol. 125, pp. 422–427, August 2007.
29. A. J. Slobodnik, E. D. Conway, and R. T. Delmonico, *Microwave Acoustic Handbook, Surface Wave Velocities*. NTIS, US Dept of Commerce, 1973.
30. Y. Rao and G. Zhang, "3D Modeling of a Surface-Acoustic-Wave Based Sensor," 2007.
31. Y. Zheng, "Biosensors on Surface Acoustic Wave Phononic Band Gap Structures," *NNIN REU Research Accomplishments*, p. 156, 2004.
32. Y. Ying and Z. Da-Zhong, "A Y-type SAW Mass Sensor with Metal Array Reflectors," *Sensors and Actuators B: Chemical*, vol. 109, pp. 244–248, September 2005.
33. G. S. May and S. M. Sze, *Fundamentals of Semiconductor Fabrication*. Hoboken, NJ: Wiley, 1998.
34. B. Hardwidge, "IBM and AMD Create First 22 nm SRAM Cell," *Custom PC*, 2008.
35. R. C. Jaeger, *Introduction to Microelectronic Fabrication*. Upper Saddle River, NJ: Prentice Hall, 2002.
36. J. H. Anderson and L. J. Rodrigues, "Terrorism and Drug Trafficking: Technologies for Detecting Explosives and Narcotics," Tech. Rep. GAO/NSIAD/RCED-96-252, United States Government Accountability Office, 1996.
37. U. Vaishnav, P. Apte, S. Lokhre, V. Palkar, and S. Pattalwar, "Micromechanical Components with Novel Properties," in *SPIE Symposium on Smart Materials, Structures and MEMS*, vol. 3321, pp. 287–297, SPIE, 1996.
38. Zeiss, *Focused Ion Beam Essential Specifications: NVision 40*, 2009.
39. Microchem, *LOR and PMGI Resists*, 2009.
40. M. Jackson and G. Robinson, "Emerging Micro and Nanomanufacturing Processes for Electrical and Electronic Engineering Applications," in *Electrical Insulation Conference and Electrical Manufacturing Expo Proceedings*, IEEE, 2005.
41. B. H. Jo, L. M. Van Lerberghe, K. M. Motsegood, and D. J. Beebe, "Three-Dimensional Micro-Channel Fabrication in Polydimethylsiloxane (PDMS) Elastomer," *IEEE/ASME Journal of Microelectromechanical Systems*, vol. 9, pp. 76–81, March 2000.
42. F. Hoppe-Seyler and K. Butz, "Peptide Aptamers: Powerful New Tools for Molecular Medicine," *Journal of Molecular Medicine*, vol. Volume 78, no. 8, pp. 426–430, 2000.

43. M. Mir, I. Katakis, and M. Vreeke, "Aptamer Biosensors: An Alternative to Immunosensors," *In Vitro Detection Technology*, 2007.
44. J. M. Slocik, E. R. Beckel, H. Jiang, J. O. Enlow, J. S. J. Zabinski, T. J. Bunning, and R. R. Naik, "Site-Specific Patterning of Biomolecules and Quantum Dots on Plasma-Enhanced Chemical Vapor Deposited Surfaces," *Advanced Materials*, 2006.
45. S. C. Huang, K. D. Caldwell, J. N. Lin, H. K. Wang, and J. N. Herron, "Site-Specific Immobilization of Monoclonal Antibodies Using Spacer-Mediated Antibody Attachment," *Langmuir*, vol. 12, no. 17, pp. 4292–4298, 1996.
46. R. A. Potyrailo and W. G. Morris, "Wireless Resonant Sensor Array for High-Throughput Screening of Materials," *Review of Scientific Instruments*, vol. 78, no. 7, 2007.
47. R. A. Potyrailo and W. G. Morris, "Multianalyte Chemical Identification and Quantitation Using a Single Radio Frequency Identification Sensor," *Analytical Chemistry*, vol. 79, no. 1, pp. 45–51, 2007.
48. "Nafion," *Wikipedia*, 2009.
49. A. Huang, V. T. S. Wong, and C.-M. Ho, "Silicone Polymer Chemical Vapor Sensors Fabricated by Direct Polymer Patterning on Substrate Technique (DP-POST)," *Sensors and Actuators B*, vol. 116, pp. 2 – 10, 2006.
50. D. T. Rooney, D. Nager, D. Geiger, and D. Shangguan, "Evaluation of Wire Bonding Performance, Process Conditions, and Metallurgical Integrity of Chip on Board Wire Bonds," *Microelectronics and Reliability*, vol. 45, no. 2, pp. 379 – 390, 2005.
51. Alternate Finishing, Inc, *Services*, 2008.
52. G. Clatterbaugh, J. Weiner, and J. Charles, H., "Gold-Aluminum Intermetallics: Ball Bond Shear Testing and Thin Film Reaction Couples," *IEEE Transactions on Components, Hybrids, and Manufacturing Technology*, vol. 7, pp. 349–356, Dec 1984.

Index

The index is conceptual and does not designate every occurrence of a keyword. Page numbers in bold represent concept definition or introduction.

- Acoustic Aperture, 9, 16
- Acoustic Reflections, 14
- Acoustic Velocity, 19
- Acoustoelectric Effect, 11
- Apodization, 21
- Bulk Micromachining, 27
- CBRNE, 1
- Chemical Vapor Deposition (CVD), 31, 35
- Chirped IDT, 24
- Deep Reactive Ion Etching (DRIE), 29
- E-Beam Lithography, 27
- Electromechanical Coupling Factor, 19
- Evaporation, 30
- Finger Thickness, 14
- Focused Ion Beam (FIB), 29
- Focused Long Term Challenge (FLTC), 1
- Global Situational Awareness (GSA), 1
- Improvised Explosive Device (IED), 1
- Insertion Loss, 13, 21
- Integrated Oscillator Analysis, 37
- Interdigital Transducer(IDT), 7
- Laser Ablation, 29
- Laser-Assisted Chemical Etching (LACE),
29
- Lift-Off Resist (LOR), 32
- Mass-loading Effect, 11
- MEMS, 5
- Metal Liftoff, 32
- Non-Planar Surfaces, 20
- Odorant Binding Protein (OBP), 3, 36
- Photolithography, 25
- Piezoelectric Effect, 5
- Plasma Enhanced CVD (PECVD), 36
- Plasma Etching, 29
- PMMA, 21
- Reactive Ion Etching (RIE), 29
- Sacrificial Layer, 31
- Scanning Electron Microscope(SEM), 57
- SOLT, 41
- Sputtering, 31
- Step Coverage, 30
- Surface Acoustic Wave (SAW), 3, 5
- Surface Micromachining, 30
- Temperature Coefficient of Delay, 20
- Transmission Parameter Analysis, 37
- Unmanned Aerial Vehicle (UAV), 1
- Vector Network Analyzer, 46
- Viscoelastic Effect, 12

REPORT DOCUMENTATION PAGE					Form Approved OMB No. 0704-0188	
<p>The public reporting burden for this collection of information is estimated to average 1 hour per response, including the time for reviewing instructions, searching existing data sources, gathering and maintaining the data needed, and completing and reviewing the collection of information. Send comments regarding this burden estimate or any other aspect of this collection of information, including suggestions for reducing the burden, to Department of Defense, Washington Headquarters Services, Directorate for Information Operations and Reports (0704-0188), 1215 Jefferson Davis Highway, Suite 1204, Arlington, VA 22202-4302. Respondents should be aware that notwithstanding any other provision of law, no person shall be subject to any penalty for failing to comply with a collection of information if it does not display a currently valid OMB control number.</p> <p>PLEASE DO NOT RETURN YOUR FORM TO THE ABOVE ADDRESS.</p>						
1. REPORT DATE (DD-MM-YYYY) 26-03-2009		2. REPORT TYPE Master's Thesis		3. DATES COVERED (From - To) September 2007 - March 2009		
4. TITLE AND SUBTITLE Surface Acoustic Wave Devices As Chemical Vapor Sensors				5a. CONTRACT NUMBER		
				5b. GRANT NUMBER		
				5c. PROGRAM ELEMENT NUMBER		
				5d. PROJECT NUMBER ENG-09-221		
6. AUTHOR(S) Gallagher, Daniel M, GS-11, DAF				5e. TASK NUMBER		
				5f. WORK UNIT NUMBER		
7. PERFORMING ORGANIZATION NAME(S) AND ADDRESS(ES) Air Force Institute of Technology Graduate School of Engineering and Management (AFIT/EN) 2950 Hobson Way WPAFB OH 45433				8. PERFORMING ORGANIZATION REPORT NUMBER AFIT/GE/ENG/09-16		
9. SPONSORING/MONITORING AGENCY NAME(S) AND ADDRESS(ES) Air Force Research Laboratory Attn: Dr. Rajesh Naik Rajesh.naik@wpafb.af.mil 937-785-9717 3005 Hobson Way, Building 654 WPAFB, OH 45433				10. SPONSOR/MONITOR'S ACRONYM(S) AFRL/RXBN		
				11. SPONSOR/MONITOR'S REPORT NUMBER(S)		
12. DISTRIBUTION/AVAILABILITY STATEMENT Approved for Public Release; Distribution Unlimited						
13. SUPPLEMENTARY NOTES						
14. ABSTRACT The objective of this research is to develop a transducer for recognition of molecular changes in the presence of chemical vapors. This transducer is tested using polymer sensing layers known to be sensitive to ethanol vapors. A surface acoustic wave device is selected as the transducer element due to low cost, high surface sensitivity, and sensitivity. These devices are designed and fabricated in-house, and a polymer sensing layer applied. The frequency response of the coated device is probed both with and without the presence of airborne ethanol molecules in a vapor stream. By analyzing the changes in the amplitude and phase of the frequency response near resonance, vapor detection was conclusively demonstrated. Additionally, the mechanism of change was identified, allowing future work in optimizing the sensitivity of the device. Other future work will include application of a biomolecular sensing layer, design of circuitry for a portable devices, and fabrication of a MEMS preconcentrator. The final goal of the project is a portable sensor array using surface acoustic wave devices coated with different bio-molecules.						
15. SUBJECT TERMS Vapor sensor, Biosensor, MEMS, IED, Biomimetic, Electronic Nose, TNT, Surface Acoustic Wave, Piezoelectric, SAM						
16. SECURITY CLASSIFICATION OF:			17. LIMITATION OF ABSTRACT	18. NUMBER OF PAGES	19a. NAME OF RESPONSIBLE PERSON	
a. REPORT	b. ABSTRACT	c. THIS PAGE			Ronald Coutu, LTC, USAF	
U	U	U	UU	161	19b. TELEPHONE NUMBER (Include area code) 937-255-3636 (x7230) Ronald.Coutu@afit.edu	

Reset